SYSTEMATIC VERTICAL GROUND MOTION OBSERVATIONS IN THE CANTERBURY EARTHQUAKES

Zach Bullock

Brendon A. Bradley

Research report 2016-03

Department of Civil Engineering

University of Canterbury

Christchurch

New Zealand

18 March 2016

Table of Contents

1 Introduction

The 2010-2011 Canterbury earthquake sequence was extremely damaging to structures in Christchurch and continues to have a large economic and social impact on the city and surrounding regions. In addition to strong ground shaking (Bradley and Cubrinovski 2011 SRL; Bradley 2012 SDEE), extensive liquefaction was observed, particularly in the 4 September 2010 Darfield earthquake and the 22 February 2011 Christchurch earthquake (Cubrinovski et al. 2010 BNZSEE; 2011 SRL). Large observed vertical ground motion amplitudes were recorded in the events in this sequence, with vertical peak ground accelerations of over 2.2g being observed at the Heathcote Valley Primary School during the Christchurch earthquake, and numerous other vertical motions exceeding 1.0g (Bradley and Cubrinovski 2011 SRL; Bradley 2012 SDEE; Fry et al 2011 SRL). Vertical peak ground accelerations of over 1.2g were observed in the Darfield earthquake.

Prior research has indicated that large vertical ground motions are principal contributors to structural response (e.g. Papazoglou and Elnashai 1996; Ghobarah and Elnashai 1998), or in contrast that they are not important. While the absolute significance of vertical ground motions remains a topic of debate, it is generally accepted that such motions (in addition to the imposed horizontal ground motion components) are certainly not beneficial, and their significance increases for structures with non-ductile structures/bridges with flexible flooring/decks, or equivalent components (Ghobarah and Tso 1973; Saadeghvariri and Foutch 1991; Kunnath et al 2008). The effects of vertical motion on structural behavior are also worsened during motions in which the peak vertical motion coincides with the peak horizontal motion (Kim et al 2010). The vertical and horizontal components of ground motion are more likely to be "in phase" in this manner at rock sites than at soil sites (Silva 1997).

This study provides a detailed examination of the amplitude characteristics of vertical ground motion records from the Canterbury sequence relative to empirical ground motion prediction equations (GMPEs). As such, this study expands upon the initial analysis of Lee et al. (2013), via an evaluation of the applicability of vertical response spectral acceleration (SA) GMPEs from the recently-completed Next Generation Attenuation West 2 project, and an examination of the systematic regional and site-specific effects of the observed vertical ground motions.

1.1 Events and Stations Considered

10 earthquake events of engineering significance, utilized in Bradley (2013) and shown in Figure 1, were adopted for this study to examine vertical ground motion characteristics. Some features of these 10 events are illustrated in Table 1, in particular the maximum source-to-site distance, R_{rup}, in order to focus on ground motion amplitudes of engineering interest (discussed subsequently in further detail). 25 strong motion stations were considered, as shown in Figure 5, which is expanded from the initial set of Bradley (2013) to include five stations in the Port Hills region: GODS, PARS, STKS, D14C, and MTPS, in order to examine the suspected influence of topographical effects on the vertical motions in this region. The vertical peak ground accelerations observed at each considered strong motion station during each event

are shown in Table 2. A histogram of the values in Table 2 is given in Figure 2. The peak vertical ground acceleration for the records considered ranges from 0.005*g* to 2.206*g* with a mean of 0.199*g*.

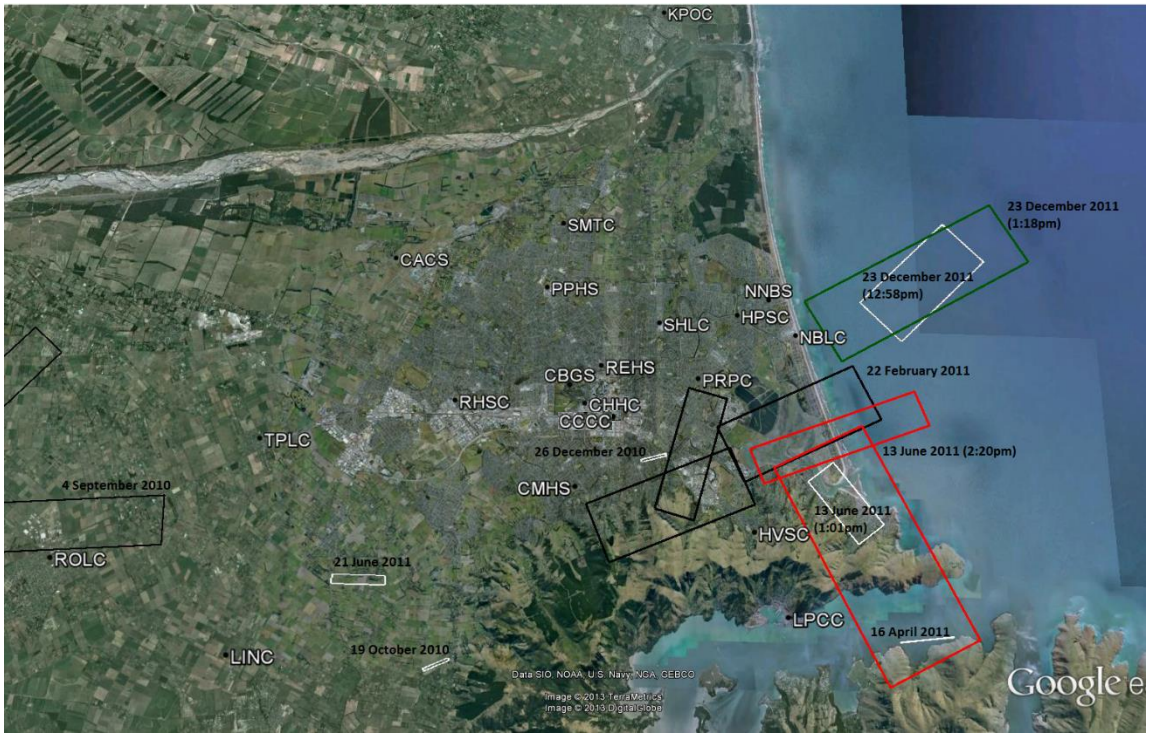

Figure 1: Location of the finite fault planes of the 10 considered earthquake events, and the location of the 25 strong motion stations at which systematic site effects are examined. Color coding of the finite fault models is for clarity only.

Table 1: Characteristics of the considered events

ID	Event date	Magnitude	Maximum Rrup (km)
1	4 September 2010	7.1	67
2	19 October 2010	4.8	20
3	26 December 2010	4.7	20
4	22 February 2011	6.2	34
5	16 April 2011	5	20
6	13 June 2011 (1:01pm)	5.3	34
7	13 June 2011 (2:20pm)	6	34
8	21 June 2011	5.2	20
9	23 December 2011 (12:58pm)	5.8	34
10	23 December 2011 (2:18pm)	5.9	34

Table 2: Characteristics of the strong motion stations considered and the vertical PGA recorded during each considered event

Station	Site Class	Num events	1	2	3	4	5	6	7	8	9	10
CACS	D	10	0.296	0.024	0.018	0.189	0.030	0.051	0.072	0.092	0.063	0.060
CBGS	D	10	0.124	0.042	0.443	0.350	0.041	0.069	0.096	0.056	0.083	0.101
CCCC	D	6	0.194	0.075	0.179	0.788	-	-	-	-	0.154	0.104
CHHC	D	10	0.153	0.053	0.160	0.622	0.130	0.107	0.209	0.063	0.110	0.120
CMHS	D	9	0.294	0.177	0.097	0.854	0.098	0.138	0.172	-	0.104	0.128
HPSC	E	10	0.141	0.021	0.047	1.026	0.155	0.535	0.349	0.041	0.357	0.392
HVSC	C	10	0.308	0.066	0.068	2.206	0.454	0.224	0.694	0.174	0.247	0.232
KPOC	D	8	0.088	0.007	0.005	0.062	0.013	0.041	0.043	0.014	-	-
LINC	D	10	0.898	0.034	0.011	0.094	0.048	0.021	0.069	0.312	0.039	0.088
LPCC	D	9	0.152	0.030	0.012	0.515	0.126	0.111	0.315	0.038	-	0.175
NBLC	D	7	-	0.018	0.013	-	0.135	0.342	0.375	0.034	0.964	-
NNBS	E	8	0.141	0.011	0.018	0.799	0.124	0.317	0.291	0.025	-	-
PPHS	D	10	0.278	0.038	0.091	0.208	0.025	0.063	0.092	0.056	0.061	0.067
PRPC	E	9	0.318	0.066	0.088	1.880	0.347	0.700	0.793	0.070	0.435	-
REHS	D	10	0.221	0.035	0.263	0.514	0.067	0.234	0.182	0.060	0.122	0.186
RHSC	D	9	0.311	0.210	-	0.192	0.070	0.063	0.159	0.235	0.066	0.116
ROLC	D	10	0.702	0.009	0.009	0.076	0.010	0.021	0.027	0.084	0.055	0.036
SHLC	D	10	0.137	0.022	0.058	0.489	0.074	0.144	0.167	0.038	0.127	0.242
SMTC	D	10	0.229	0.028	0.021	0.167	0.022	0.173	0.067	0.048	0.060	0.082
TPLC	D	10	0.935	0.096	0.031	0.157	0.037	0.043	0.072	0.604	0.087	0.080
GODS	B	5	-	-	-	-	0.195	0.100	1.193	-	0.139	0.117
PARS	B	6	-	-	-	-	0.407	0.104	0.699	0.027	0.193	0.176
STKS	B	6	-	-	-	-	0.047	0.077	0.098	0.081	0.072	0.076
D14C	B	6	-	-	-	-	0.085	0.041	0.137	0.147	0.079	0.065
MTPS	B	6	-	-	-	-	0.329	0.122	0.634	0.067	0.169	0.142

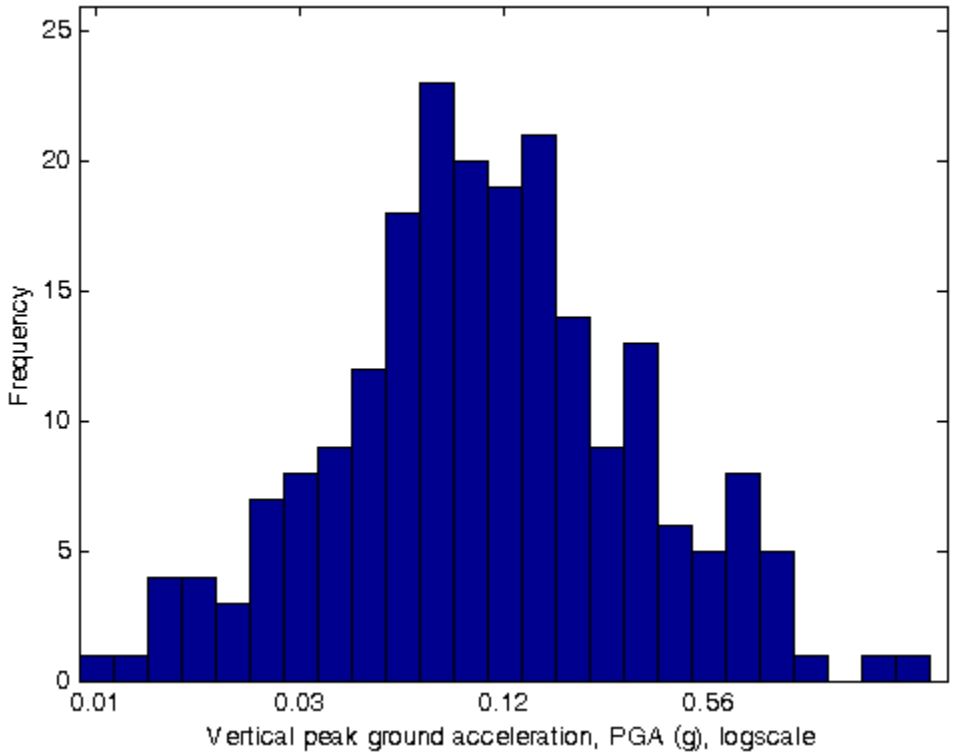

Figure 2: Histogram of the vertical PGA values at each considered station in each considered event

2 Comparison of Considered GMPEs with Observed Vertical Ground Motion Amplitudes

2.1 Considered models and causal parameter ranges

All four of the vertical ground motion prediction equations that were developed as part of the Next Generation Attenuation for the Western United States (NGA-West2) project were considered: Gülerce, Kamai, Abrahamson and Silva (2013) (henceforth referred to as GKAS13); Stewart, Seyhan, Boore and Atkinson (2013) (henceforth referred to as SSBA13); Bozorgnia and Campbell (2013) (henceforth referred to as BC13); and Campbell and Young (2013) (henceforth referred to as CY13). All four of these GMPEs were developed using recordings from worldwide earthquakes, while some model coefficients are specific for different geographic regions. Only SSBA13 includes explicit specific consideration for New Zealand in these adjustments.

A summary of the constraints on the NGA-West2 GMPEs is presented in Table 3. All considered events and stations fall within the applicability of GKAS2013. SSBA13 is poorly suited to the 19 October 2010 and 26 December 2010 events, for which Mw<5.0, and to Site Class E sites, which are assumed to have a V_{S30} of 180m/s, but is applicable to all other events and site classes. BC13 is appropriate for all events and sites considered. CY13 is also applicable for all events and sites considered in this study.

Table 3: Applicability of the NGA-West2 vertical GMPEs

GMPE	Magnitude	Distance	Shear Wave Velocity	Period	Depth
GKAS13	$3.0 \leq M \leq 8.5$	$R_{rup} \leq 300km$	$180m/s \leq V_{S30}$	$T \leq 10s$	-
SSBA13	$5.0 \leq M \leq 8.5$	$R_{JB} \leq 400km$	$200m/s \leq V_{S30} \leq 1500m/s$	$T \leq 3s$	-
BC13	$3.3 \leq M \leq 8.5$	$R_{rup} \leq 300km$	$150m/s \leq V_{S30} \leq 1500m/s$	$T \leq 3s$	$Z_{HYP} \leq 20km$
CY13	$3.5 \leq M \leq 8.5$	$R_{rup} \leq 300km$	$180m/s \leq V_{S30} \leq 1500m/s$	$0s < T \leq 3s$	$Z_{TOR} \leq 20km$

Due to the range of vibration periods for which most of the NGA-West2 GMPEs are valid, and because T=3 seconds is considered a very long natural period of vertical excitation for most structures, the range of periods for consideration in this study was selected to be T=0-3s.

2.2 Comparison of the general trends in the considered GMPEs

Figure 3 shows acceleration spectra for each individual NGA-West2 GMPE for magnitudes of 6.0 and 7.0. It can be seen that all four of the NGA-West2 vertical GMPEs produce similar results for given values of magnitude. Plots of vertical PGA versus distance-to-rupture for each NGA-West2 vertical GMPE for an event with Mw=7.0 are included in Figure 4. Because Chiou and Youngs (2013) is invalid for a vibration period of precisely 0 seconds, a period of 0.01 seconds was used to produce this plot. Figure 3 and Figure 4 illustrate the similarity among the NGA-West2 vertical GMPEs.

Because there is no marked difference between the four GMPEs, and because their applicability is roughly equivalent and inclusive of the characteristics of the considered stations and events, a simple mean of all four NGA-West2 GMPEs was used for the median ground motion prediction for all subsequent analysis.

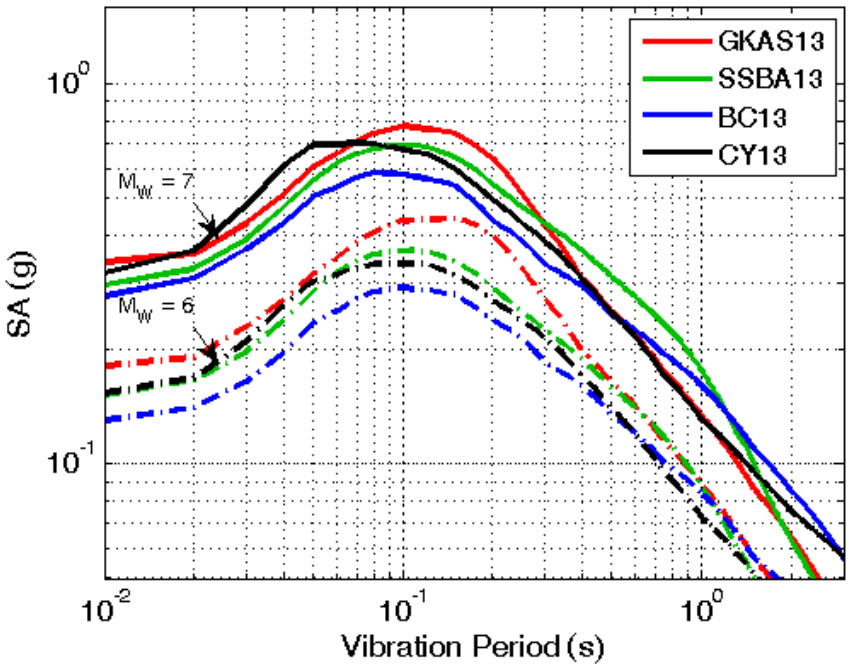

Figure 3: Vertical acceleration spectra produced by the NGA-West2 vertical GMPEs for selected magnitudes with other inputs fixed

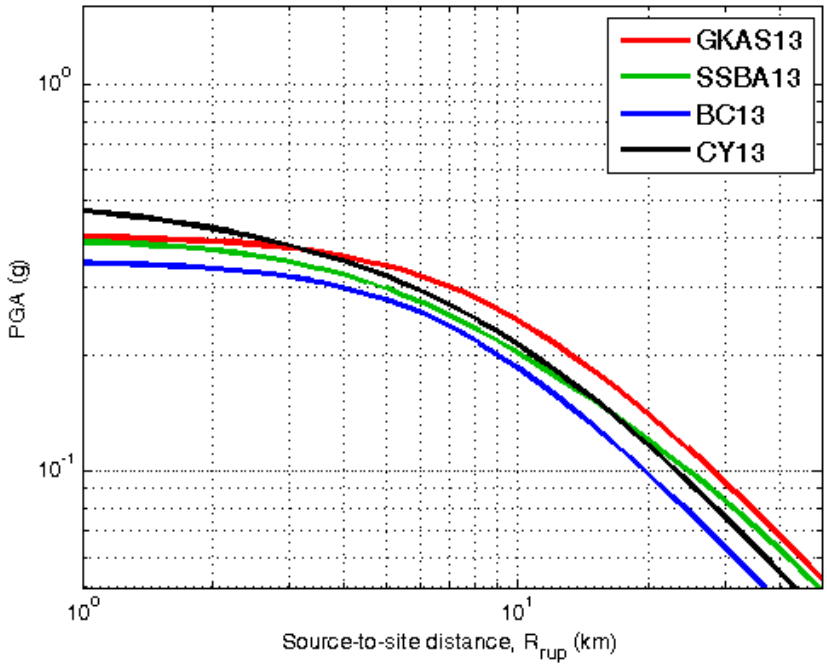

Figure 4: PGA values produced by the NGA-West2 GMPEs versus distance to rupture with all other inputs fixed

3 Prediction Bias of the NGA-West2 Vertical Ground Motion Prediction Equations

3.1 Evaluation of Bias in the Unadjusted NGA-West2 Vertical Ground Motion Prediction Equations

In order to examine the systematic site and location effects on vertical motion in the Canterbury earthquake sequence, the performance of the NGA-West2 GMPEs was first evaluated. Figure 5 shows the predicted median ground motion with bounds of plus or minus one logarithmic standard deviation produced using the suite of NGA-West2 vertical GMPEs plotted with the observed values from the Canterbury earthquake sequence. All of these plots were produced for a vibration period of 0.05 seconds, which is typically where the acceleration spectrum of vertical records reaches its peak. Similar plots for periods of 0.01 seconds, 0.1 seconds, and 0.2 seconds are included in Appendix A.

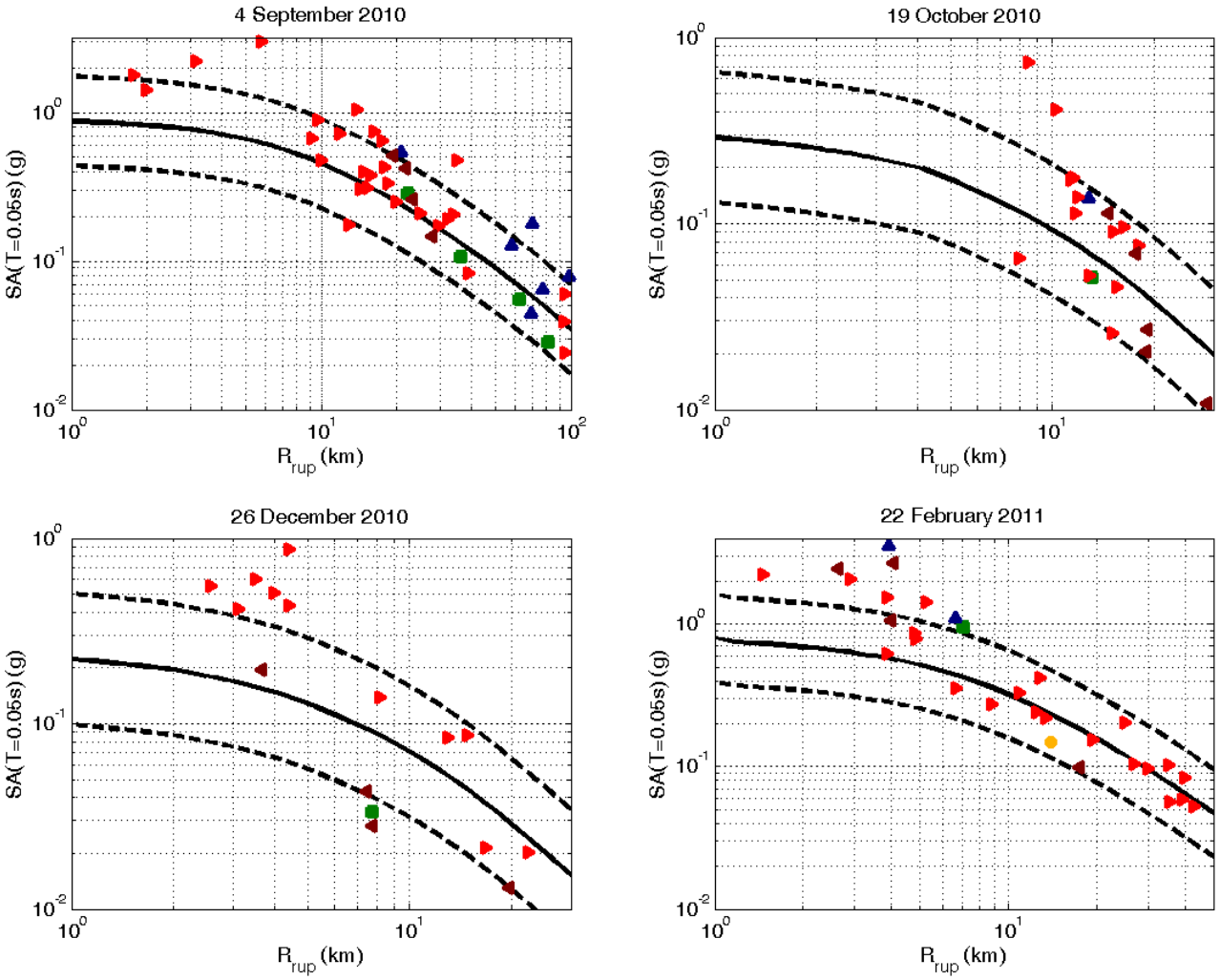

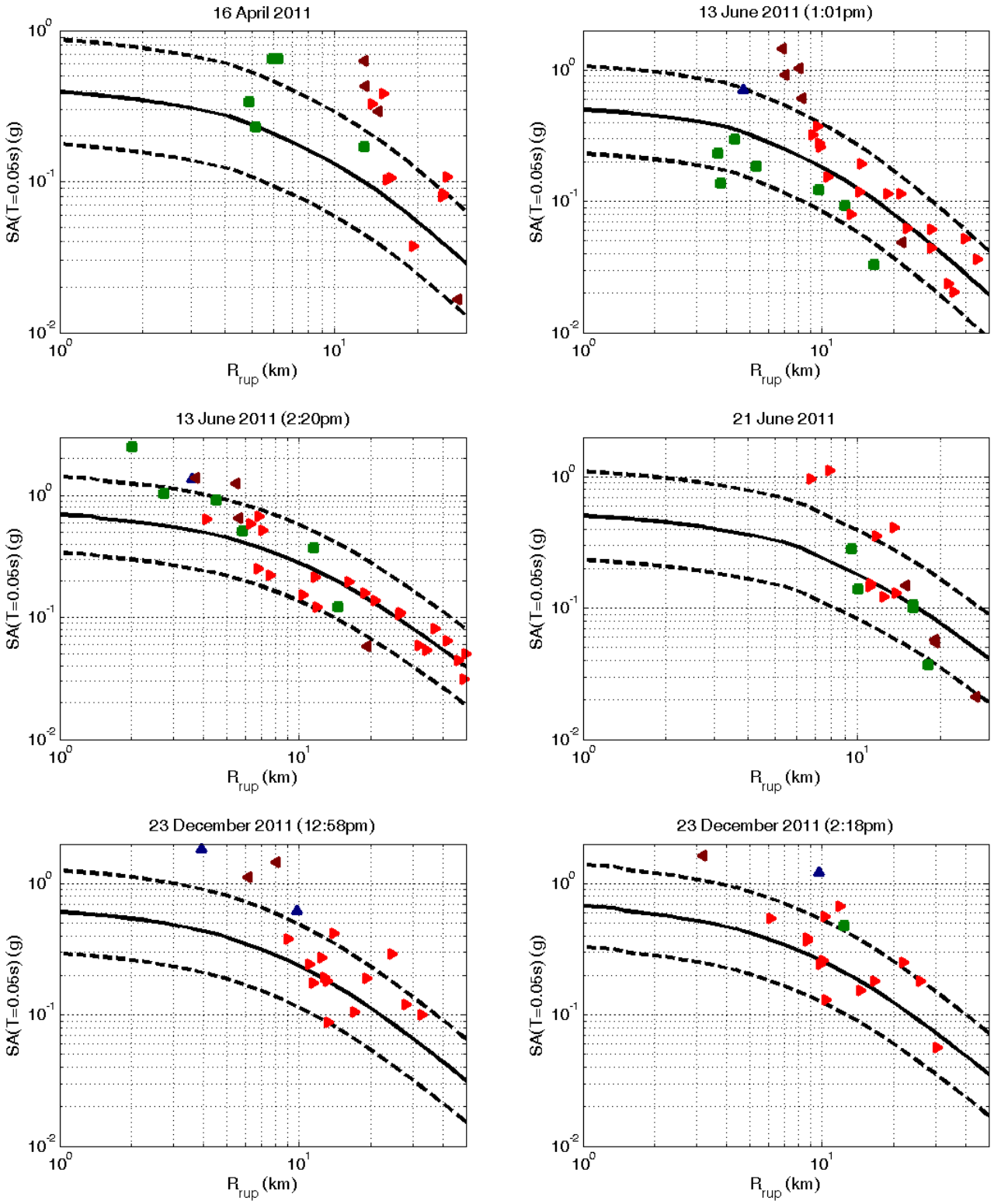

Figure 5: Mean spectral acceleration at T=0.05s plus and minus one standard deviation versus distance to rupture for the NGA-West2 suite of GMPEs, with records included as points

The pseudo-spectral acceleration (SA) from event *e*, at station *s*, is usually represented by:

$$lnSA_{es} = f_{es}(Site, Rup) + \delta B_e + \delta W_{es} \quad (1)$$

where $lnSA_{es}$ is the natural logarithm of the observed spectral acceleration; $f_{es}(\text{Site}, \text{Rup})$ is the median of the predicted logarithm of spectral acceleration as calculated using the empirical GMPE, which depends on the site and rupture being considered; δB_e is the between-event residual with zero mean and variance τ^2; and δW_{es} is the within-event residual with zero mean and variance ϕ^2.

Based on Equation 1, the distribution of SA is provided by:

$$lnSA_{es} \sim N(f_{es}, \tau^2 + \phi^2) \quad (2)$$

where $X \sim N(\mu_x, {\sigma_x}^2)$ is shorthand for X being normally distributed with mean μ_x and variance ${\sigma_x}^2$.

As stated previously, three of the four NGA-West2 GMPEs have no special considerations for use in New Zealand, and none of the GMPEs has special considerations for use in the Canterbury region. Therefore, the performance of these prediction equations was evaluated via comparison with the observed vertical ground motion amplitudes in the 2010-2011 Canterbury earthquakes and by specifically examining bias in the total logarithmic residual as a function of the predictor variables M_W, V_{S30} and R_{rup}.

The results of this analysis for M_W and V_{S30} are shown in Figure 6 and Figure 7, respectively. No clear trend in the total residual as a function of these predictor variables can be identified. Figure 6 shows whisker plots of the between-event residuals observed for each event according to magnitude. The median between-event residual for each observed value of M_W is within ±0.2 with the exceptions of the 16 April 2011 event ($M_W = 5.0$).

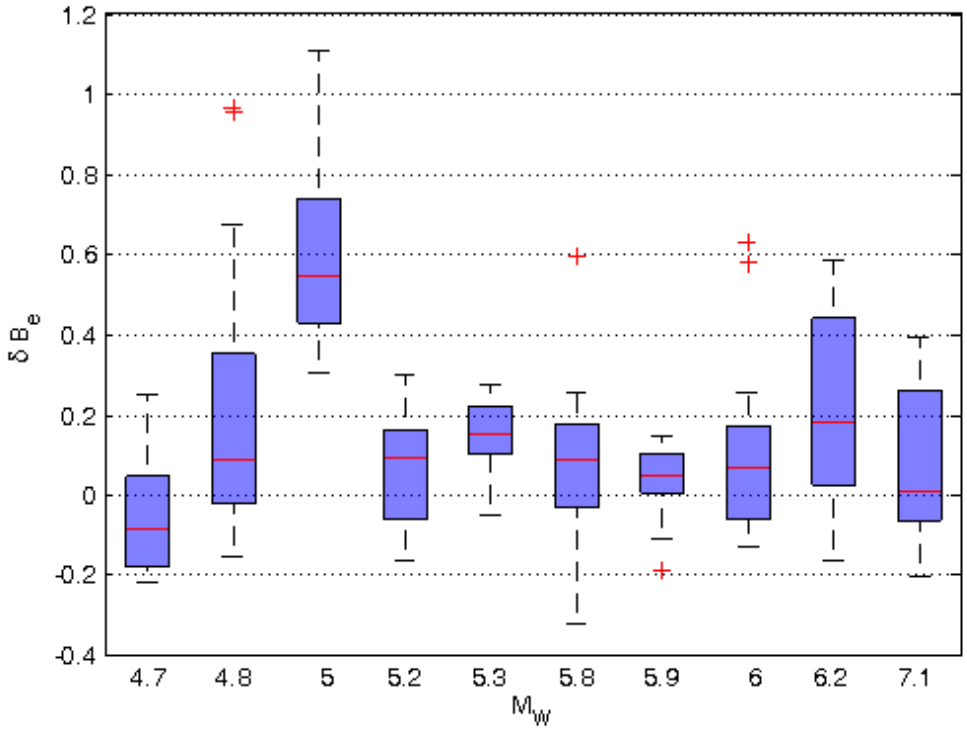

Figure 6: Whisker plots for between-event residuals for each event according to magnitude

Figure 7 shows whisker plots of the within-event residuals observed at each station according to their site class V_{S30}. The median within-event residual for each site class included is very near zero. The databases used to develop the NGA-West2 GMPEs include records from sites with V_{S30} values distributed between 100 and 1000 meters per second. This range includes all sites considered in this study. Combined with the lack of a trend in the residuals as a function of V_{S30}, this suggests that the NGA-West2 GMPEs do not exhibit V_{S30} bias when applied to the Canterbury region.

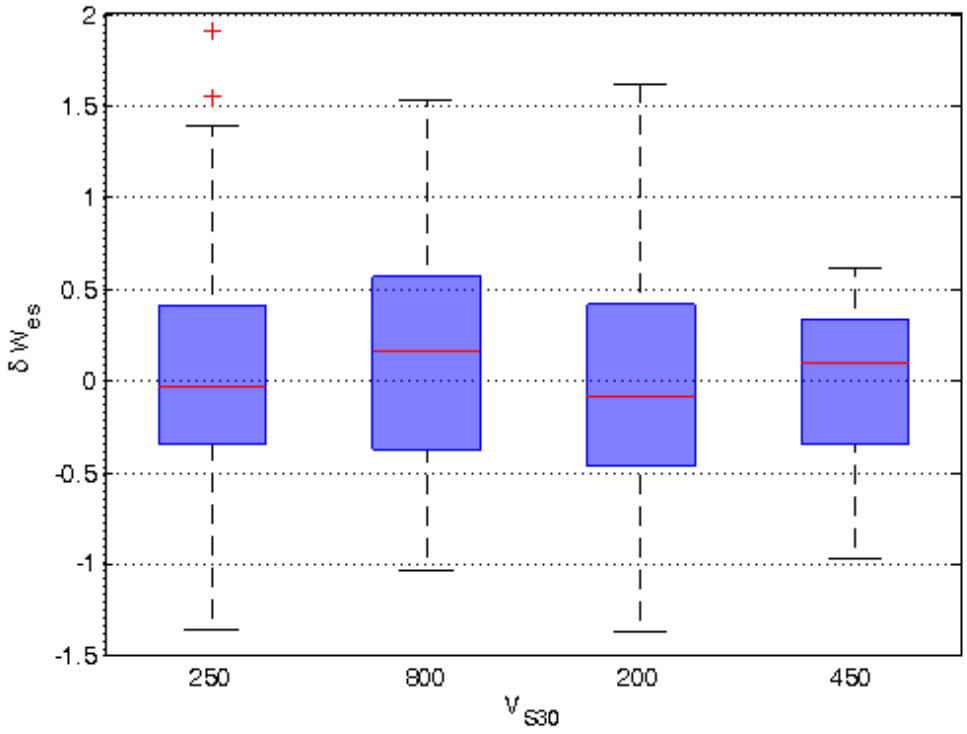

Figure 7: Whisker plots for within-event residuals according to site VS30

However, as shown in Figure 8, there is a clear trend in within-event residual as a function of R_{rup}. The rolling average of the within-event residuals is shown in black. The intensity of ground motion at sites less than 15 kilometers away from the rupture is systematically under-predicted when using the suite of NGA-West2 vertical GMPEs. This bias seems to decrease as a function of R_{rup}.

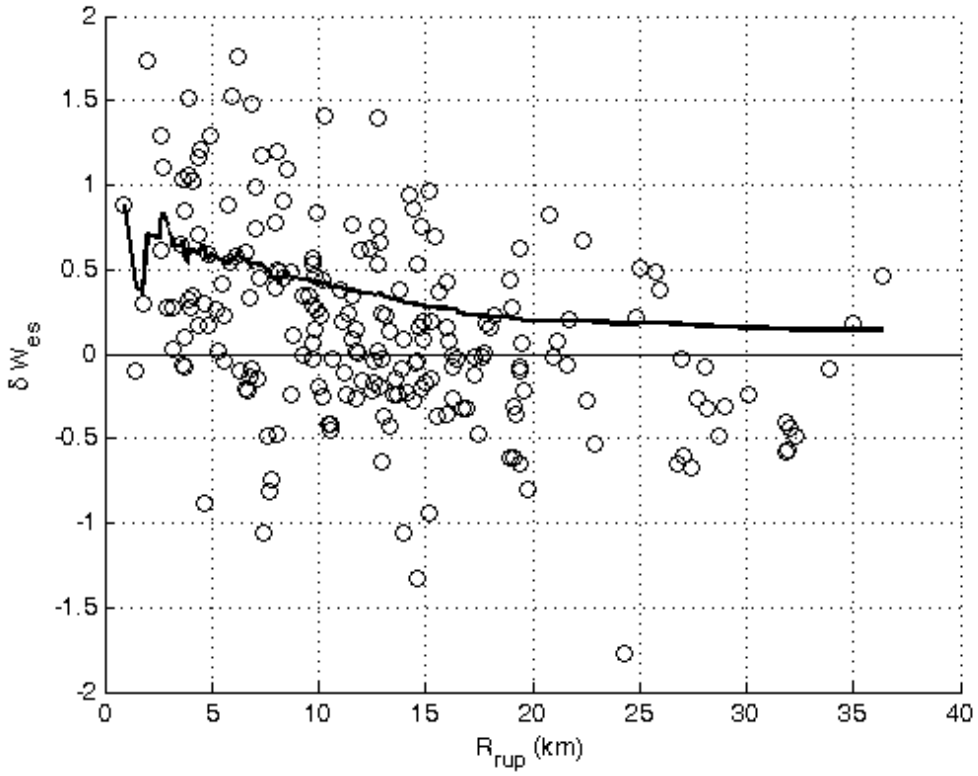

Figure 8: Median within-event residual values from all considered stations plotted against distance to rupture

The inter-event residuals for the selected events are plotted against vibration period in Figure 9. The location-to-location residual for the Canterbury earthquake sequence clearly indicates that the unadjusted NGA-West2 suite of vertical GMPEs systematically under-predicts vertical spectral acceleration at periods less than 0.1 seconds or greater than 1 second.

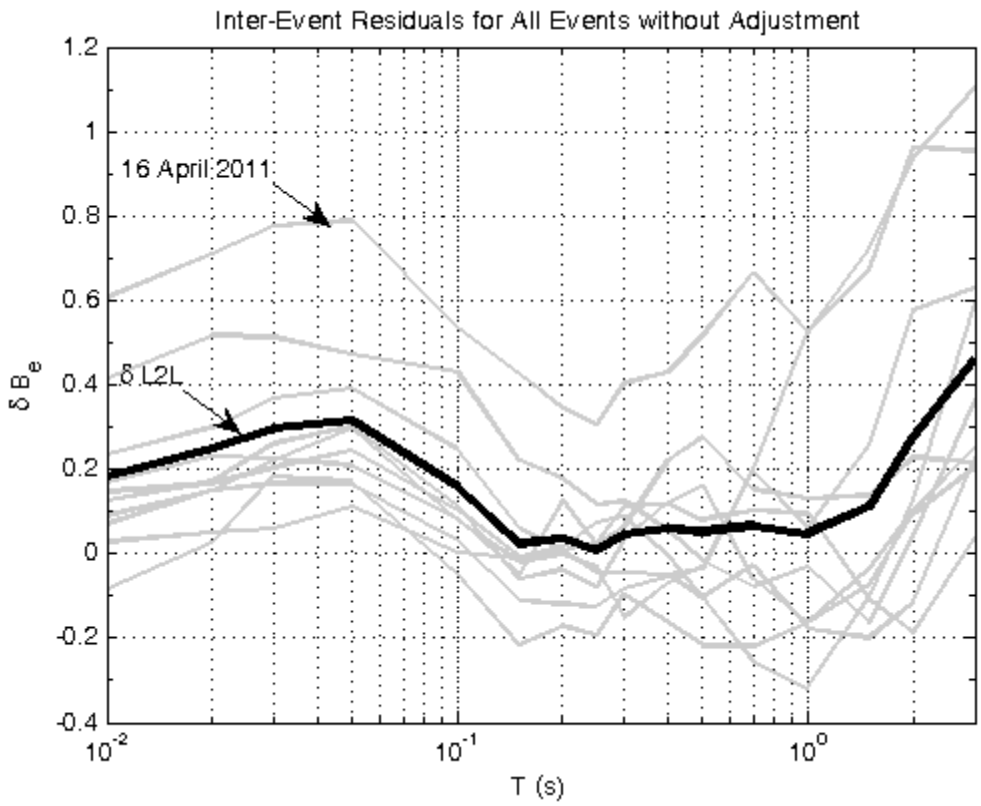

Figure 9: Inter-event residuals for all considered events before correction for distance-to-rupture bias

Based on the analysis presented in Figure 6, Figure 7, and Figure 8, the error in the NGA-West2 suite of GMPEs for predicting the vertical ground motion in the Canterbury region of New Zealand is caused principally by bias on distance-to-rupture. In order to attempt to identify the source of this bias, the M_W-R_{rup} space covered by the NGA-West2 GMPEs was compared to that covered by the records from the Canterbury earthquake sequence.

The distances-to-rupture of all records in the NGA-West2 database which were used in the development of each of the four NGA-West2 GMPEs versus the magnitudes of the events in which they were observed are shown in Figure 10. Figure 2.2 (Gülerce, Kamai, Abrahamson and Silva 2013), Figure 3.8 (Stewart, Seyhan, Boore and Atkinson 2013), Figure 4.1 (Bozorgnia and Campbell 2013), and Figure 5.1 (Chiou and Youngs 2013) from the NGA-West2 vertical ground motion attenuation report are reproduced.

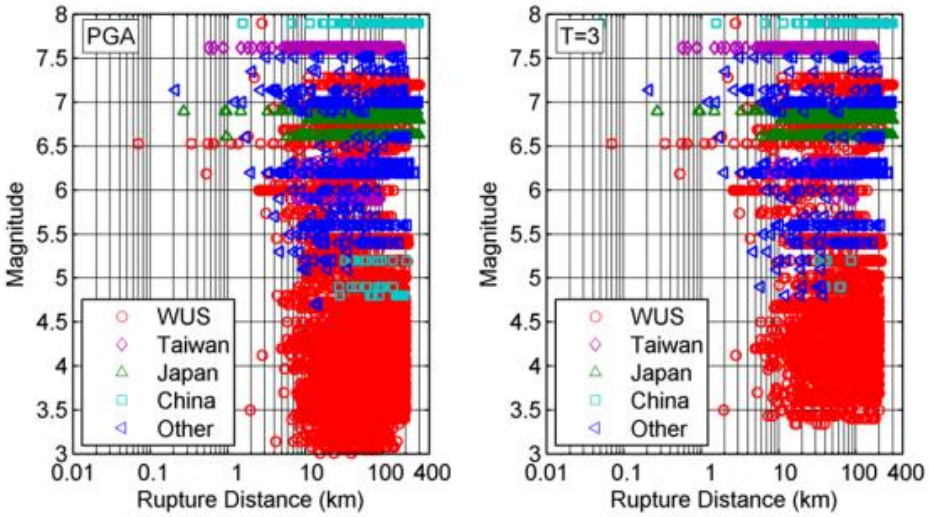

Figure 2.2 **Magnitude-distance distributions for the final subset.**

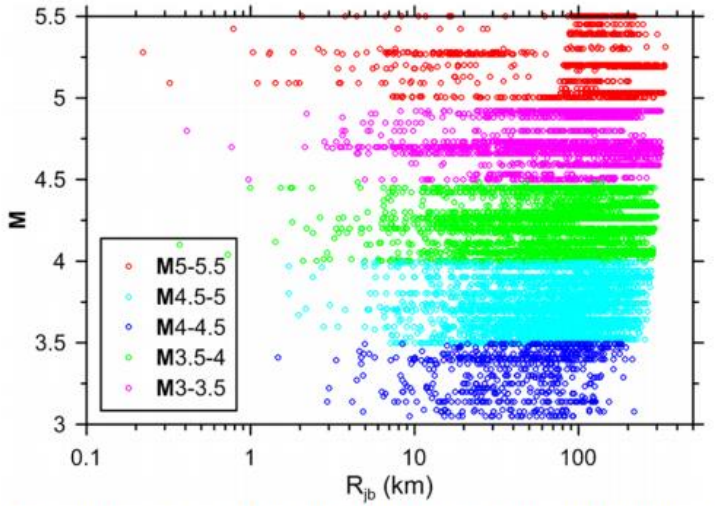

Figure 3.8 **Binned groups of California data in NGA-West 2 vertical flatfile used for constraint of apparent anelastic attenuation terms.**

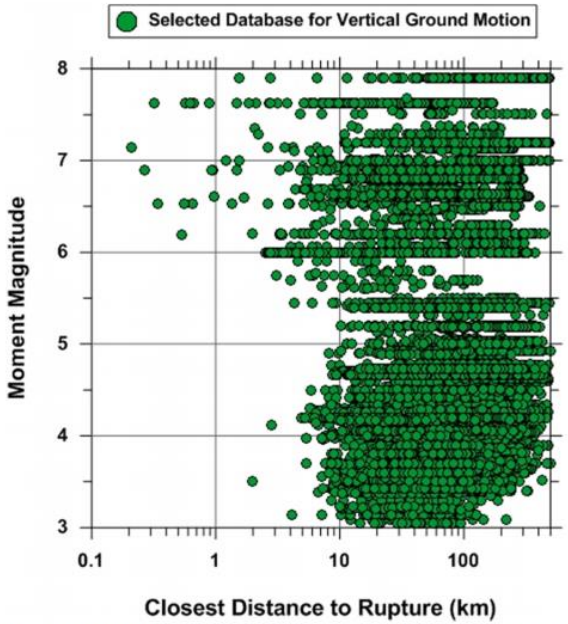

Figure 4.1 **Distribution of recordings with magnitude and distance for the BC13 vertical ground motion database.**

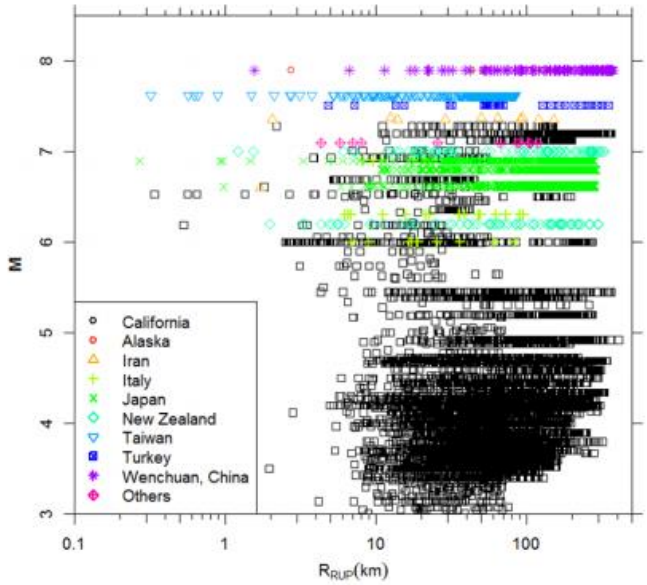

Figure 5.1 **Magnitude-distance-region distribution of selected records of vertical motion.**

Figure 10: Magnitude-distance content of the datasets used in development of the NGA-West2 vertical GMPEs

The distances-to-rupture of all records from each event in the Canterbury earthquake sequence plotted against the event's magnitude are illustrated in Figure 11. Records which were outside the prescribed R_{rup} limit given in Table 1 are shown in red. In general, more records from a greater range of distances are available from events with higher moment magnitude. The only exception to this trend is the 4 September 2010 event, the largest considered, which has recordings available from a narrower range of R_{rup} values than the next largest event.

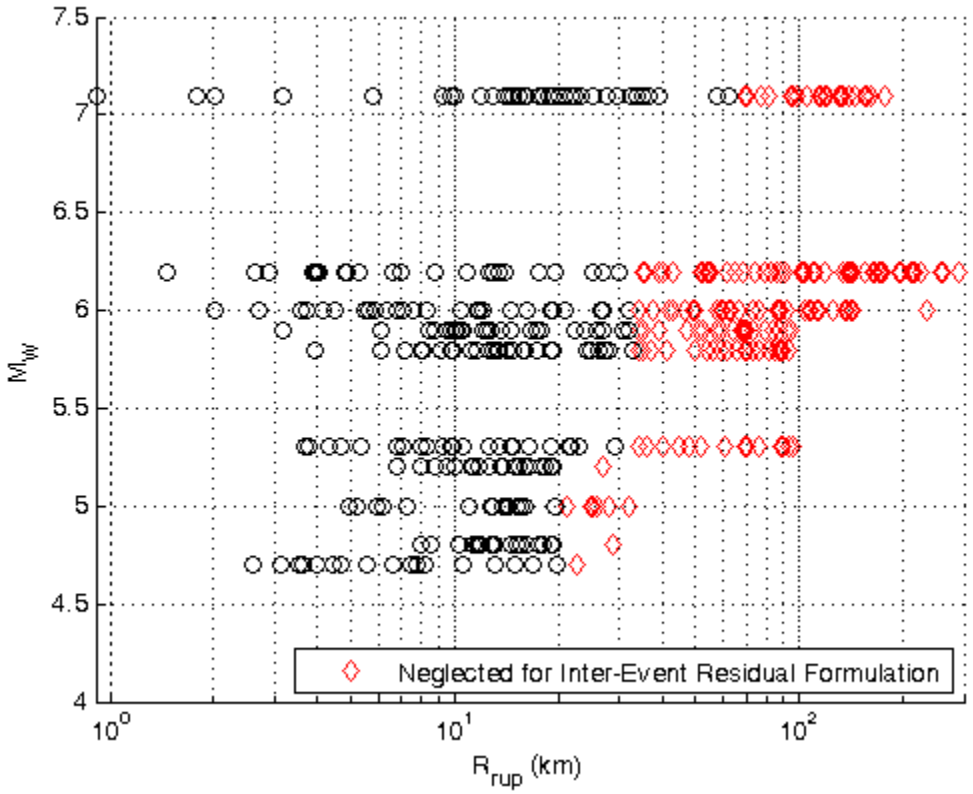

Figure 11: Magnitude-distance content of the records collected at the considered stations in the considered events

From a comparison of Figure 10 and Figure 11, it is clear that there are significant gaps in the database of records from the Canterbury earthquake sequence. The database used for the development of the NGA-West2 vertical GMPEs included many events of lower magnitudes, a more robust and granular assortment of event magnitudes, and more records from stations at greater distances-to-rupture for all magnitudes. However, a relatively small portion of the records considered in the NGA-West2 database are from stations within 10 kilometers of rupture. Due to the nature of the Canterbury earthquake sequence and the instrumentation in the region, a much larger portion of the records being considered in this study are very near the rupture. It is possible that this is a contributing factor to the observed R_{rup} bias. Additionally, some unique feature of the Canterbury basin which is not captured in the broadly located NGA-West2 databases may be contributing to the bias. This bias is of particular engineering significance because vertical motion is much more likely to contribute to structural damage at close fault distances (Silva 1997).

For all subsequent analysis, it will be necessary to assume that the between-event residuals, δB_e, and the within-event residuals, δW_{es}, are random variables with zero mean and some variance which are

independent of all predictor variables. Because it has been demonstrated that this is not the case when using the NGA-West2 suite of GMPEs as originally presented, it is necessary to develop an adjustment factor to remove distance-to-rupture bias and validate this assumption in order to perform non-ergodic analysis. This approach is similar to the one taken in Rodriguez-Marek et al (2011).

3.2 Adjustment for Distance to Rupture Bias

Due to the distance-to-rupture bias observed in the NGA-West2 vertical GMPEs when applied to earthquakes in the Canterbury region, an adjustment factor is needed. In order to determine an appropriate adjustment factor, a moving average of the total residuals, $z = dB_e + dW_{es}$, for all considered events with respect to distance to rupture was observed to have an approximately exponential shape, as shown in Figure 12.

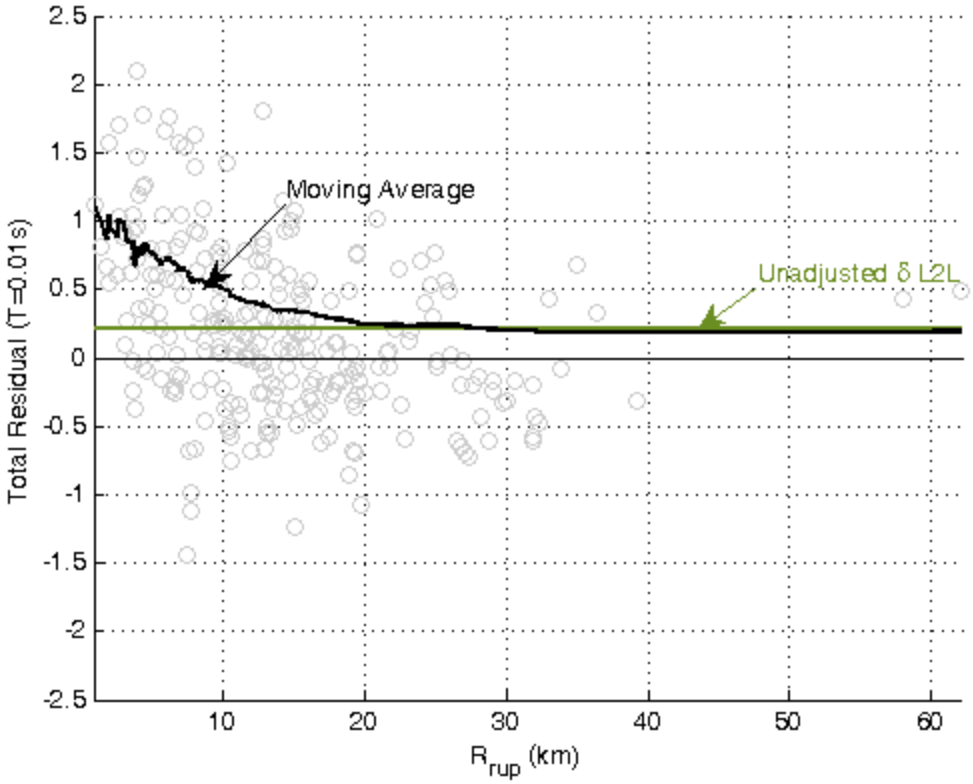

Figure 12: Illustration of the bias of the NGA-West2 suite of GMPEs with regard to distance-to-rupture when applied to records from the Canterbury region

The unadjusted systematic location-to-location residual for this vibration period taken from Figure 9 is also shown in green in Figure 12. Because the distance-to-rupture bias is being formulated using a moving average, the bias value at long periods is necessarily equivalent to the unadjusted value of *δL2L.* Distance-to-rupture bias is also pronounced in a similar scatterplot of the within-event residuals, shown in Figure 13. The bias evident in the within-event residuals is similar in shape to the bias evident in the total residuals. However, the bias in the within-event residuals is zero for high distances-to-rupture.

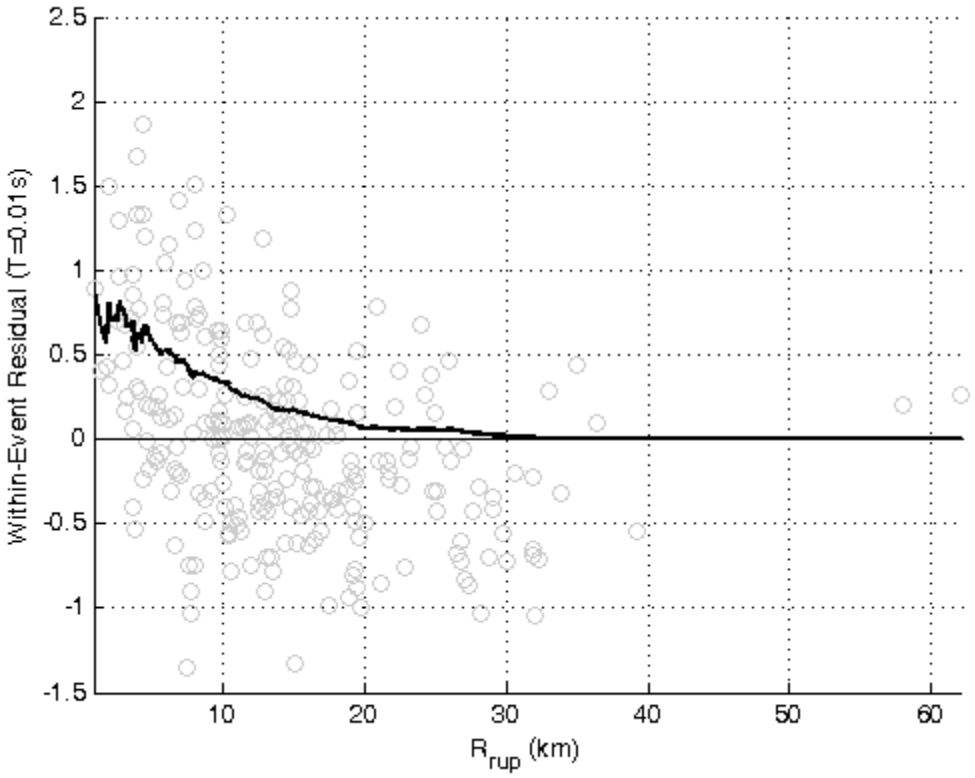

Figure 13: Within-event residuals for all considered stations and events versus distance-to-rupture

An adjustment factor was developed based on fitting an exponential function to the observed values of the bias. This function had the following form:

$$\hat{z} = Ae^{(-B*R_{rup})} + C \tag{3}$$

An adjusted value of predicted spectral acceleration would therefore be given by:

$$ln(SA_{adjusted}) = ln(SA_{original}) + \hat{z} \tag{4}$$

To avoid introducing bias at long distances to rupture, the value of C was constrained such that the function approaches the long distance to rupture bias. Values of A, B, and C were formulated for each vibration period being considered. These values were optimized to minimize the residual sum of squares between the derived bias value and the observed bias value. The residuals and the fitted bias value are shown in Figure 14.

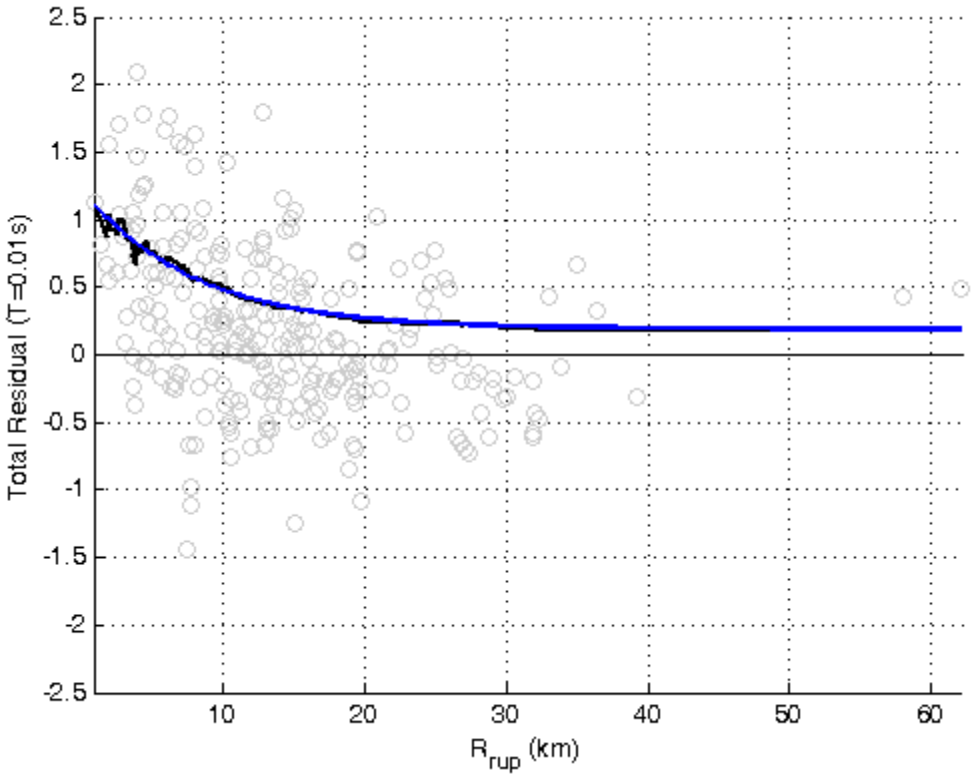

Figure 14: Total residuals versus distance-to-rupture with the proposed bias correction shown in blue

Because the large number of observations at distances to rupture of less than 15 kilometers results in a large weight assigned to the residual sum of squares for this range of R_{rup} values, the values of A, B, and C were constrained such that bias at long distances to rupture was removed completely. The coefficients for each vibration period are included in Table 4.

Table 4: Period-specific coefficients of the empirical distance-to-rupture bias correction

T (s)	A	B	C
0.00	1.268	0.129	-0.081
0.01	1.035	0.127	-0.0696
0.02	1.177	0.131	-0.0236
0.03	1.172	0.137	0.0388
0.05	1.078	0.136	0.074
0.1	0.981	0.096	-0.1605
0.15	0.804	0.09	-0.2583
0.2	0.82	0.096	-0.2385
0.25	0.633	0.074	-0.2566
0.3	0.732	0.093	-0.2039
0.4	0.78	0.106	-0.1742
0.5	0.586	0.087	-0.1651
0.7	0.517	0.101	-0.0986
1	0.219	0.056	-0.0772
1.5	0.09	0.04	0.0429
2	0.022	-0.008	0.2443
3	0.042	0.095	0.4653

After adjustment, very little bias in the total residuals is caused by distance to rupture, as shown in Figure 15. For all subsequent analysis, bias is therefore assumed to be independent of all predictor variables in the ground motion prediction equations.

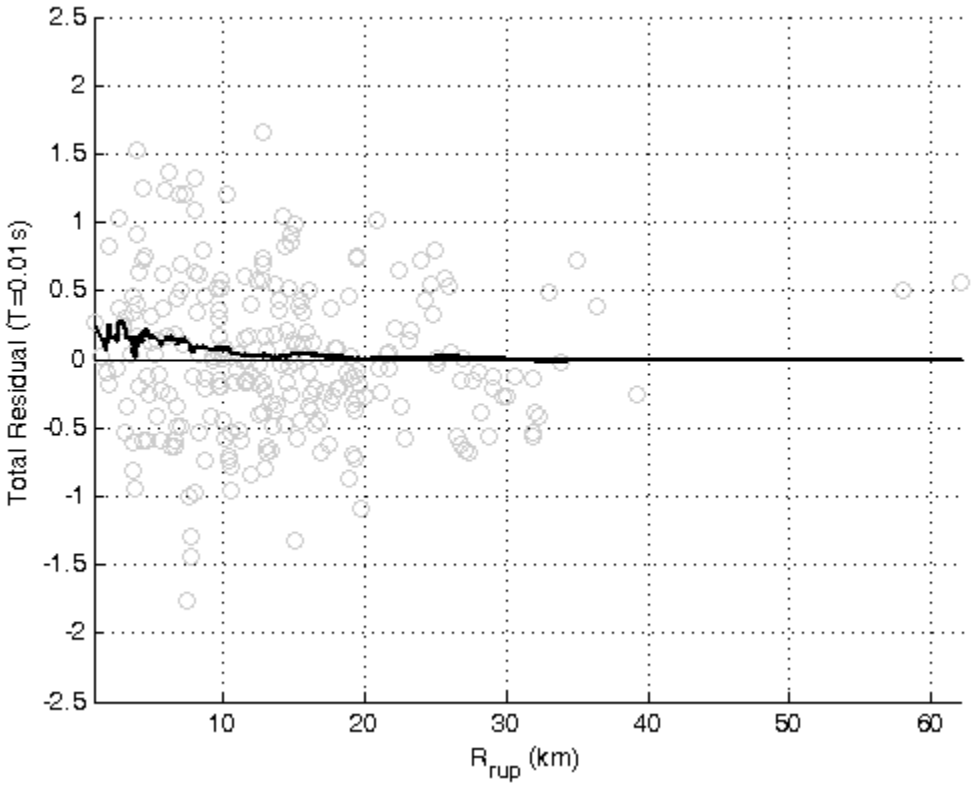

Figure 15: Total residual versus distance-to-rupture following the application of the empirical bias correction

Similarly, the adjusted within-event residuals were also substantially reduced, as shown in Figure 16. As before, the bias of the within-event residuals at high distances-to-rupture is zero.

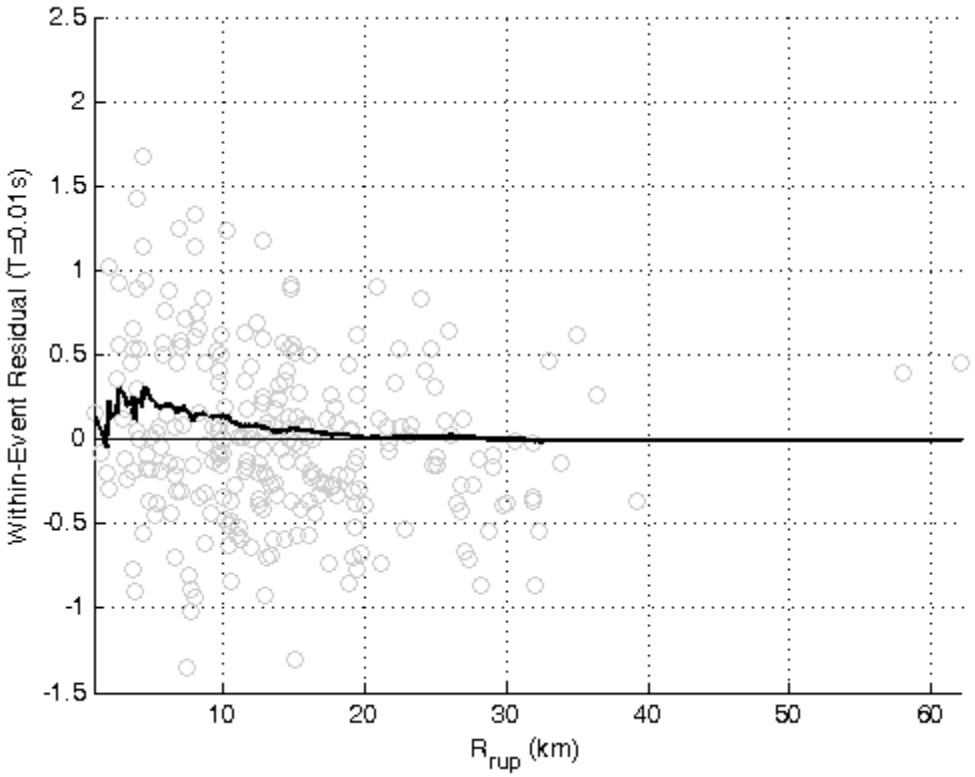

Figure 16: Within-event residuals versus distance-to-rupture following the application of the empirical bias correction

The coefficients used in this empirical bias adjustment are shown plotted as a function of vibration period in Figure 17. Due to the optimization methodology used, the trends in these coefficients are quite jagged. However, large-scale trends are identifiable with a few exceptions such as the value of B at $T = 3.0s$. Functional forms of these coefficients could be derived in terms of vibration period and used in place of the derived values tabulated above.

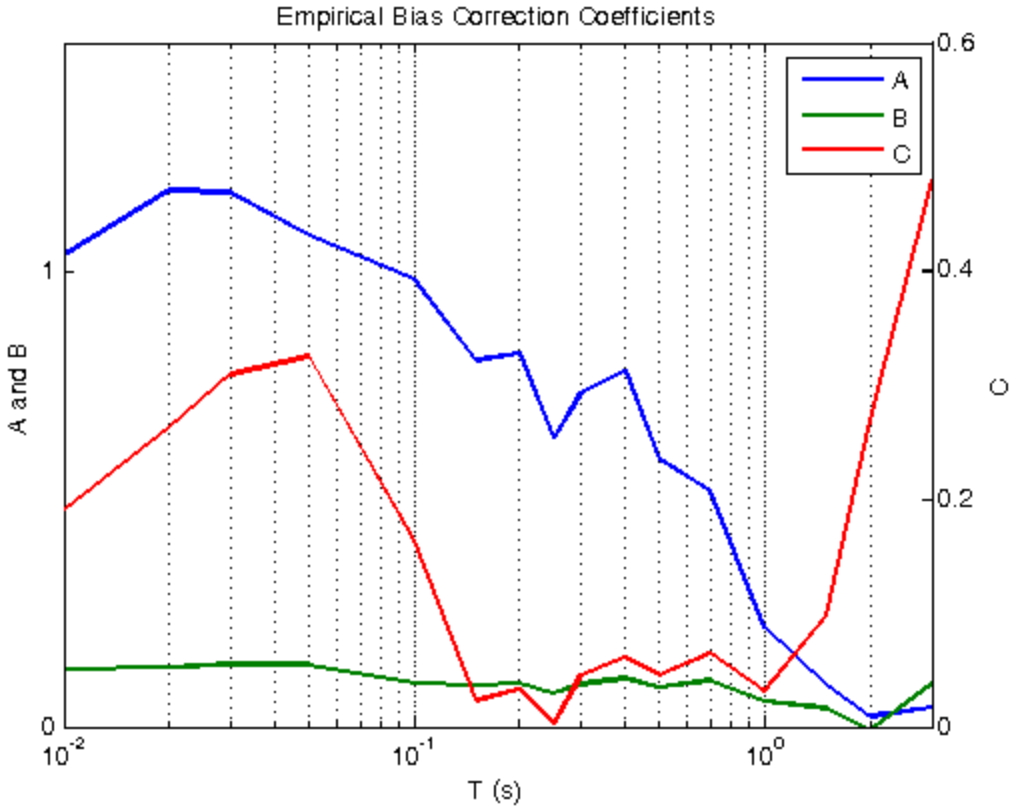

Figure 17: Coefficients of the empirical distance-to-rupture bias correction plotted against vibration period

As can be seen from Figure 17, the value of the coefficient A, which governs the magnitude of the R_{rup}-dependent portion of the correction, decreases with vibration period. This is expected due to the influence of surface waves and the shallow water table at low periods. The value of coefficient C increases at long periods, potentially due to the geometry of the basin and its effect on the contribution of Rayleigh waves to vertical motion.

Plots of the distance-to-rupture bias adjustment factor against vibration period for a selection of distance-to-rupture values are presented in Figure 18. It can be seen that the adjustment is largest for low distances to rupture. The adjustment is flattest for higher distances to rupture.

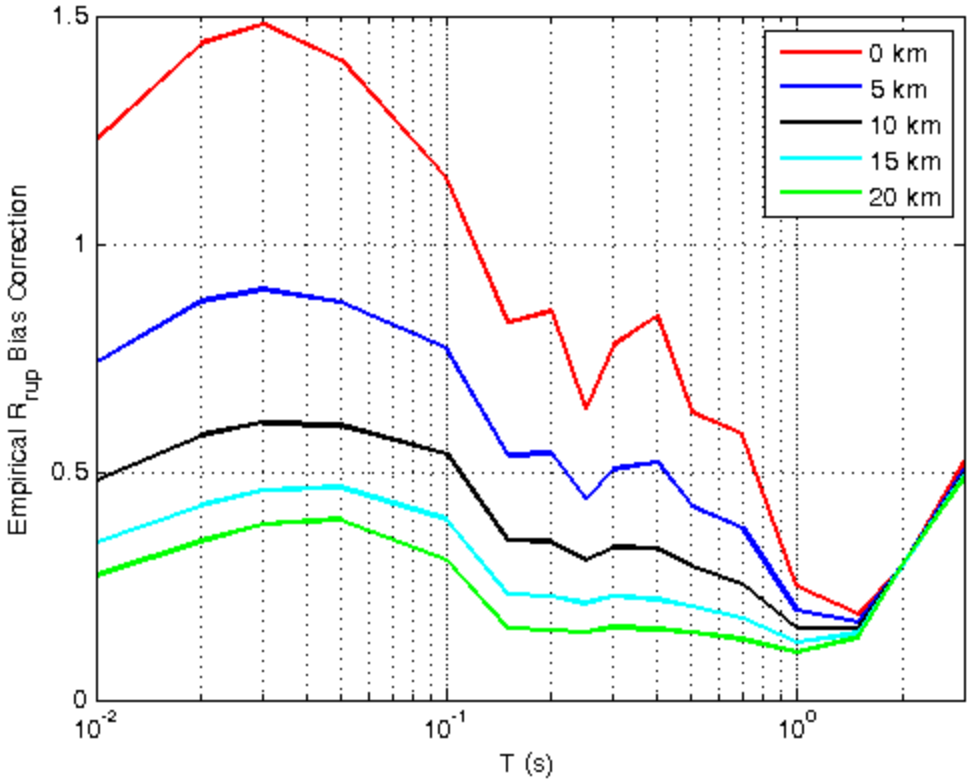

Figure 18: Empirical distance-to-rupture bias correction versus vibration period for selected values of Rrup

3.3 Evaluation of the Performance of the Adjusted NGA-West2 Ground Motion Prediction Equations

The performance of the corrected suite of NGA-West2 GMPEs for each considered event is illustrated in Figure 19. The performance of the original NGA-West2 GMPEs is shown in grey.

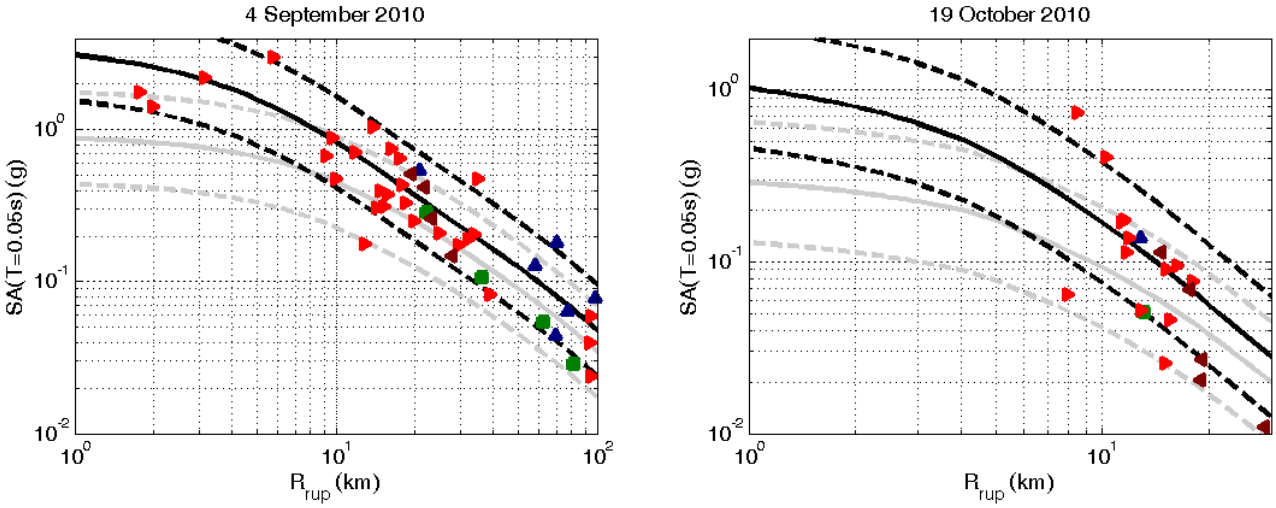

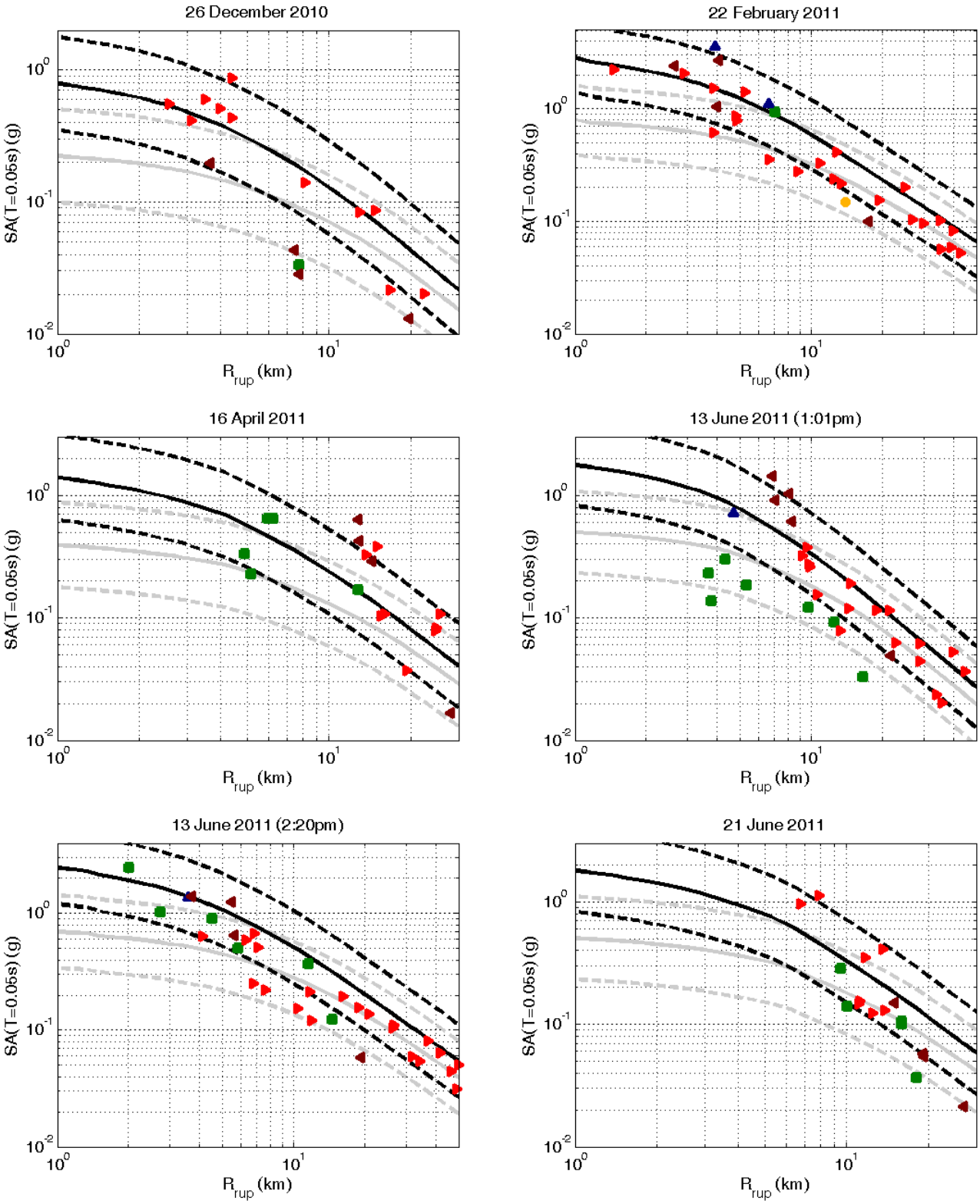
26 December 2010
22 February 2011
16 April 2011
13 June 2011 (1:01pm)
13 June 2011 (2:20pm)
21 June 2011
SA(T=0.05s) (g)
R_rup (km)
10^0
10^-1
10^-2
10^1

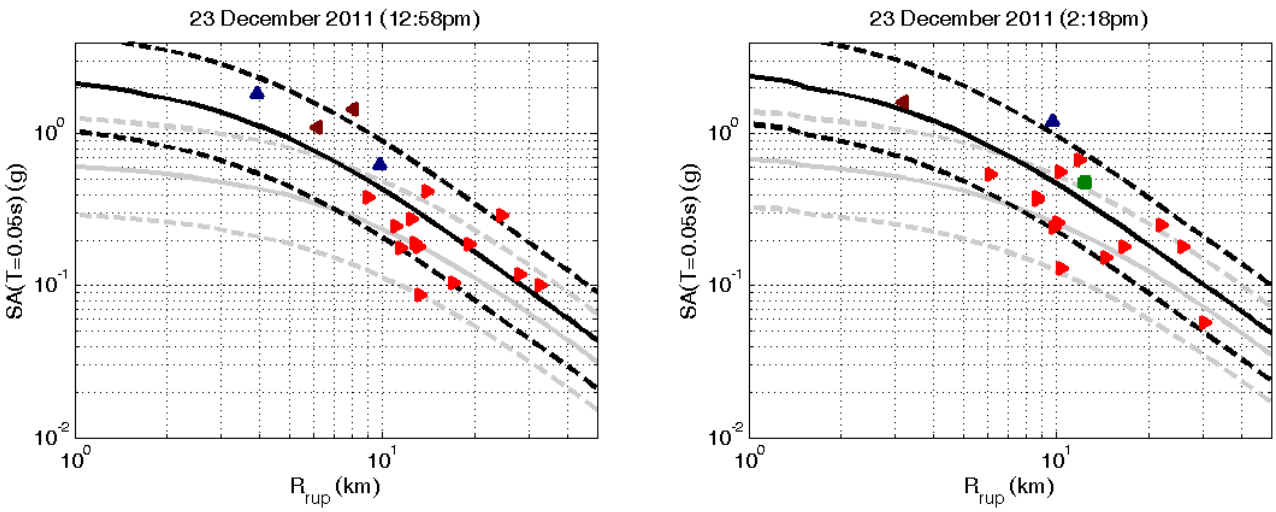

Figure 19: Mean spectral acceleration at T=0.05s plus and minus one standard deviation versus distance to rupture for the adjusted NGA-West2 suite of GMPEs, with records included as points and the unadjusted NGA-West2 suite of GMPEs shown in grey

In order to illustrate that the adjusted NGA-West2 GMPEs do not exhibit any bias with regard to the principal input variables R_{rup}, M_W, and V_{S30}, the analysis performed earlier to identify bias in the unadjusted GMPEs was repeated. The results of this analysis are shown in Figure 20, Figure 21, and Figure 22.

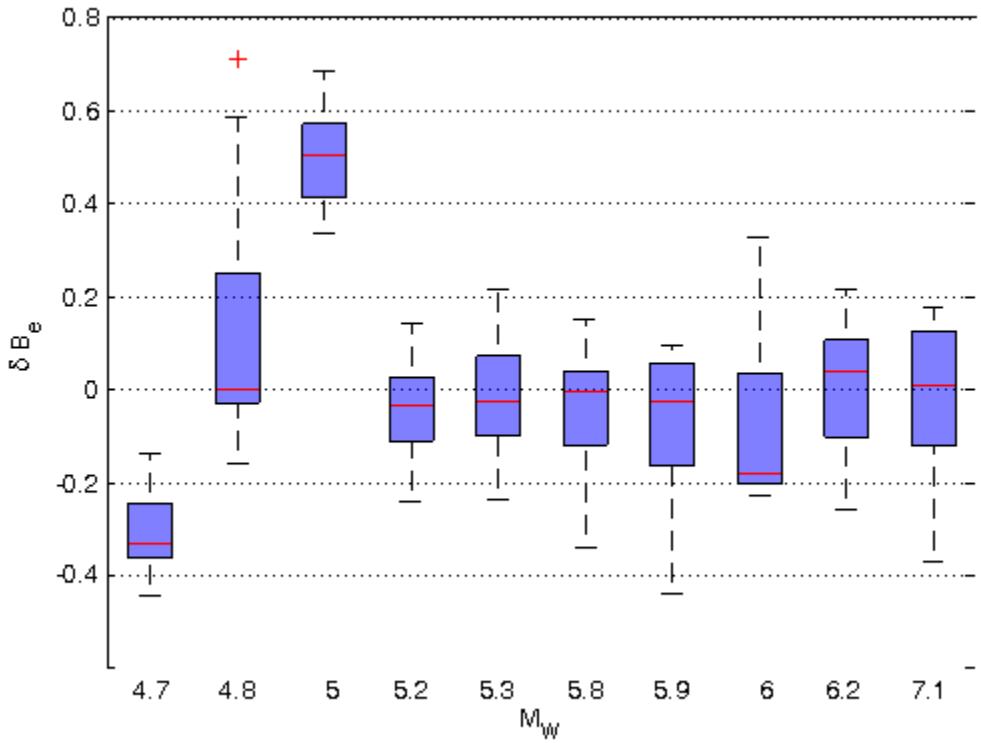

Figure 20: Whisker plots showing between-event residuals for all events according to magnitude after adjustment

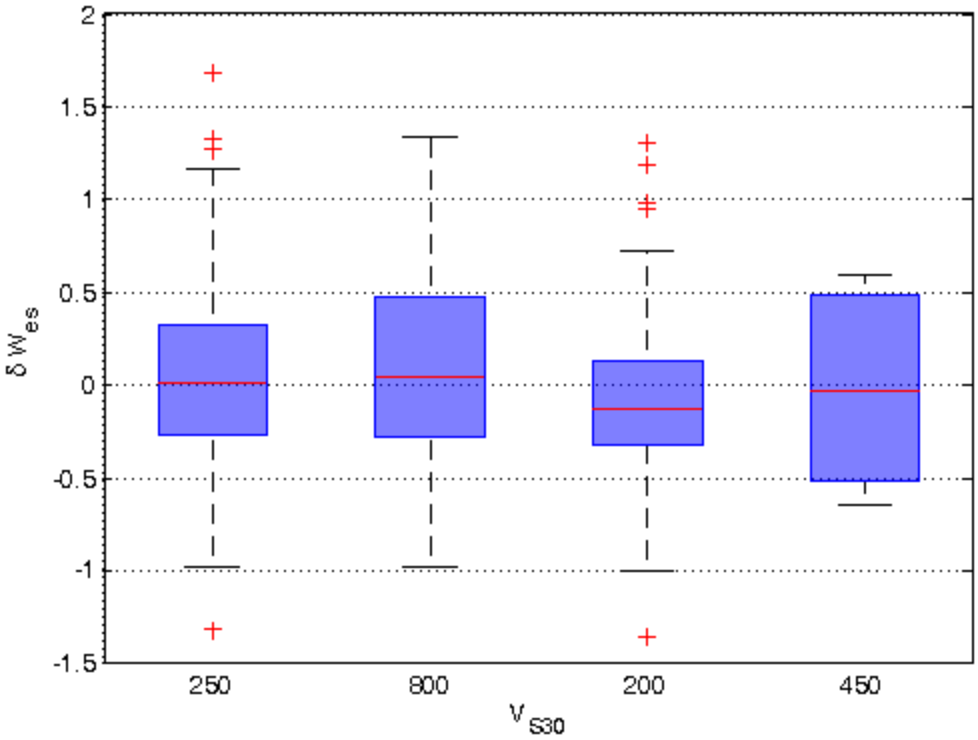

Figure 21: Whisker plots showing all within-event residuals according to site VS30 after adjustment

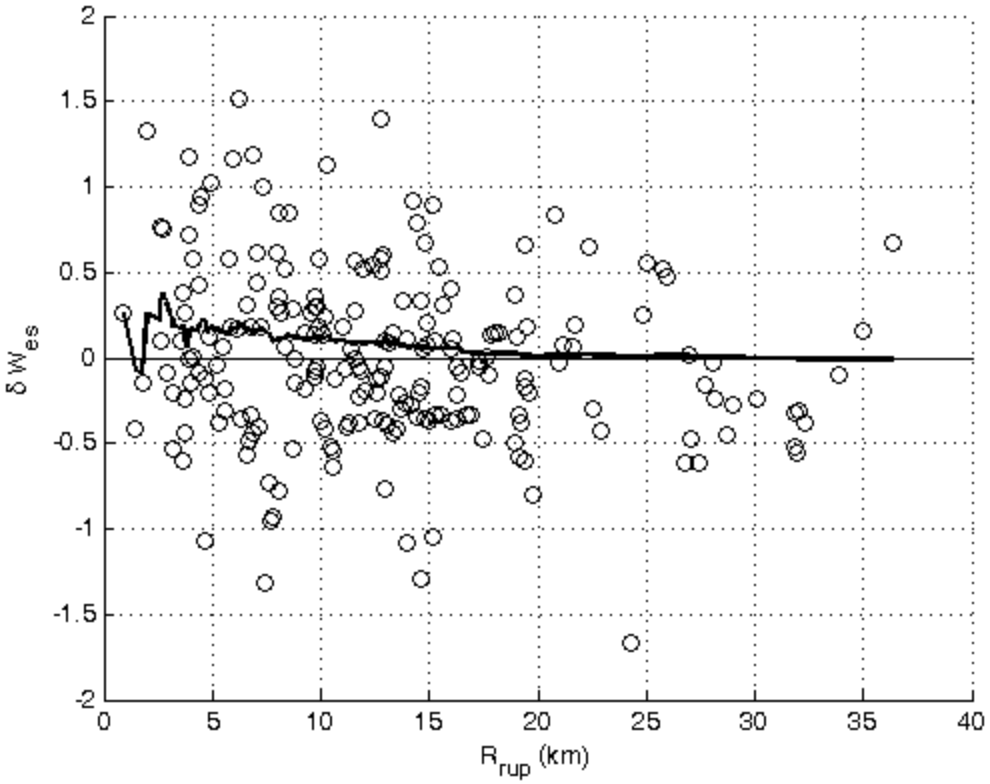

Figure 22: Median within-event residual versus distance-to-rupture after adjustment

As before, no bias stemming from M_W or V_{S30} is evident. However, the bias due to R_{rup} has been greatly reduced.

4 Sensitivity of Results to the Scope of the Study

4.1 Sensitivity of Results to the Distance Limits

The authors were concerned that the analysis of the systematic effects in the vertical components in the Canterbury earthquake sequence might be sensitive to very weak records observed at great distances to rupture. For this reason, the limits on distance to rupture for consideration of records from each event were lowered by a factor of two thirds relative to the limits previously used for analysis of the horizontal components. All analysis heretofore was performed using the newly reduced limits. A comparison of the results for the inter-event residuals formulated using the current R_{rup} limits with those formulated using the original limits is shown in Figure 26. This figure illustrates a comparison of the inter-event residuals for each event at each considered vibration period. Each event is depicted in a different color.

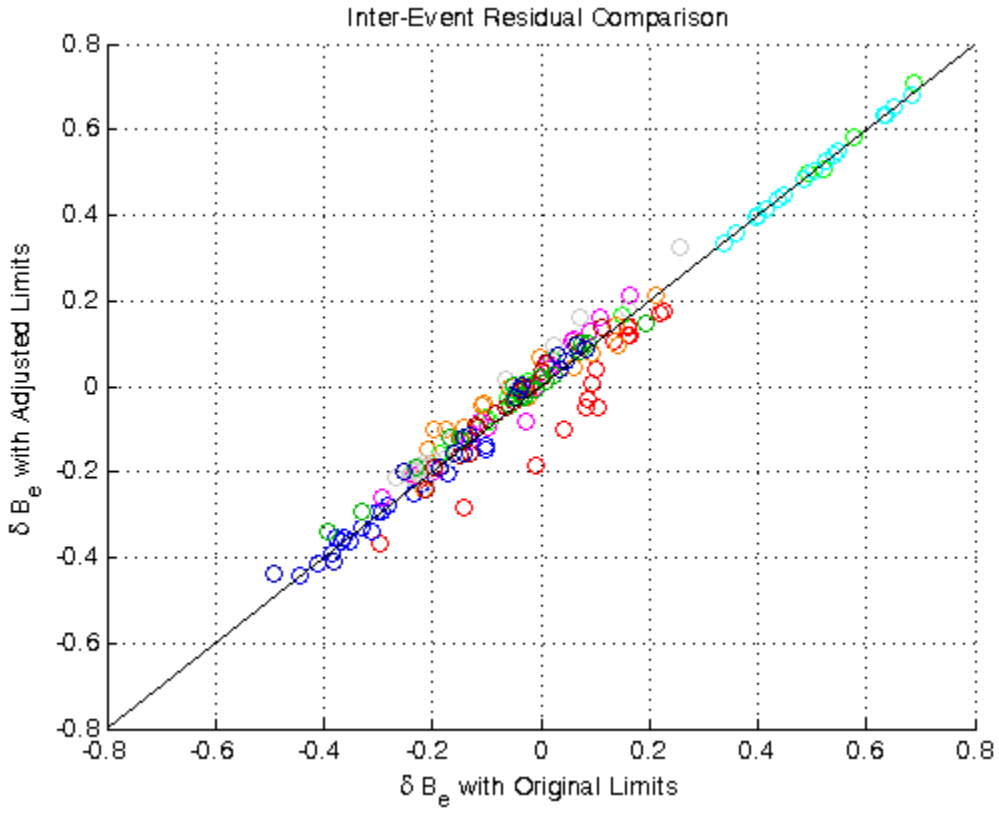

Figure 23: Comparison of inter-event residuals using the adjusted distance-to-rupture limits and the original limits

The changes observed based on altering the distance to rupture limits was very small, except in the case of the 4 September 2010 event, shown in red, which experienced a slight reduction in inter-event residual for most periods considered. This is likely because the Darfield event has the most records available for analysis, and experienced the greatest change in the number of records being considered when the limits were adjusted. The change in number of records considered is shown in Table 5.

Table 5: Comparison of the adjusted distance-to-rupture limits with the original limits for all considered events

Event date	Original Rrup (km)	Original Num Records	Adjusted Rrup (km)	Adjusted Num Records	Percent Decrease	Estimated VPGA at Rrup Limit (g)
4 September 2010	100	44	67	36	-19%	0.039
19 October 2010	30	20	20	20	-	0.018
26 December 2010	30	19	20	19	-	0.015
22 February 2011	50	29	34	24	-18%	0.047
16 April 2011	30	24	20	24	-	0.012
13 June 2011 (1:01pm)	50	31	34	26	-17%	0.020
13 June 2011 (2:20pm)	50	34	34	28	-18%	0.040
21 June 2011	30	22	20	22	-	0.035
23 December 2011 (12:58pm)	50	33	34	28	-16%	0.034
23 December 2011 (2:18pm)	50	31	34	27	-13%	0.037

An estimate of the vertical peak ground acceleration at a typical site located at the adjusted maximum R_{rup} bound for an event of the given magnitude is also included in Table 5. These values are on the order of 0.04g or less. Records with an intensity lower than this are unlikely to cause significant damage.

Despite the apparent insensitivity to changing these limits, the new limits have been adopted for the purposes of this study of vertical motion. Although only the Darfield event is affected significantly by this phenomenon in this study, records with a small amplitude recorded at a long distance to rupture tend to be poorly predicted and therefore should be excluded in order to prevent their having a disproportionate influence on the observed systematic effects. The new limits were used in all analysis of vertical motion up to this point as well as in all subsequent analysis.

4.2 Sensitivity of Results to the Inclusion or Exclusion of the Port Hills Stations

The stations located in the Port Hills region are of special concern for this study. These stations are GODS, PARS, STKS, D14C, and MTPS. No records from these stations exist from the 22 February 2011 earthquake or before. The Port Hills stations have experienced relatively large ground motions in all of the considered events for which they have records, as was shown in Table 1 above.

Excluding these stations from consideration when calculating the between-event residuals tends to decrease the between-event residuals, as shown in Figure 24. Except in the case of the earlier of the two 13 June 2011 events, this effect seems fairly uniform.

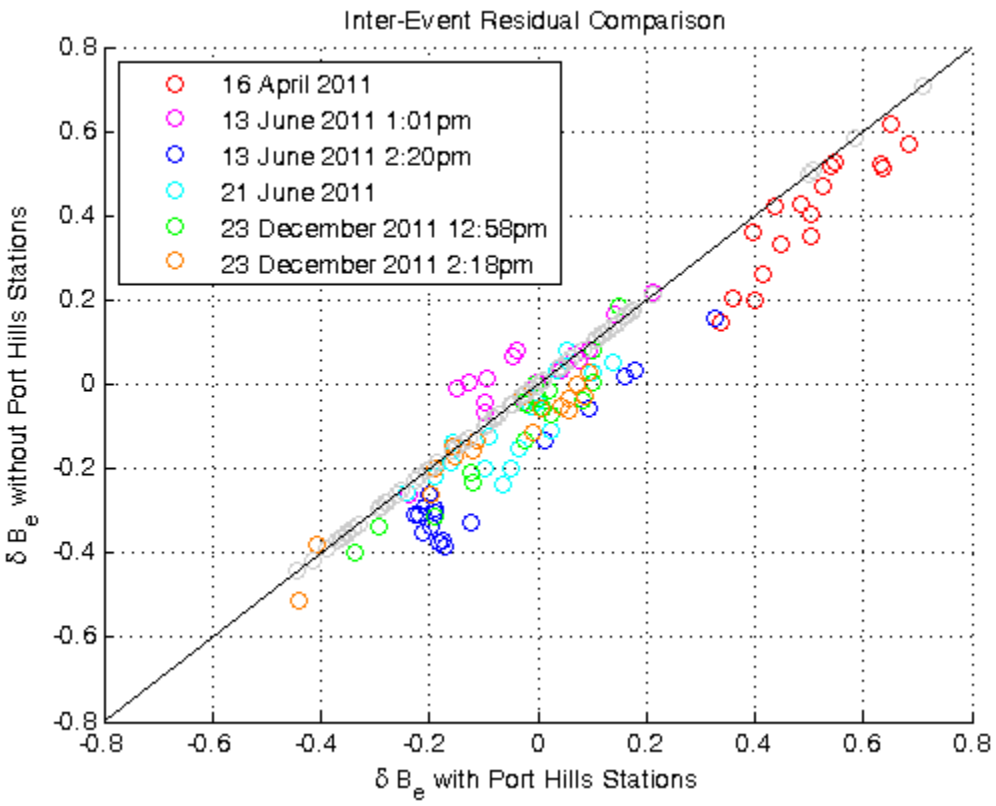

Figure 24: Comparison of inter-event residuals including and excluding the Port Hills stations from consideration

The Port Hills stations have been included in the formulation of the between-event residuals for the purposes of this study. The source of this behavior in the Port Hills stations is expected to be topographic effects, which are not captured in the ground motion prediction equations.

5 Non-Ergodic Ground Motion Prediction

The same methodology used in Bradley (2013) for decomposing the residuals into their between-event and within-event components was used for calculating δB_e and δW_{es}. The systematic location-to-location residual, $\delta L2L_l$ and systematic site-to-site residual, $\delta S2S_s$, as well as the components of the between-event standard deviation, τ_{L2L_l} and τ_0, and the components of the within-event standard deviations, ϕ_{S2S} and ϕ_0, were also calculated using the same method. The non-ergodic prediction can be expressed as:

$$lnSA_{es} = f_{es}(Site, Rup) + (\delta L2L_l + \delta B^0{}_{el}) + (\delta S2S_s + \delta W^0{}_{es}) \quad (5)$$

The $f_{es}(Site, Rup)$ component of Equation 5 is the mean of the four $lnSA_{es}$ predictions produced by the corrected suite of NGA-West2 vertical GMPEs. The methodology for calculating the remaining terms of Equation 5 follows, paraphrased from Bradley (2013).

5.1 Between-Event Residual and Its Components

The between-event residual, δB_e, is comprised of two components. The first is the systematic location-to-location residual, which can be calculated as the mean of the between-event residuals:

$$\delta L2L_l = \frac{1}{NE}\sum_{e=1}^{NE} \delta B_e \quad (6)$$

The NE term seen in Equation 6 is the total number of events considered ($NE = 10$ for this analysis). For each event, the remaining portion of the between-event residual is simple to calculate:

$$\delta B^0{}_{el} = \delta B_e - \delta L2L_l \quad (7)$$

Because $\delta L2L_l$ is the mean of δB_e, $\delta B^0{}_{el}$ has axiomatically zero mean. Additionally, both $\delta L2L_l$ and $\delta B^0{}_{el}$ carry a degree of uncertainty. The uncertainty in the systematic location-to-location residual stems from the fact that it has been formulated based on a finite sample of events. Its variance can be computed as:

$$Var[\delta L2L_l] = \tau_{L2L_l}^2 = \frac{\hat{\tau}^2}{NE} \quad (8)$$

In Equation 8, $\hat{\tau}^2$ is the sample variance of the between-event residuals, δB_e. The variance of the remaining portion of the between-event residuals, $\delta B^0{}_{el}$, can be computed from statistical inference:

$$\tau_{l0}^2 = Var[\delta B^0{}_{el}] = \frac{1}{NE-1}\sum_{e=1}^{NE}(\delta B^0{}_{el})^2 \quad (9)$$

5.2 Within-Event Residual and Its Components

Likewise, the within-event residual, δW_{es}, can also be decomposed into two portions. The first is the systematic site-to-site residual, which can be calculated as the average within-event residual for the given station in all considered events:

$$\delta S2S_s = \frac{1}{NE_s}\sum_{e=1}^{NE_s} \delta W_{es} \quad (10)$$

The NE_s term in Equation 10 is the number of events which have recordings at station *s*. The remaining portion of the within-event residual at each station in each event can similarly be computed as:

$$\delta W^0{}_{es} = \delta W_{es} - \delta S2S_s \quad (11)$$

Again, the remaining portion of the within-event residual, $\delta W^0{}_{es}$, has zero mean by definition. Additionally, both $\delta S2S_s$ and $\delta W^0{}_{es}$ carry a degree of uncertainty. The uncertainty in the systematic site-to-site residual stems from the fact that it has been formulated based on a finite sample of events. Its variance can be computed as:

$$Var[\delta S2S_s] = \phi_{S2S_s}^2 = \frac{\hat{\phi}^2}{NE_s} \quad (12)$$

In Equation 12, the $\hat{\phi}^2$ term is the sample variance of the within-event residuals, δW_{es}. The variance of the remaining portion of the between-event residuals, $\delta B^0{}_{el}$, can be computed from statistical inference:

$$\phi_{s0}^2 = Var[\delta W^0{}_{es}] = \frac{1}{NE_s-1}\sum_{e=1}^{NE_s}(\delta W^0{}_{es})^2 \quad (13)$$

5.3 Non-Ergodic Prediction

Having calculated the components of the between- and within-event residuals, it is now possible to calculate the mean and variance of the non-ergodic GMPE. The mean value of $lnSA_{es}$ is given by:

$$E[lnSA_{es}] = f_{es} + \delta L2L_l + \delta S2S_s \quad (14)$$

because $E[\delta B^0{}_{el}] = E[\delta W^0{}_{es}] = 0$. Because SA_{es} is lognormally distributed, the median value of SA_{es} can be calculated as the exponential of the mean of $lnSA_{es}$.

$$Median[SA_{es}] = exp(E[lnSA_{es}]) \quad (15)$$

As was the case in Bradley (2013), it is useful to consider the "systematic amplification factor," or the ratio between the non-ergodic and ergodic predictions, which results from inclusion of the systematic location-to-location and site-to-site residuals. This amplification factor is given by:

$$\frac{Median[SA_{es}]_{nonergodic}}{Median[SA_{es}]_{ergodic}} = exp(\delta L2L_l + \delta S2S_s) \quad (16)$$

Making the conventional assumption that the between-event and within-event standard deviations are uncorrelated, the non-ergodic prediction variance can be obtained as:

$$Var[lnSA_{es}] = \left(\tau^2_{L2L_l} + \tau^2_{l0}\right) + \left(\phi^2_{S2S_s} + \phi^2_{s0}\right) \quad (17)$$

For each of the between-event, within-event, and total residuals, a standard deviation reduction factor can be computed for the ratio of the non-ergodic and ergodic standard deviations:

$$RF_\tau = \sqrt{\frac{\tau^2_{L2L_l} + \tau^2_{l0}}{\tau^2}} \quad (18)$$

$$RF_\phi = \sqrt{\frac{\phi^2_{S2S_s} + \phi^2_{s0}}{\phi^2}} \quad (19)$$

$$RF_{\sigma_T} = \sqrt{\frac{\left(\tau^2_{L2L_l} + \tau^2_{l0}\right) + \phi^2_{S2S_s} + \phi^2_{s0}}{\tau^2 + \phi^2}} \quad (20)$$

6 Observed Systematic Effects in the Vertical Components of the Canterbury Earthquakes

6.1 Between-Event Residuals

Figure 25 shows the inter-event residuals for each of the events considered plotted as a function of vibration period. The systematic location-to-location residual, *δL2L* is shown as well. For periods between 0.01 and 3 seconds, *δL2L* is approximately zero. This confirms that the corrected NGA-West2 GMPEs, which have been adjusted to remove R_{rup} bias, are unbiased for short periods.

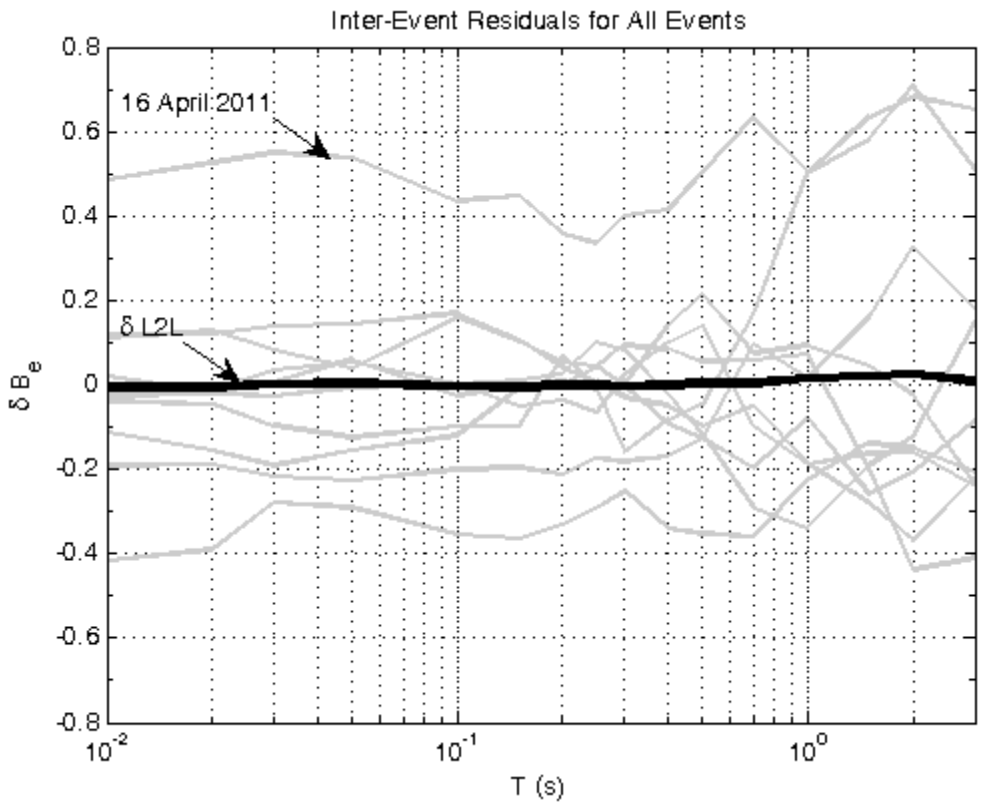

Figure 25: Inter-event residuals formulated using the adjusted NGA-West2 suite of GMPEs

Figure 26 illustrates the dependence of the inter-event residual on event magnitude. As was observed in Bradley 2015, the 16 April 2011 event ($M_W = 5.0$) has unusually high inter-event residuals, and the cause for this is unknown. It is possible that the estimated moment magnitude is incorrect or that the reported location for this event is imprecise. Further investigation of the cause of the anomalous characteristics of this event with regard to systematic effects in both the horizontal and vertical directions is required. Additionally, the inter-event residuals for the 19 October 2010 event increase sharply for vibration periods above one second. The cause of this anomaly is also unknown. In general, the inter-event residuals exhibit no dependence on M_W.

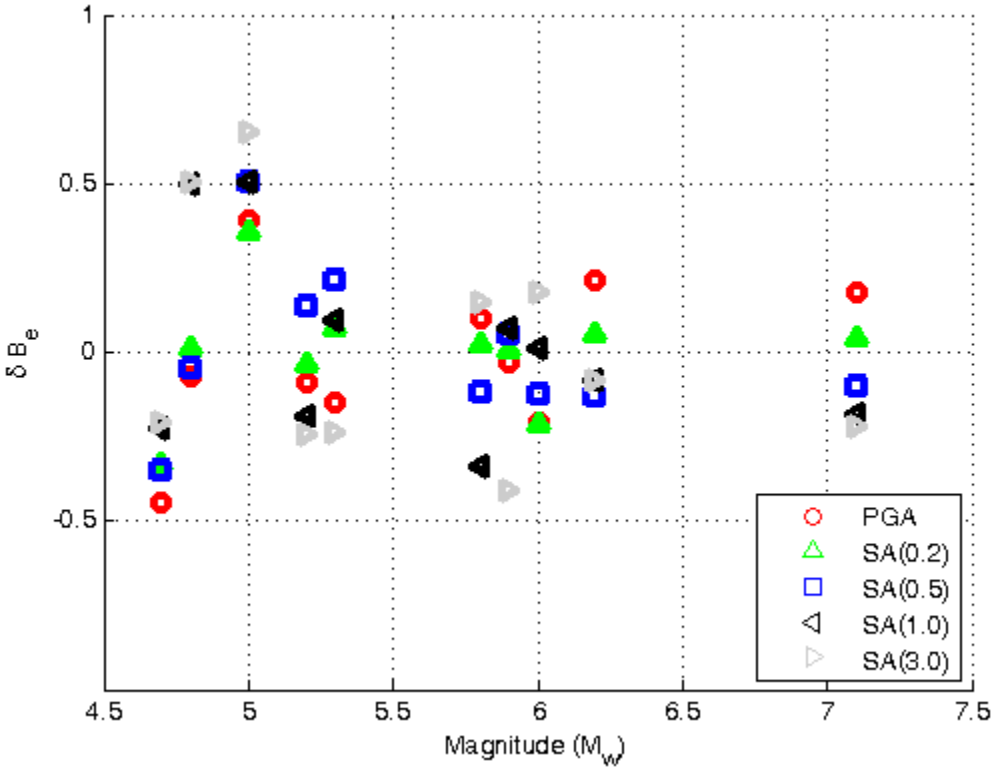

Figure 26: Inter-event residuals versus event magnitude for selected acceleration levels

6.2 Within-Event Residuals

Systematic site effects were identified by determining the within-event residuals at each site during all considered events. Appendix B includes the within-event residuals for all 25 strong motion stations considered plotted against vibration period. Due to space limitations, only a few illustrative examples are included here. Figure 27a-c show the within-event residuals at CBGS, HVSC, and KPOC. It can be seen in Figure 27a that motion at CBGS (Christchurch Botanical Gardens) was generally over-predicted by the NGA-West2 GMPE suite, except in the case of the 26 December 2010 event, which was greatly under-predicted, especially at low periods. Figure 27b and Figure 27c present the within-event residuals at HVSC (Heathcote Valley Primary School) and KPOC (Kaiapoi North School), respectively. It can be seen that the motion at HVSC is under-predicted at low periods and over-predicted at high periods. This behavior mirrors the trend observed in the horizontal motion within-event residuals at this station in Bradley 2015, which was attributed to known basin-edge effects in that area. The motion at KPOC is generally over-predicted, but this over-prediction is reduced in magnitude with increasing vibration period.

Where Figure 27a-c present the results for individual stations, including $\delta S2S$ for each station, Figure 27d shows $\delta S2S$ for all stations considered plotted together. On average, the values of $\delta S2S$ are close to zero. The largest deviations from zero tend to occur at very low periods, except in the case of the Port Hills stations, which indicate significant under-prediction of the vertical component of ground motion for periods of 0.2 to 1.0 seconds. Figure 27d demonstrates that the NGA-West2 suite of GMPEs is unbiased when using the ergodic assumption, although significant variability due to systematic site effects is evident, especially at low periods.

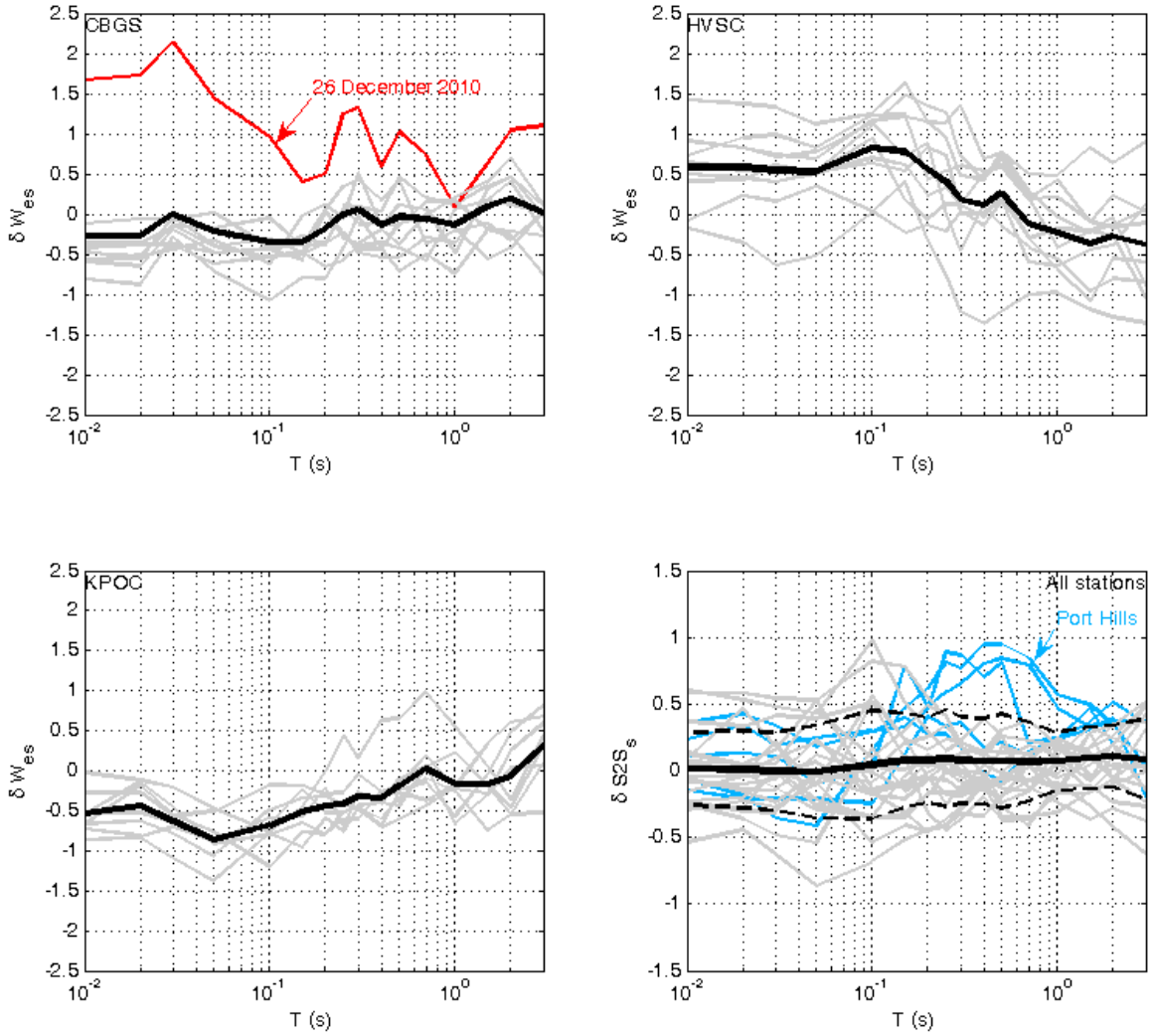

Figure 27: Within-event residuals for selected stations with systematic site-to-site residuals in bold; systematic site-to-site residuals for all stations with median, 16th and 84th percentile in bold

Figure 28 shows the within-event residuals for three stations near CBGS in the 26 December 2010 event. The values of the within-event residuals for CCCC and CHHC behave somewhat similarly. Although REHS behaves more similarly to CBGS than either CCCC or CHHC, REHS and CBGS are not extremely comparable. This is also evident in the peak ground acceleration values at these stations in the 26 December 2010 event. CCCC and CHHC had PGA values of 0.18g and 0.16g respectively, where REHS had a PGA of 0.26g and CBGS had a PGA of 0.44g. Of all of the records considered from this event,

these four experienced by far the largest accelerations. This suggests that there is some near-surface characteristic of CBGS that is having an influence on the ground motion recorded there.

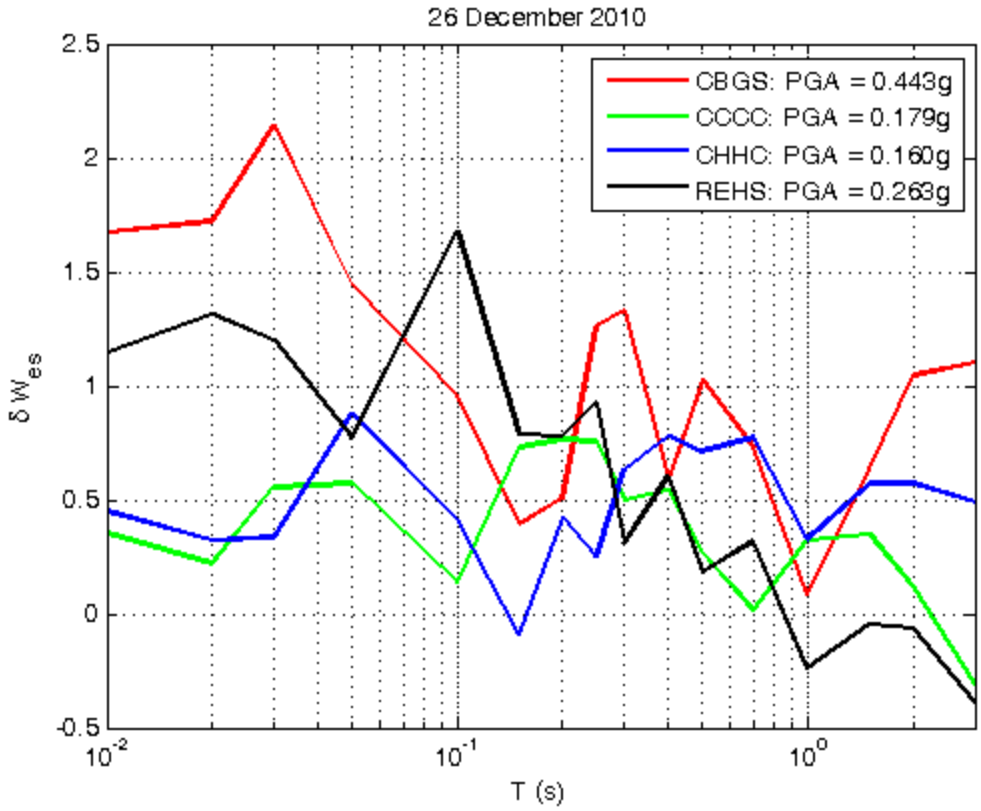

Figure 28: Within-event residuals for CBGS and nearby stations in the 26 December 2010 event

As was found in Bradley 2015 for the horizontal peak ground acceleration, no consistent relationship between vertical peak ground acceleration and the within-event residuals could be identified. Figure 29a-f provide illustrative examples. In some cases, such as CBGS and GODS, the record with the largest peak ground acceleration corresponds to the largest formulated within-event residuals. However, even in these cases, the remaining records do not follow in descending order. In most cases, represented here by CHHC, NNBS, PRPC and SMTC, no clear trend is present.

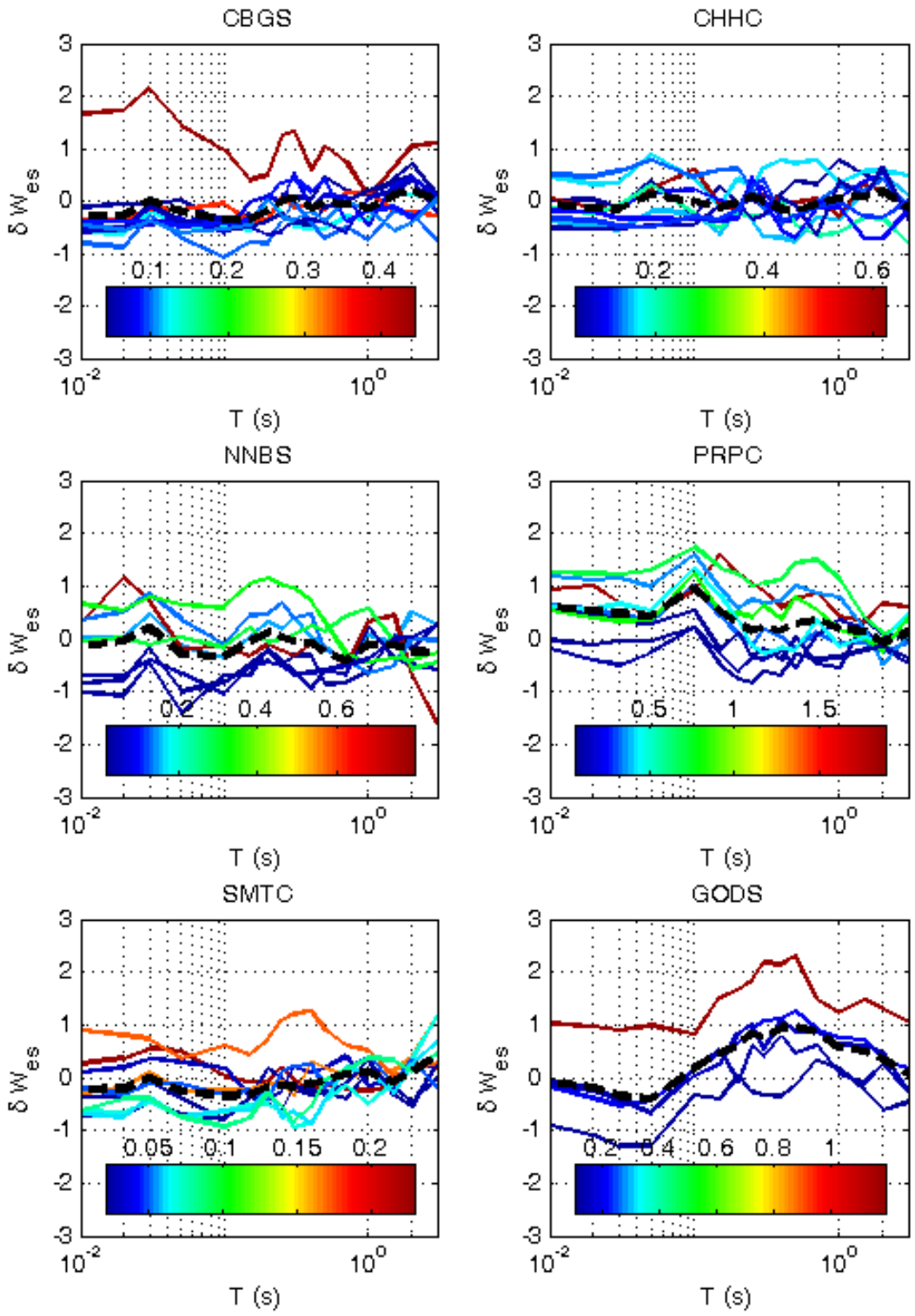

Figure 29: Within-event residuals for selected stations colored according to the PGA of the ground motion recordings taken there

The depth to water table was also considered in an attempt to determine whether effects such as those observed in the Kobe earthquake occurred. These effects were described in Yang and Sato (2000). Site

amplification of this nature is caused by a difference in the velocity of waves in saturated and unsaturated media, which results in an increase in the amplitude of waves in the upper, unsaturated layer. This analysis was impeded by the fact that many strong motion stations in the Canterbury region have similar depths to water table, and many stations with identical depths to water table experienced vastly different motion due to disparate inferred nonlinear soil behavior. In other cases, the effect of site amplification of this kind could not be isolated from the basin-edge effect or the effects of soil nonlinearity. No empirical conclusions regarding the relationship between water table depth and within-event residual have been drawn in this study.

6.3 Examination of Horizontal Motion at CBGS

Due to the unusual behavior of CBGS with regard to vertical motion, the horizontal motion at this station and three nearby stations (CCCC, CHHC, and REHS) was reexamined. The horizontal within-event residuals colored according to event PGA for these stations are shown in Figure 30. Again, no relationship between horizontal PGA and within-event residuals can be identified.

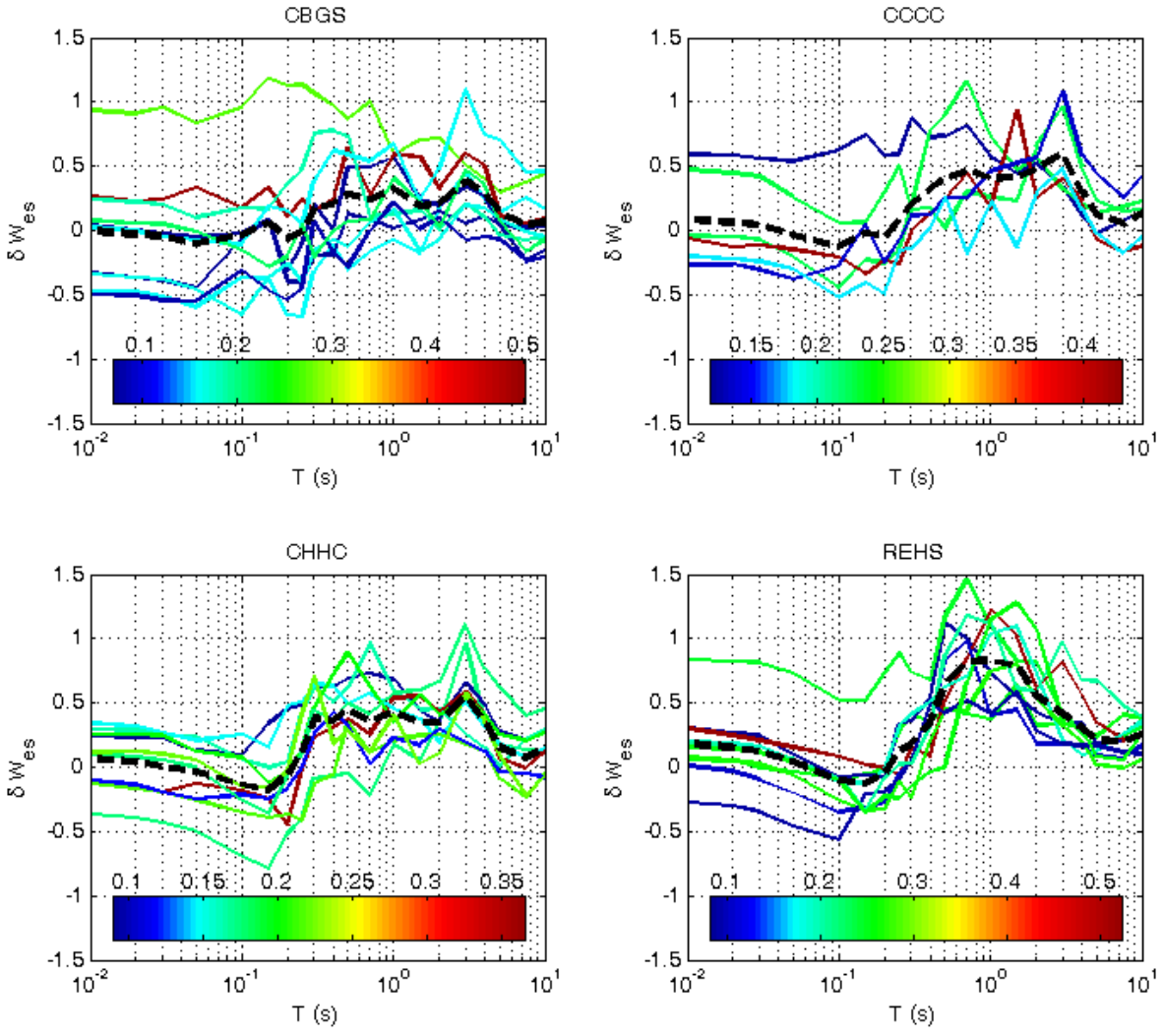

Figure 30: Within-event residuals for CBGS and nearby stations colored according to the PGA of the horizontal ground motion records taken there

Figure 31 shows the within-event residuals for horizontal motion at CBGS by itself. As was observed for vertical motion, an unusually high value of δW_{es} was observed at this station in the 26 December 2010 event for low periods. This provides further indication that the aberrance in the behavior at this station in this event was caused by near-surface effects at the CBGS site.

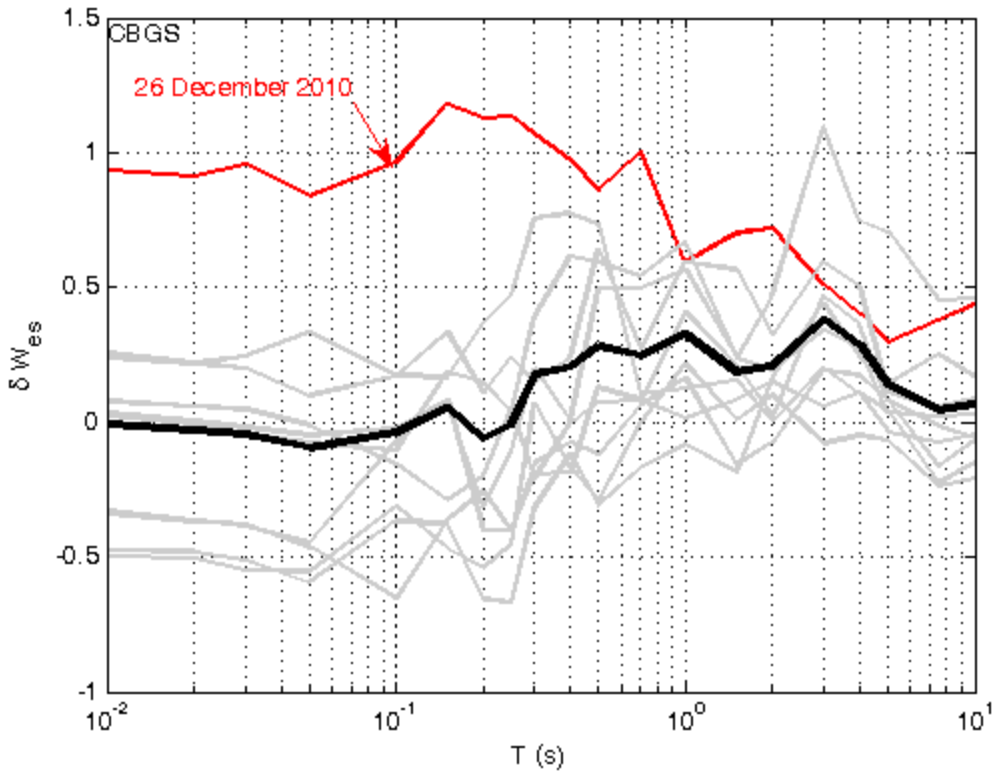

Figure 31: Within-event residuals for CBGS

7 Systematic Amplification in Sub-Regions in Canterbury

7.1 Systematic Site-to-Site Residuals for Sub-Regions in Canterbury

The recording stations being considered were split into five groups based on their geographical location and their systematic site-to-site residuals. These sub-regions were: the central business district, the western suburbs, the eastern suburbs, the northern suburbs, the southern suburbs, and the Port Hills area. A few stations did not fall neatly into a sub-region based on their geography and the systematic effects observed, and these were considered separately. The systematic site-to-site residuals of all stations in each sub-region are shown in Figure 32.

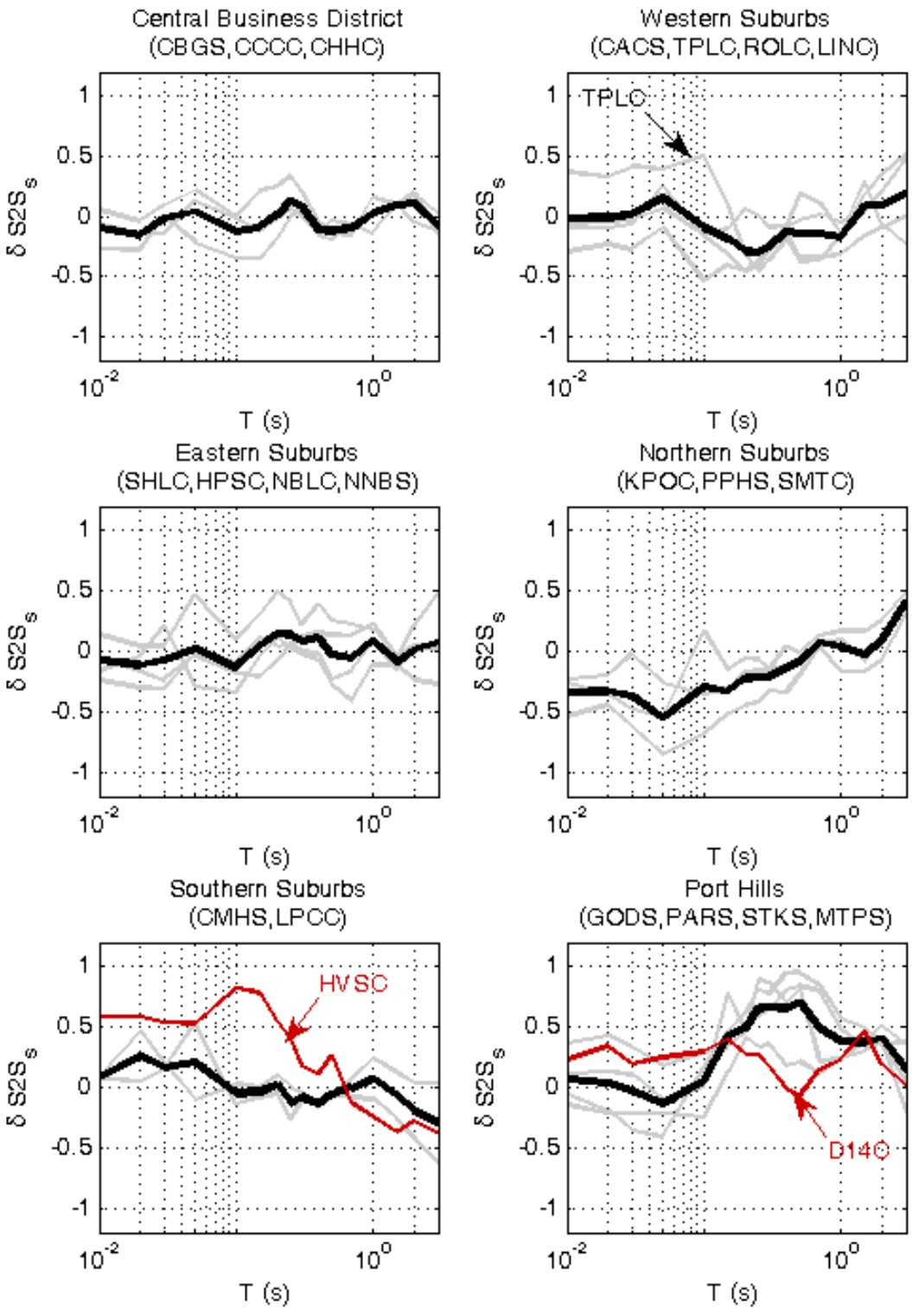

Figure 32: Systematic site-to-site residuals for the stations in each sub-regional grouping

Figure 32a shows the systematic site-to-site residuals for the three stations in the CBD sub-region: CBGS, CCCC, and CHHC. The same trend is shown by all three of these stations and their residuals do not deviate far from zero at any period.

Figure 32b illustrates the trends in the systematic site-to-site residuals for the stations in the Western Suburbs: CACS, TPLC, ROLC, and LINC. The systematic site-to-site residual for TPLC is significantly larger than the remaining stations for periods less than 0.2 seconds, but adheres to the sub-region trend at longer periods. In general, motion at the Western Suburbs stations was systematically over-predicted for periods between about 0.2 and 1.0 seconds and was otherwise predicted accurately.

Figure 32c shows the systematic site-to-site residuals for the four stations in the Eastern Suburbs: SHLC, HPSC, NBLC, and NNBS. The trends in $\delta S2S$ for this sub-region are generally similar to those of the CBD stations. It is interesting to note that NBLC, although resting on a sand dune, did not display aberrant behavior compared to its neighbors for vertical motion, as was observed in Bradley 2015 regarding horizontal motion.

Figure 32d illustrates the trends in $\delta S2S$ for the stations in the Northern Suburbs: KPOC, PPHS, and SMTC. These systematic site-to-site residuals for this sub-region are negative for low periods, indicating that motion there was generally over-predicted. They approach and pass zero for very long periods.

Figure 32e depicts the systematic site-to-site residuals for the Southern Suburbs: CMHS and LPCC. For both of these stations, $\delta S2S$ is slightly positive for periods below 0.1 seconds and hovers around zero before becoming negative at around 1 second. Also included is the $\delta S2S$ for the HVSC station, shown in red. HVSC was excluded from the Southern Suburbs sub-regional grouping in this study due to the discrepancy between its systematic residuals and those of its neighboring stations. It is therefore not used when calculating the mean for this sub-region in this figure.

Figure 32f shows the systematic site-to-site residuals for the stations in the Port Hills sub-region: GODS, PARS, STKS, and MTPS. It should be noted that GODS, PARS, and MTPS are very close together and exhibit extremely similar trends in their $\delta S2S$. STKS exhibits a similar trend, although with a smaller plateau between vibration periods of 0.1 and 3 seconds. D14C, shown in red but not used when calculating the sub-regional mean, is excluded because it does not follow the same trend of having near-zero values of $\delta S2S$ for low vibration periods with a plateau at longer periods, but rather has a high $\delta S2S$ for the entire range of periods considered. It is also further away than STKS from the core group formed by GODS, PARS, and MTPS.

7.2 Locations Which Do Not Conform to Sub-Regional Categories

It is worth noting that REHS and RHSC, while geographically grouped with the stations in the CBD sub-region, have similar within-event residuals that exhibit a different trend than the remaining CBD stations, as shown in Figure 33.

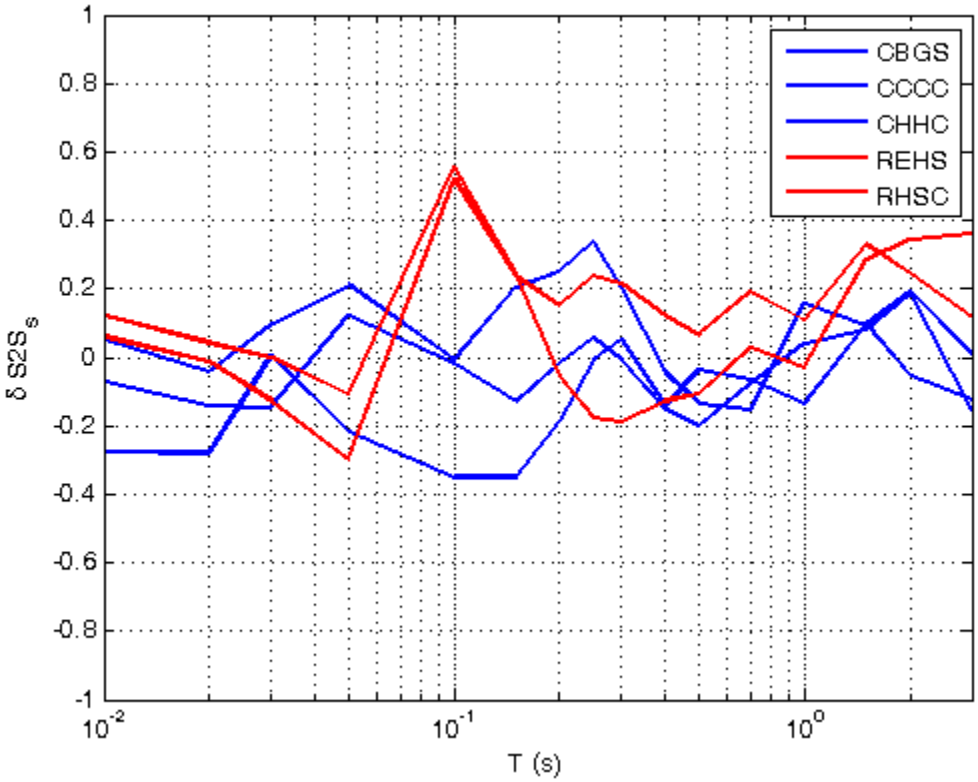

Figure 33: Systematic site-to-site residuals for stations near the Christchurch CBD

It can be seen that REHS and RHSC are systematically under-predicted at vibration periods around 0.1 seconds. Both of these stations also had pronounced horizontal residuals at low periods (Bradley 2015). Additionally, their within-event residuals are generally higher than those of the other CBD stations at very low and very high periods. It is possible that this is due to the large impedance contrast (stiff deposits overlaid with soft deposits) in the soil strata at these locations.

HVSC, PRPC, and D14C were also not assigned to a sub-region. HVSC and PRPC were observed to exhibit similar trends, as shown in Figure 34. However, PRPC is located near to the CBD stations and HVSC is located near the Port Hills stations. Neither station exhibits the same trend as its corresponding geographical cluster, so neither was assigned. D14C and STKS are located away from the cluster formed by GODS, PARS, and MTPS, which may explain the difference in their behavior from the other Port Hills stations. It is possible that the basin-edge effects clearly observed at these stations were more significant in the area where GODS, PARS, and MTPS are located.

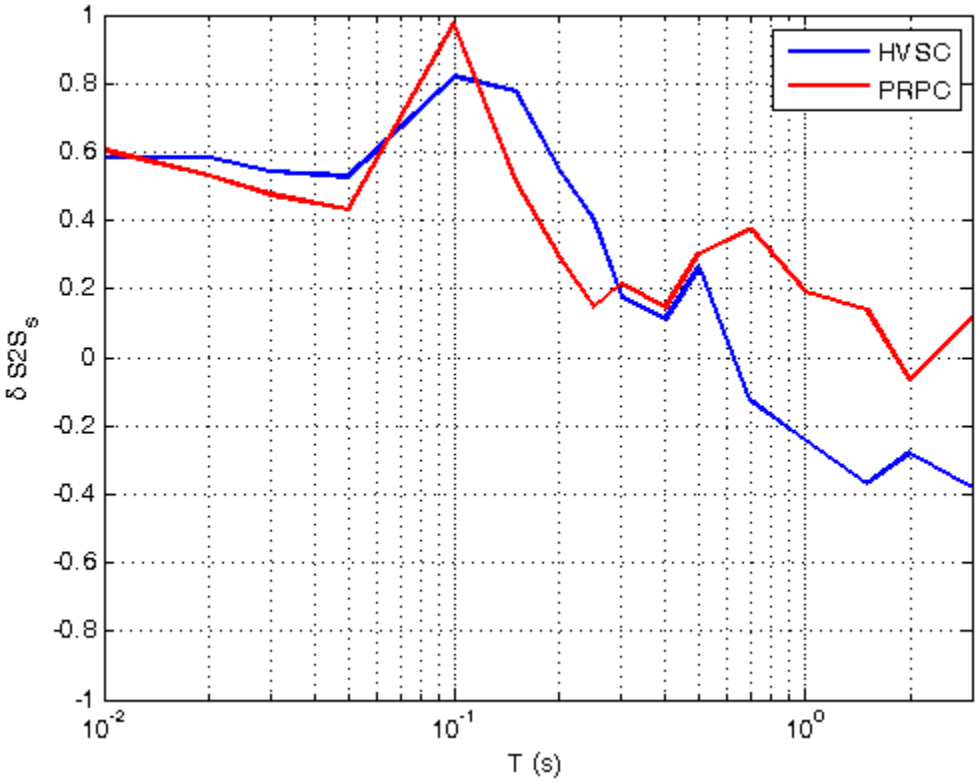

Figure 34: Systematic site-to-site residuals for HVSC and PRPC

Because HVSC is situated on the edge of the basin and PRPC is located away from the basin edge, the results shown in Figure 34 suggest a complicated subsurface topography. This could be due to the trampoline effect (Aoi, Kunugi, and Fujiwara 2008). The trampoline effect is caused by separation of surficial soil layers, which limits the magnitude of negative vertical acceleration to -1g and therefore causes asymmetry in vertical motion records. This effect has been identified in the vertical records at both of these locations in a study of ground motions from the 22 February 2011 event (Bradley and Cubrinovski 2011). Whether this effect contributes to the site behavior at HVSC and PRPC in other events is unknown. Further study into the systematic site effects at these locations is needed.

7.3 Comparison of All Sub-Regions

Figure 35 shows the variation in the average site-to-site residuals of each sub-region with vibration period. Because the number of sub-regions and the number of unassigned locations are so great, the unassigned locations have been omitted from this plot to reduce clutter. The Northern Suburbs sub-region has a negative systematic site-to-site residual at periods less than 0.1 seconds. For the same range of periods, the Southern Suburbs have a positive value of $\delta S2S$. All other sub-regions have systematic site-to-site residuals of near zero at these low periods.

For periods larger than 0.1 seconds, the CBD, Eastern Suburbs, and Eastern Suburbs maintain values of $\delta S2S$ around zero. The Northern Suburbs sub-region's systematic site-to-site residual grows steadily and is slightly positive at high periods. That of the Western Suburbs sub-region becomes slightly negative for periods up to around 1.0 seconds before returning to near zero. The Port Hills sub-region's average site-to-site residual increases sharply around 0.1 seconds and plateaus until nearly 3.0 seconds before

dropping again. This under-prediction at this range of periods is reflective of basin-edge effects experienced in this sub-region.

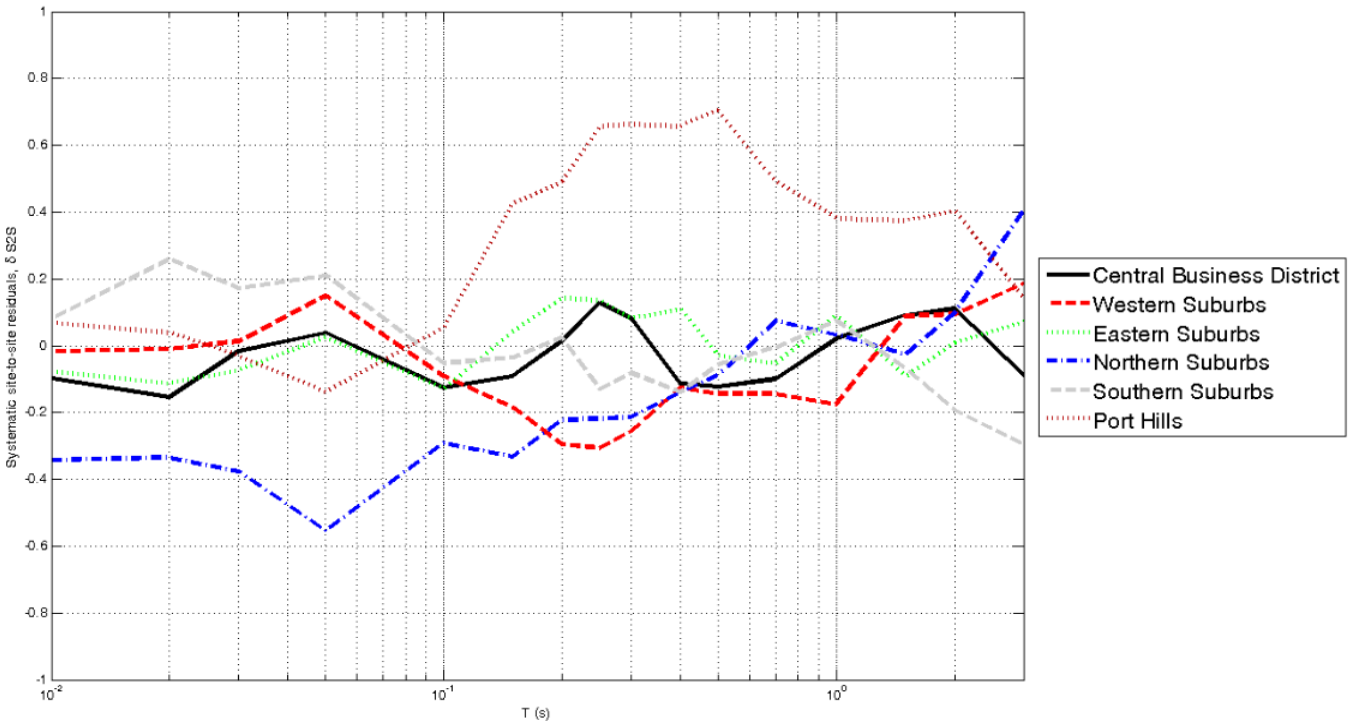

Figure 35: Average systematic site-to-site residuals for stations in each sub-regional grouping

Figure 36 shows the systematic amplification factor plotted against vibration period for each of the six sub-regions. This factor would be applied to the predicted median ground motion in these regions. This factor follows the same trends as the systematic site-to-site residual above. For the periods considered, only the Port Hills sub-region exceeds a factor of 1.5. The lowest observed factor was in the Northern Suburbs sub-region at periods of 0.2 seconds or less.

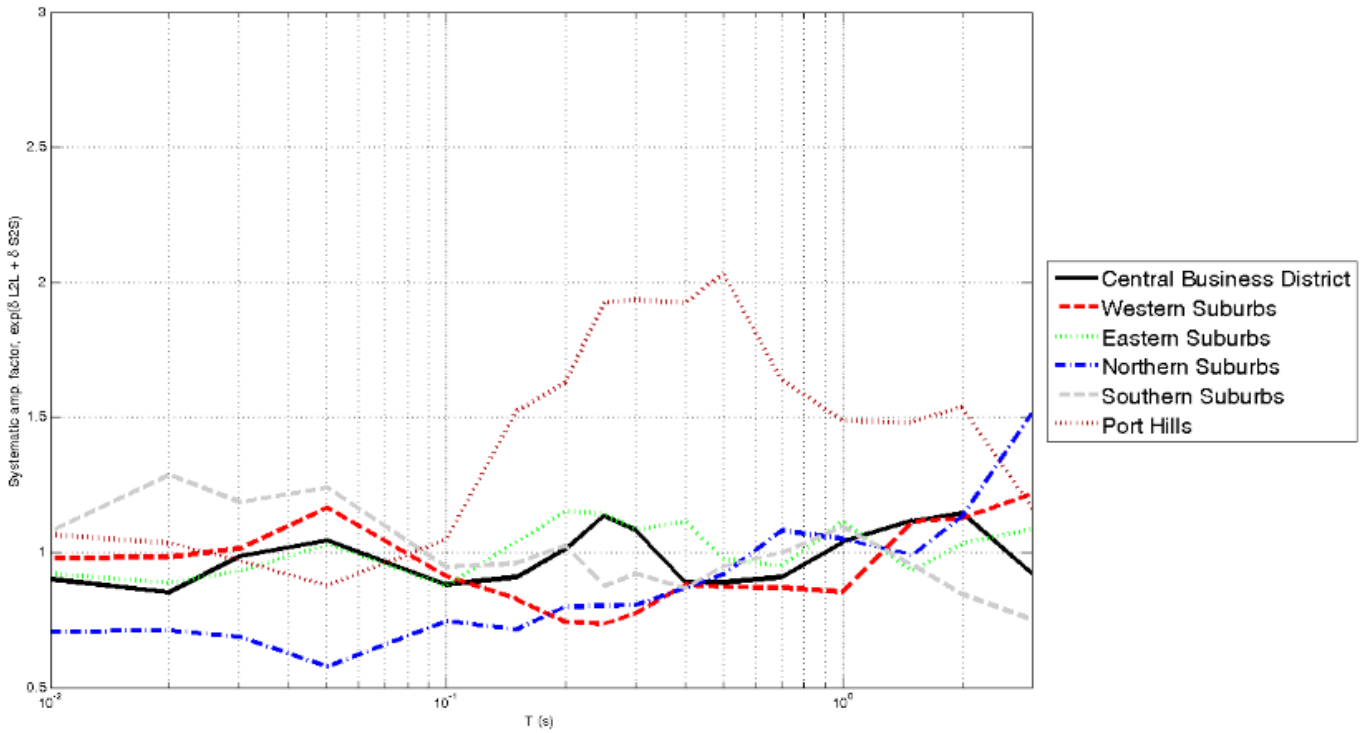

Figure 36: Average systematic amplification factors for stations in each sub-regional grouping

Figure 37 shows the amplification factors that were calculated for each individual station in order to illustrate the variability within each sub-region. For the CBD, the Southern Suburbs, and the Northern Suburbs, within-region deviation away from the mean is very low. It is slightly higher for the Western Suburbs and Eastern Suburbs, and significantly higher for the Port Hills. Except for the Northern Suburbs and Port Hills, all sub-regions behave very similarly. The variation between the means of each sub-region is small compared to the variation among sites in one sub-region.

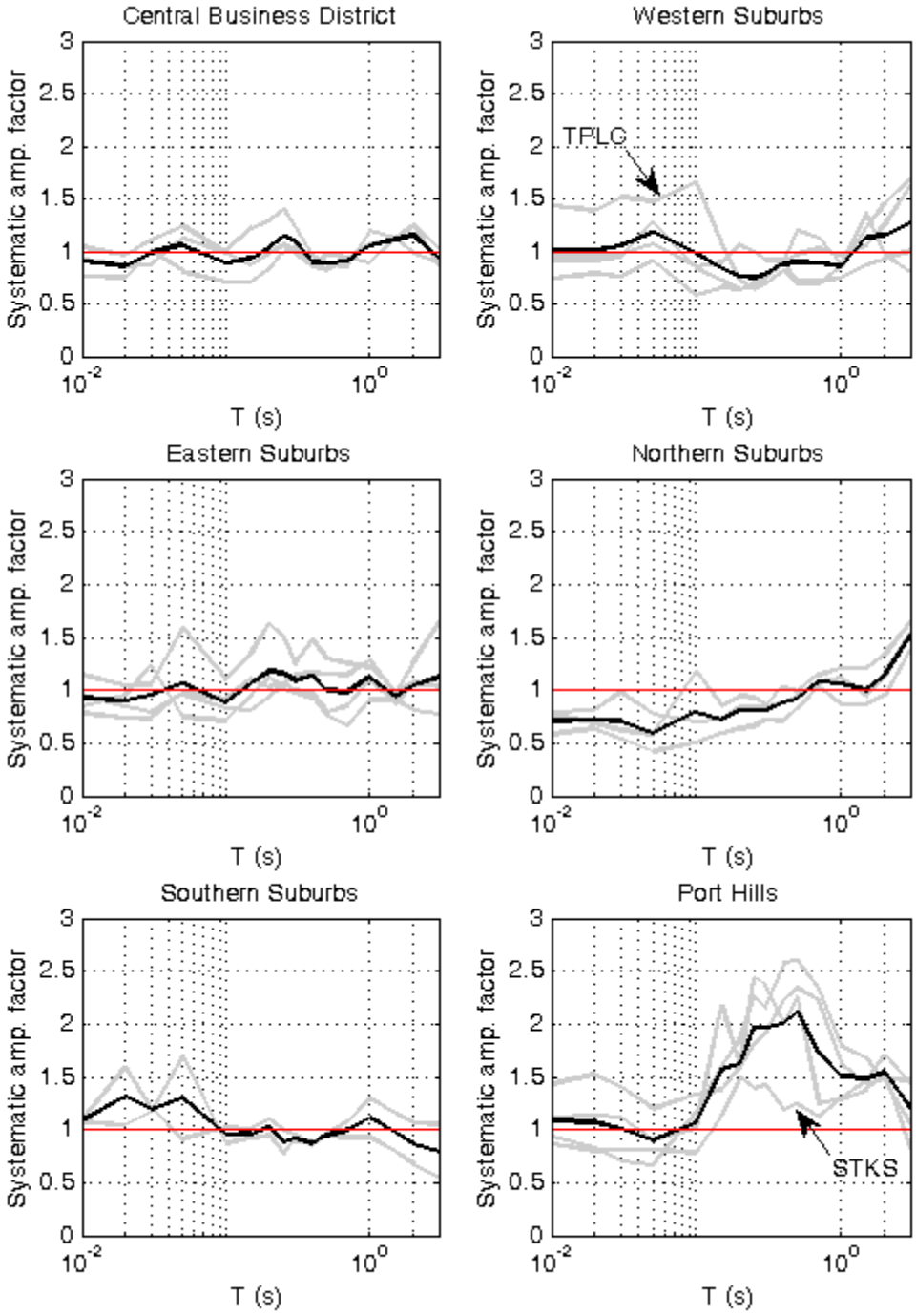

Figure 37: Systematic amplification factor for stations in each sub-regional grouping

The systematic amplification factors for all stations as functions of vibration period are shown in Figure 38. Those of the Port Hills sub-region are colored in blue. The Port Hills stations have extremely large systematic amplification factors for large periods, greatly exceeding the 84th percentile. KPOC, which was

included in the Northern Suburbs sub-region, is colored in red and is noteworthy for having the lowest overall amplification factor with a value around 0.5 for low periods. Neither HVSC, in green, nor PRPC, in purple, were assigned to sub-regions, and exhibit the largest factors seen at low periods, which are similar in magnitude to the amplification seen in the Port Hills stations at longer periods. Values of the amplification factor for most stations at most periods do not fall outside the band formed by the 16th and 84th percentiles.

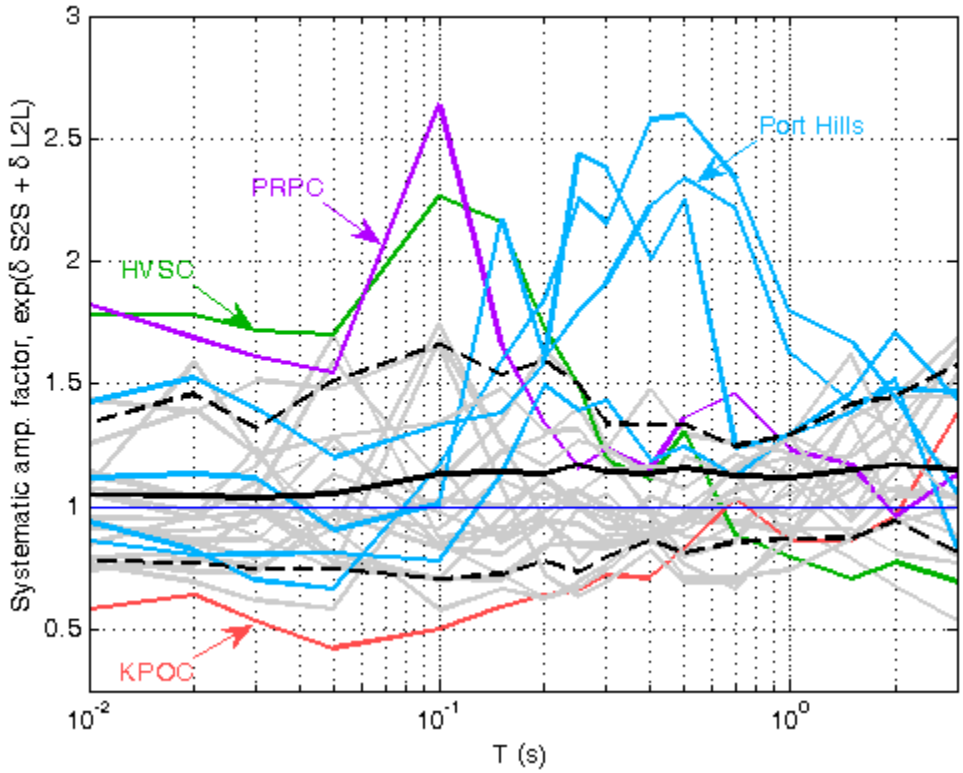

Figure 38: Systematic amplification factors for all stations

7.4 Further Investigation of the Northern Suburbs Stations

Because the Northern Suburbs stations are located furthest from the basin, further investigation of the systematic over-prediction for these stations was undertaken. The adjusted and unadjusted total residuals at $T = 0.01s$ for these stations are plotted against distance-to-rupture in Figure 39. The unadjusted residuals of the stations in the Northern Suburbs follow the same trend as the residuals of other sub-regions, and they do not appear to suffer from overcorrection when the R_{rup} bias adjustment is applied.

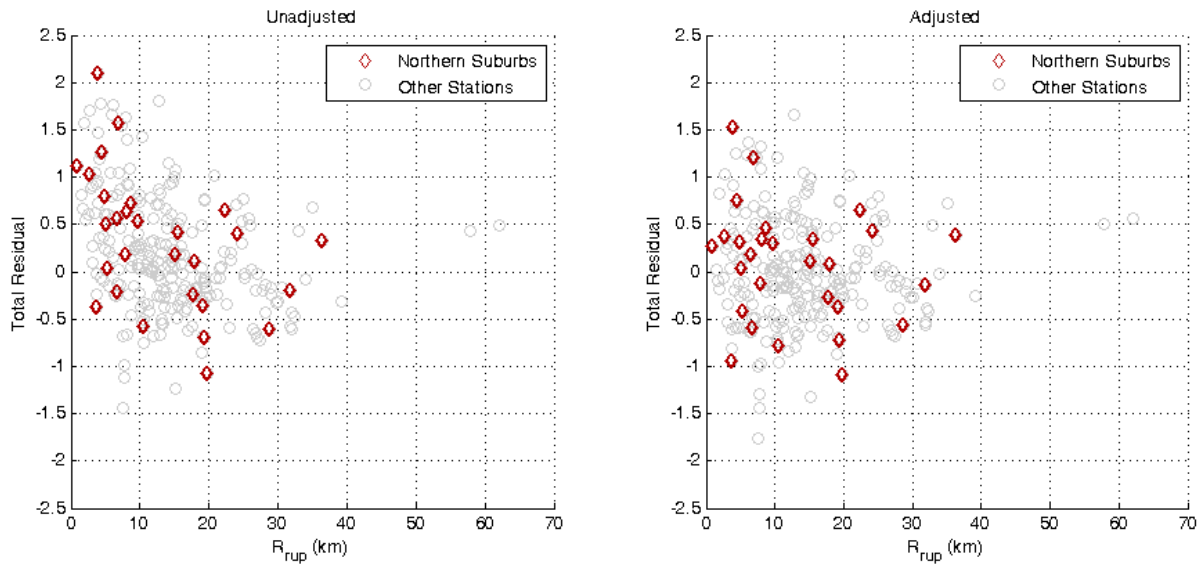

Figure 39: Total residuals versus distance-to-rupture for both the adjusted and unadjusted NGA-West2 GMPEs with Northern Suburbs stations highlighted

The within-event component of the residuals at the Northern Suburbs stations in each event is plotted against vibration period in Figure 40a-c. Figure 40d illustrates the relationship between the systematic site-to-site residuals of the Northern Suburbs stations and their average distance-to-rupture across all events. It can be seen in Figure 40d that there is a positive relationship between $\delta S2S$ and mean R_{rup}. However, R_{rup} does not seem to have a consistent influence on the within-event residuals.

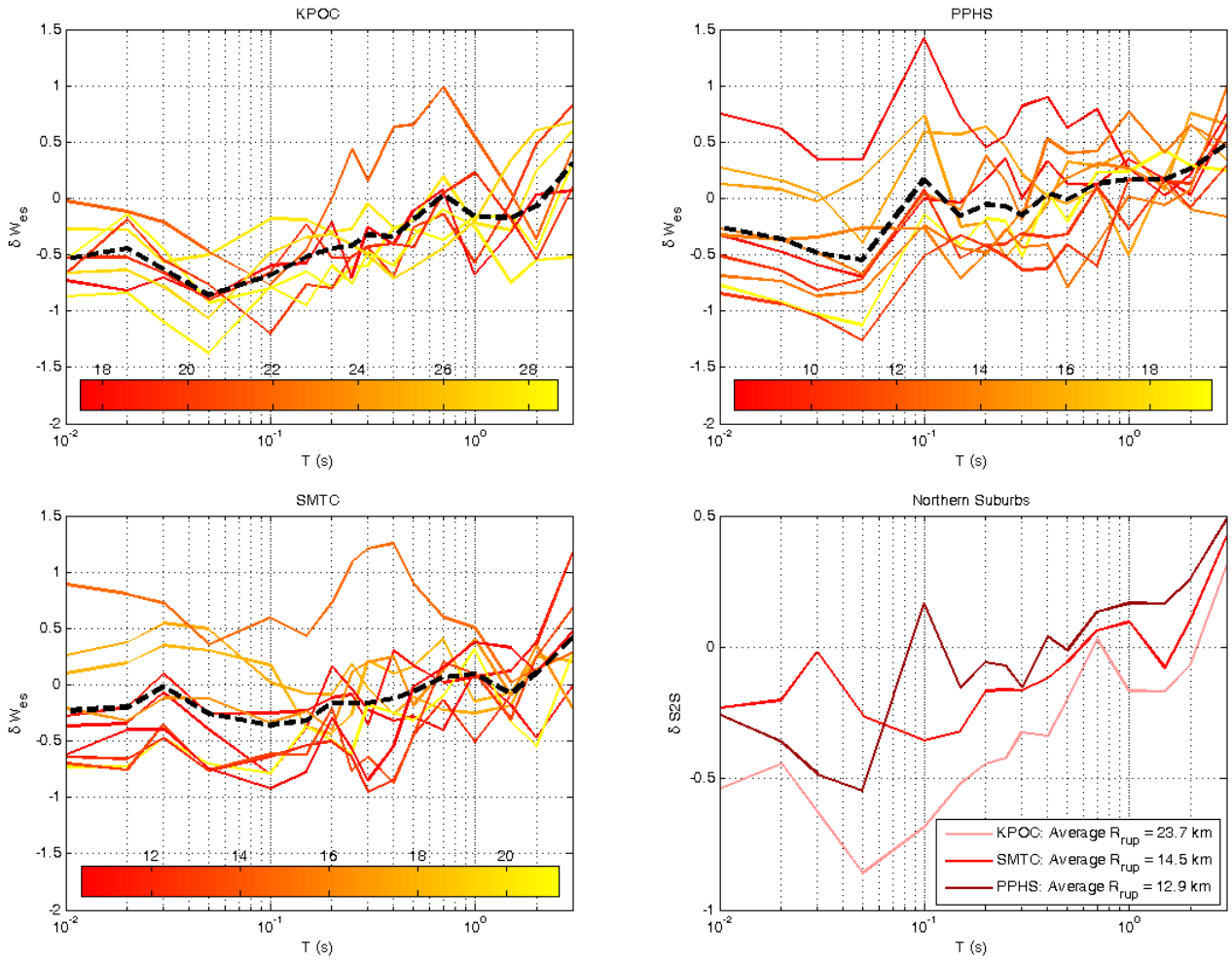

Figure 40: Within-event residuals and systematic site-to-site residuals for the Northern Suburbs stations colored according to their distance-to-rupture in each event for the adjusted NGA-West2 GMPEs

To show that this pattern is not caused by the distance-to-rupture bias adjustment, the same plots for the unadjusted records are illustrated in Figure 41. Because the empirical adjustment is relatively flat for the distances to rupture for these stations, little change can be seen in the shape of each individual event-station pair's within-event residual curve. However, the adjustment generally shifted each curve up slightly. This indicates that the under-prediction in the Northern Suburbs stations was more severe before the R_{rup} bias adjustment was applied.

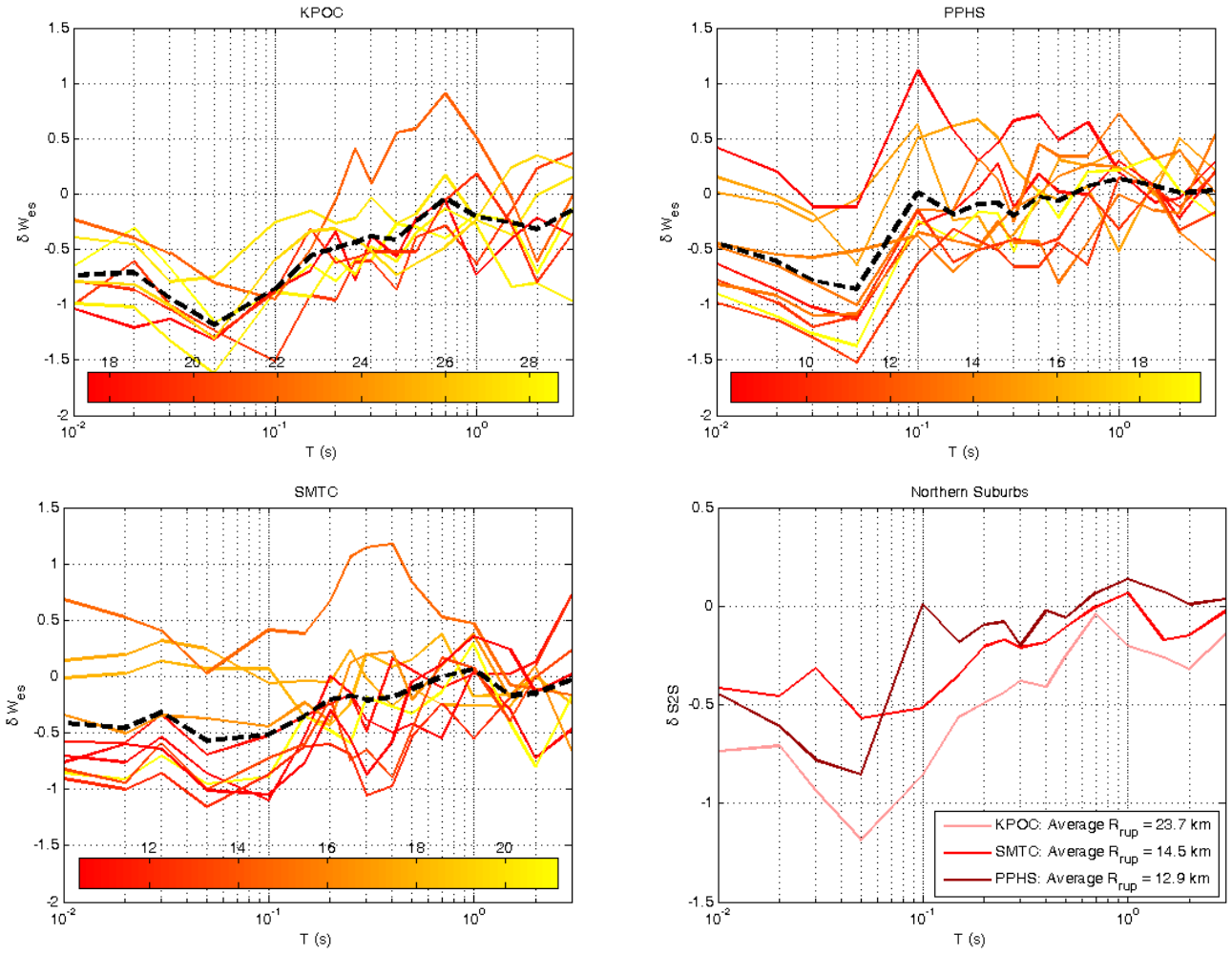

Figure 41: Within-event residuals and systematic site-to-site residuals for the Northern Suburbs stations colored according to their distance-to-rupture in each event for the unadjusted NGA-West2 GMPEs

Figure 42 shows the empirical distance-to-rupture bias adjustment factor applied for each record from the Northern Suburbs plotted as a function of vibration period. The adjustment factors corresponding to the mean R_{rup} and the mean R_{rup} plus or minus one standard deviation are also shown. The range of the factors applied to the Northern Suburbs stations is shaded. There is no trend to suggest that one station is affected by the adjustment disproportionately strongly compared to the other two. In all cases, the adjustment has a larger effect at low periods. For many of the Northern Suburbs records, the adjustment is relatively small for all periods considered.

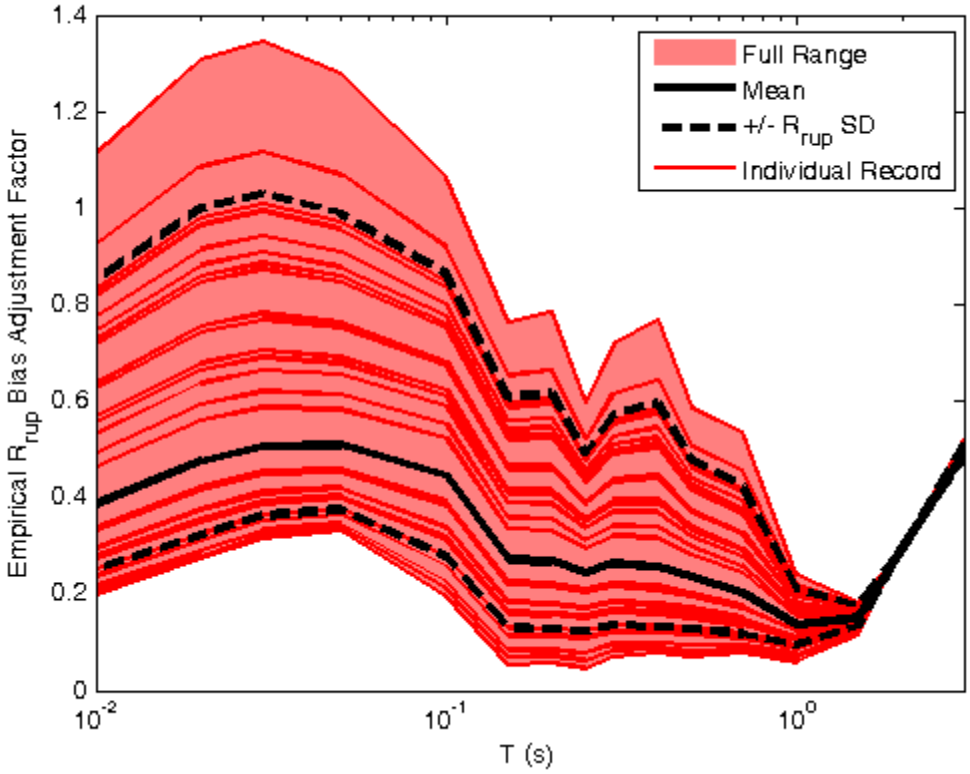

Figure 42: Empirical distance-to-rupture adjustment factor for all Northern Suburbs stations in all events

The trends observed in the systematic site-to-site residuals of the Northern Suburbs stations therefore do not appear to be a result of the empirical distance-to-rupture adjustment factor. A more likely cause of this phenomenon is the fact that the Northern Suburbs stations are located a significant distance away from the basin's edge, where high-frequency shaking is dominant. The basin edge generates Rayleigh waves, which decrease in amplitude as they travel north towards these stations. The amplitude of short-period motion at these stations is smaller due to the reduced influence of these basin-generated waves.

8 Non-Ergodic Standard Deviations

8.1 Between-Event Standard Deviations

Figure 43 presents the ergodic prediction of the between-event standard deviation, τ, yielded by the corrected suite of NGA-West2 GMPEs, in comparison with the non-ergodic estimate and its constituent components: the standard deviation of the systematic location-to-location residuals, τ_{L2L_l}, and that of the remaining between-event residuals, τ_0. As observed in Bradley 2015, τ_{L2L_l} is axiomatically smaller than τ_0 by a factor of $\sqrt{10}$ ($\sqrt{N_{Events}}$). The non-ergodic between-event standard deviation is uniformly smaller than the ergodic estimate. For periods up to around 0.25 seconds, the reduction factor in τ, RF_τ, is roughly 60%. Between 0.25 and 2 seconds, it increases to roughly 90%.

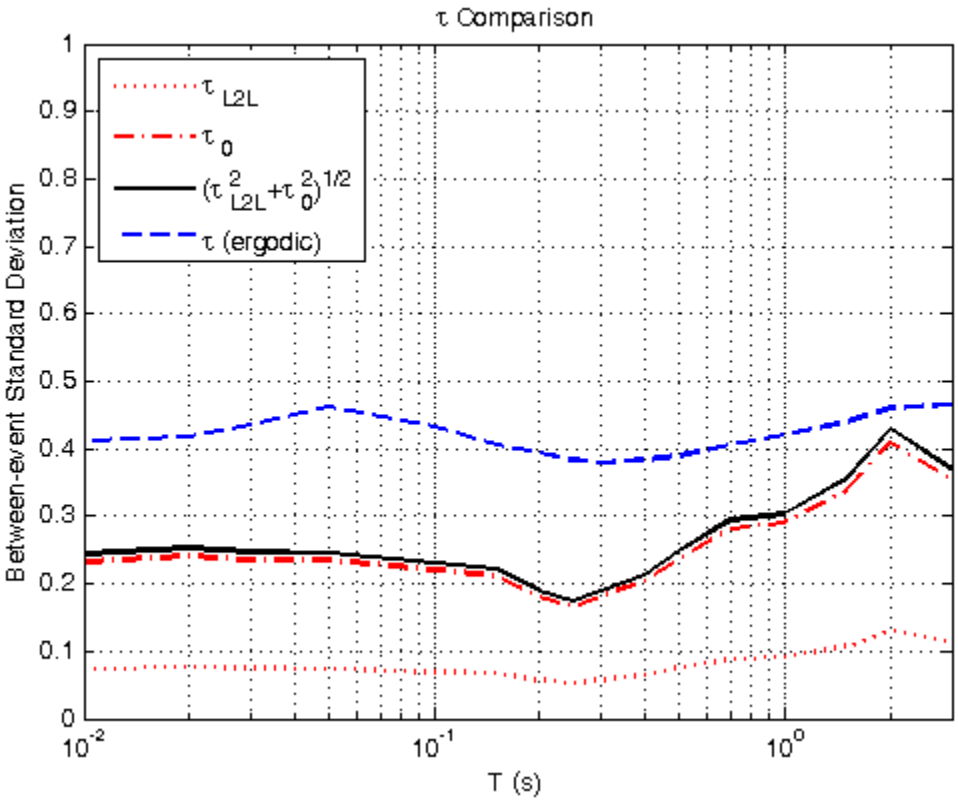

Figure 43: Ergodic and non-ergodic between-event standard deviation

Similar to the results presented in Bradley 2015, the average value of the ergodic between-event standard deviation across all 10 events is shown here. The reduction factor in the between-event standard deviation, RF_{τ}, for each event is shown in Figure 44.

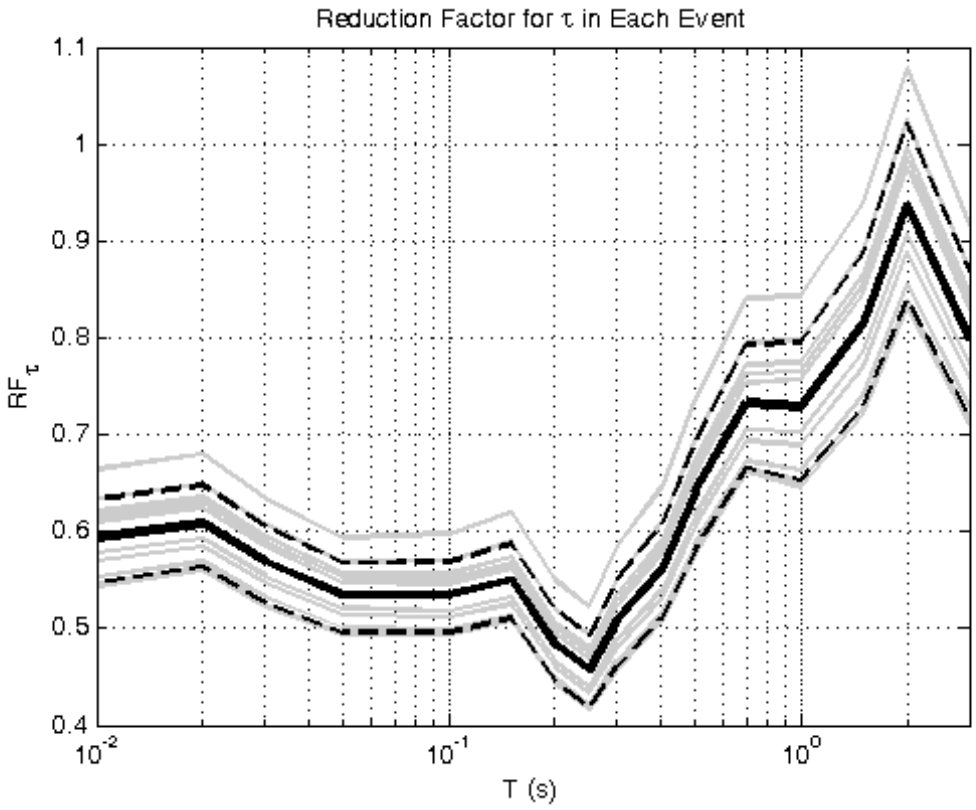

Figure 44: Reduction factor in between-event standard deviation for all 10 events

The nonergodic between-event variance ($\tau_{nonergodic}{}^2$) is roughly 30% of the ergodic between-event variance ($\tau_{ergodic}{}^2$) for periods up to 0.3 seconds. In the Bradley 2015 study of systematic source and site effects on the horizontal motion recorded in the Canterbury earthquake sequence, $\tau_{nonergodic}{}^2$ was roughly 55% of $\tau_{ergodic}{}^2$. The reduction in between-event uncertainty resulting from easing the ergodic assumption is much greater for vertical motion than for horizontal motion at low periods. At periods approaching 3 seconds, the reduction becomes more similar. The ratio of the nonergodic between-event variance to the ergodic between-event variance for both vertical and horizontal motion is presented in Figure 45.

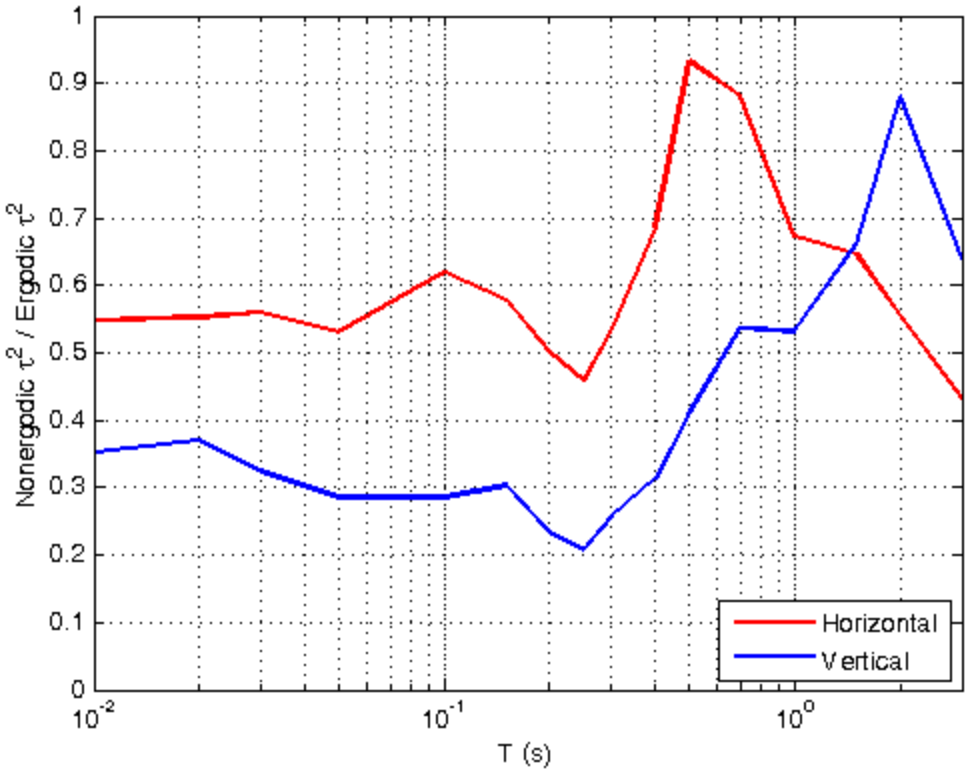

Figure 45: Comparison of the ratio between non-ergodic and ergodic variance for both horizontal and vertical motion

8.2 Within-Event Standard Deviations

Plots of the ergodic and non-ergodic within-event standard deviations for each station in the same style as Figure 43 are presented in Appendix C. To illustrate the high amount of variability in these plots, the within-event standard deviations of six selected stations (CBGS, HVSC, NBLC, SHLC, TPLC, and GODS) are shown in Figure 46.

The low-period residuals of CBGS are heavily influenced by the 22 February 2011 event, in which a remarkably large amount of liquefaction was observed in the area. The fact that its values of δW_{es} are much higher for that event than for other events at low periods is reflected in its high non-ergodic ϕ for the same periods. HVSC has very large values of δW_{es} for low periods, but they are uniformly high and its non-ergodic ϕ is roughly equivalent to the ergodic result. NBLC lies on a sand dune, and this may have some influence on the magnitude of its non-ergodic intra-event standard deviations. As previously mentioned, GODS is in the Port Hills region and basin-edge effects are a likely driver of its high intra-event standard deviation because these effects might affect the site somewhat differently in each separate event. For some stations, such as SHLC and TPLC, the non-ergodic within-event standard deviation is smaller than the ergodic value for all periods.

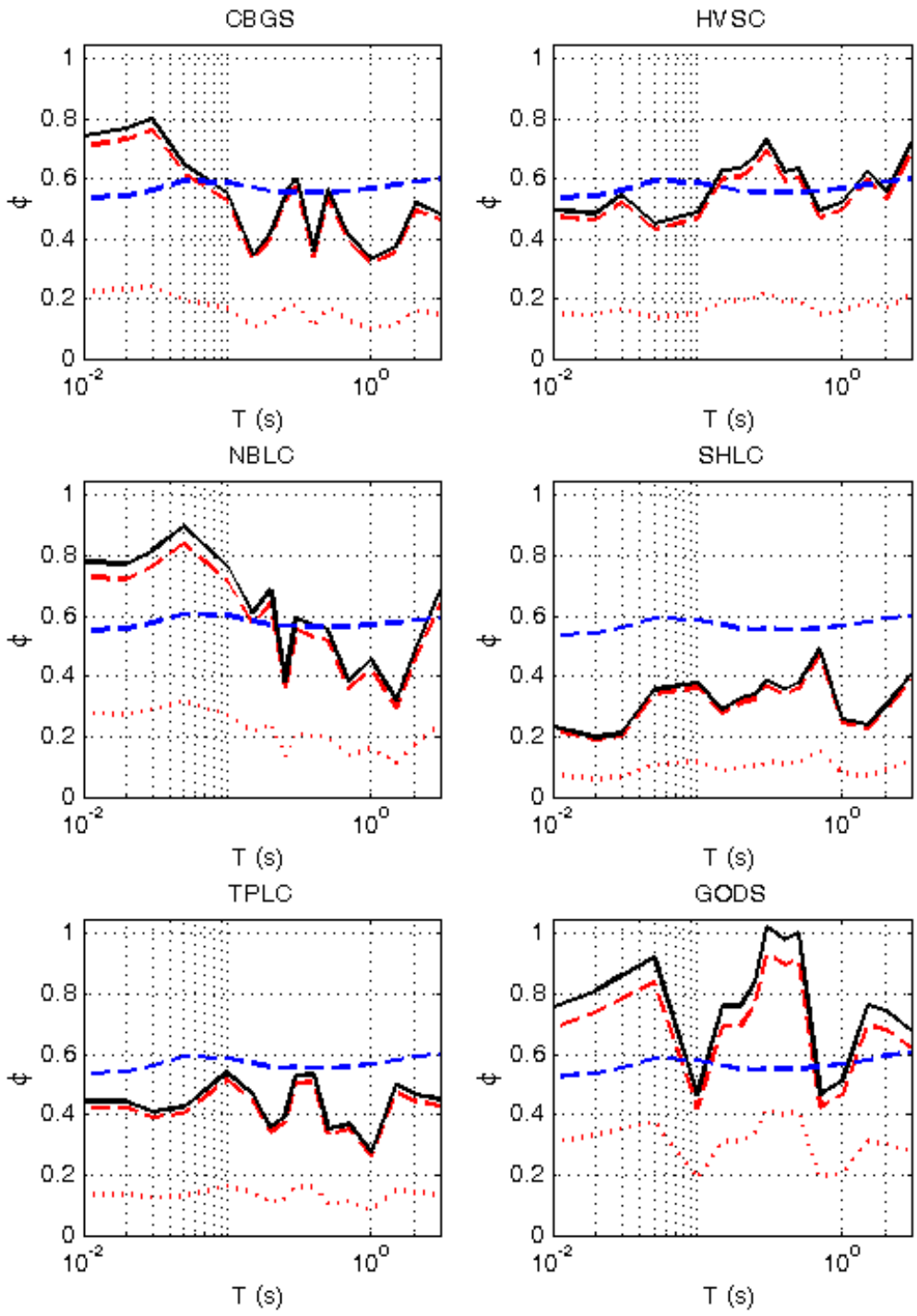

Figure 46: Ergodic and non-ergodic within-event standard deviation for selected stations

In many cases, the non-ergodic within-event standard deviations exceed the ergodic value produced by the corrected suite of NGA-West2 GMPEs by significant amounts. The reduction factor in the within-event standard deviation, RF_{ϕ}, for all stations including the Port Hills stations is shown in Figure 47. The same plot excluding the Port Hills stations follows in Figure 48. RF_{ϕ} for the Port Hills stations shows no cohesive trend except for a tendency to spike during the range of periods for which motion at those sites

was systematically under-predicted. For the rest of the stations considered, RF_ϕ tends to have the most scatter at low vibration periods while falling mostly within the 16th to 84th percentile band at longer periods. Although the median value of RF_ϕ falls below 1 for all periods, there are a significant amount of stations that exhibit values greatly above or below 1 at some periods.

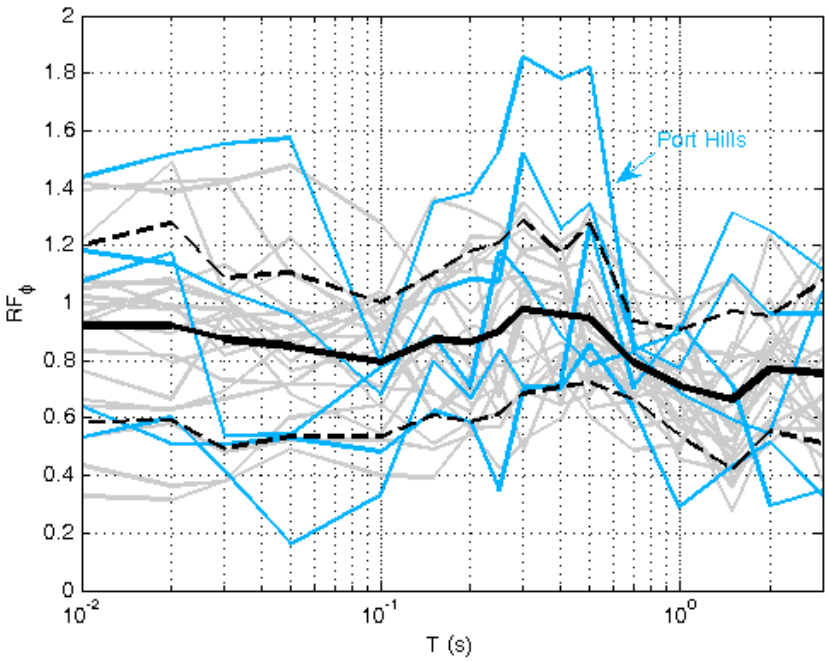

Figure 47: Reduction factor in within-event standard deviation for all stations

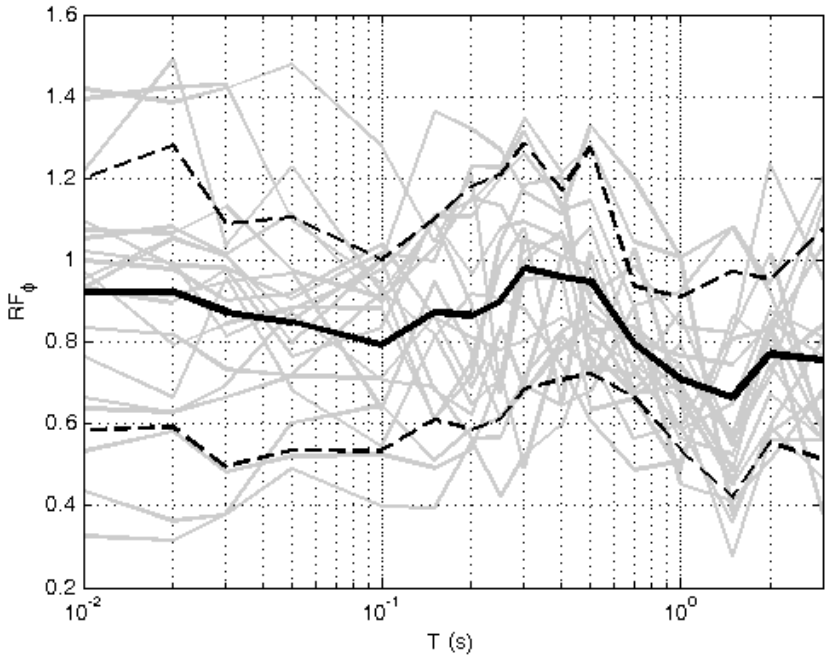

Figure 48: Reduction factor in within-event standard deviation excluding the Port Hills stations

In almost all cases, the within-event standard deviation greatly exceeds the between-event standard deviation. This indicates that site-to-site variability is more significant than location-to-location variability, and that the within-event standard deviation is the dominant contributor to the total standard deviation. This dominance is more pronounced for vertical motion than for horizontal motion.

8.3 Total Standard Deviation

The reduction factor on the total standard deviation, RF_σ, for all stations is included in Figure 49. As was the case in Bradley 2015, RF_σ behaves very similarly to RF_ϕ. At low periods, where the reduction factor in the between-event standard deviation is the lowest, values of RF_σ are less dispersed than were the values of RF_ϕ. At longer periods, this effect is less pronounced, except at exactly $T = 2s$, where RF_τ reaches a peak.

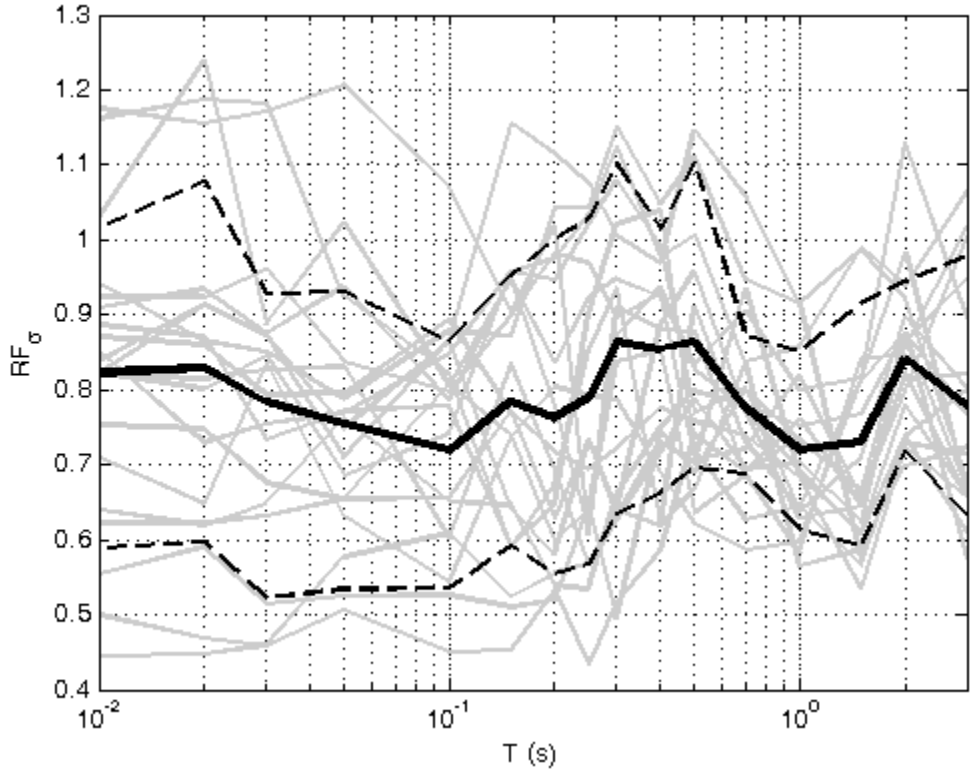

Figure 49: Reduction factor in the total standard deviation for all except the Port Hills stations

9 Conclusions

This study examined vertical ground motion observations at a collection of recording stations located near the sources of ten earthquakes in the 2010-2011 Canterbury earthquake sequence. The objective of the study was to evaluate the performance of the suite of Next Generation Attenuation vertical ground motion prediction equations when applied to Canterbury region, to identify and correct bias in these equations, and to develop modification factors to allow for easing the ergodic assumption. Bias was identified in ground motion predictions of the NGA-West2 GMPE with respect to distance to rupture and an empirical adjustment was developed and implemented. The location-to-location residuals, which account for the systematic portion of the between-event residuals, were found to be near zero for all periods considered (up to 3 seconds). As in Bradley 2015, the systematic site-to-site residuals were found to be independent of vertical ground motion intensity.

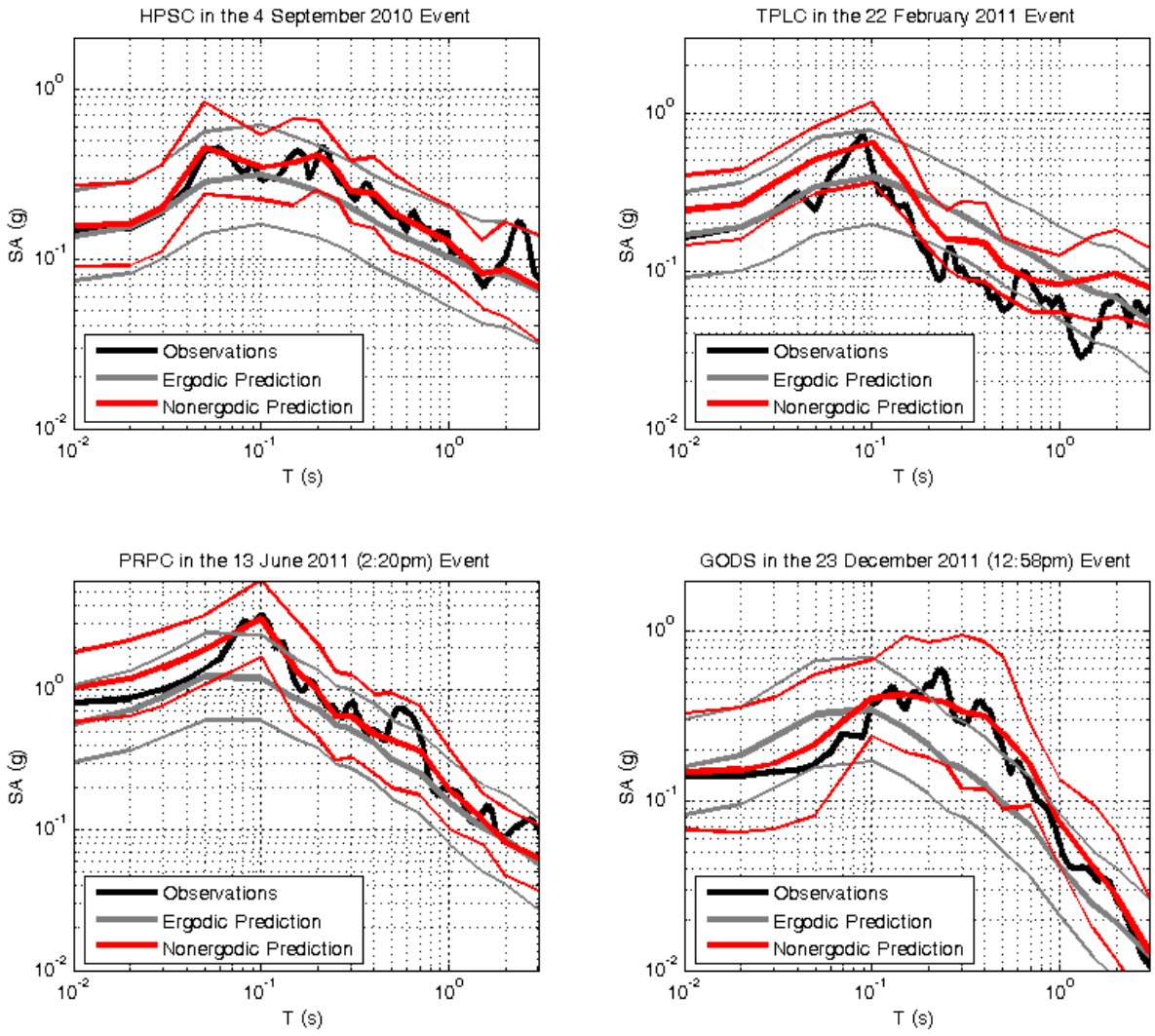

Figure 50: Comparison of results before and after easing the ergodic assumption for selected stations in selected events

On the basis of geographic arrangement and similarity in systematic site-to-site residuals, 20 of the 25 stations considered were grouped into six sub-regions. The remaining 5 stations did not exhibit the same trends in their systematic features as did the stations in the same areas. As was the case in Bradley 2015, the goal of creating these sub-regions is to allow for non-ergodic ground motion prediction anywhere within these sub-regions, rather than specifically at the SMS sites.

10 References

Aoi, S., Kunugi, T., & Fujiwara, H. (2008). Trampoline effect in extreme ground motion. Science, *322*(5902), 727-730.

Bradley, B. A. (2010). NZ-specific pseudo-spectral acceleration ground motion prediction equations based on foreign models, Department of Civil and Natural Resources Engineering, University of Canterbury, UC Research Report 2010-03, Christchurch, New Zealand. 324pp. http://ir.canterbury.ac.nz/handle/10092/5126

Bradley, B. A. (2015). Systematic ground motion observations in the Canterbury earthquakes and region-specific non-ergodic empirical ground motion modeling. *Earthquake Spectra*, *31*(3), 1735-1761.

Bradley, B. A., & Cubrinovski, M. (2011). Near-source strong ground motions observed in the 22 February 2011 Christchurch earthquake. *Seismological Research Letters*, *82*(6), 853-865.

Cubrinovski, M., et al. (2011). Geotechnical Aspects of the 22 February 2011 Christchurch Earthquake, *Bulletin of the New Zealand Society for Earthquake Engineering*, *44*, 205-226.

Kim, S. J., Holub, C. J., & Elnashai, A. S. (2010). Analytical assessment of the effect of vertical earthquake motion on RC bridge piers. *Journal of Structural Engineering*, *137*(2), 252-260.

Kunnath, S. K., Erduran, E., Chai, Y. H., & Yashinsky, M. (2008). Effect of near-fault vertical ground motions on seismic response of highway overcrossings. *Journal of Bridge Engineering*, *13*(3), 282-290.

Lee, R. L., Bradley, B. A., & Franklin, M. J. (2013). Characteristics of vertical ground motions in the Canterbury earthquakes. *New Zealand Society for Earthquake Engineering Conference.* 26-28 April 2013. Christchurch, New Zealand. Paper 16. 8pp.

Ghobarah, A., & Elnashai, A. S. (1998, September). Contribution of vertical ground motion to the damage of RC buildings. In *Proceedings of the Eleventh European Conference on Earthquake Engineering* (pp. 9-13).

Ghobarah, A., & Tso, W. K. (1973). Seismic analysis of skewed highway bridges with intermediate supports. *Earthquake Engineering & Structural Dynamics*, *2*(3), 235-248.

Papazoglou, A. J., & Elnashai, A. S. (1996). Analytical and field evidence of the damaging effect of vertical earthquake ground motion. *Earthquake engineering and structural dynamics*, *25*(10), 1109-1138.

Rodriguez-Marek, A., Montalva, G. A., Cotton, F., & Bonilla, F. (2011). Analysis of single-station standard deviation using the KiK-net data. *Bulletin of the Seismological Society of America*, *101*(3), 1242-1258.

Saadeghvariri, M. A., & Foutch, D. A. (1991). Dynamic behaviour of R/C highway bridges under the combined effect of vertical and horizontal earthquake motions. *Earthquake Engineering & Structural Dynamics*, *20*(6), 535-549.

Silva, W. (1997). Characteristics of vertical strong ground motions for applications to engineering design. *National Center for Earthquake Engineering.* Technical Report 1997-0010, 205-252.

Yang, J., & Sato, T. (2000). Interpretation of seismic vertical amplification observed at an array site. *Bulletin of the Seismological Society of America*, *90*(2), 275-285.

Appendix A: NGA-West2 Predictions versus Observations for Additional Periods

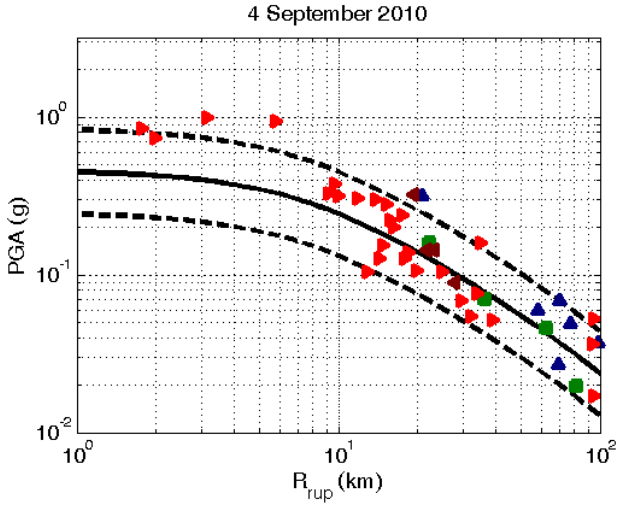

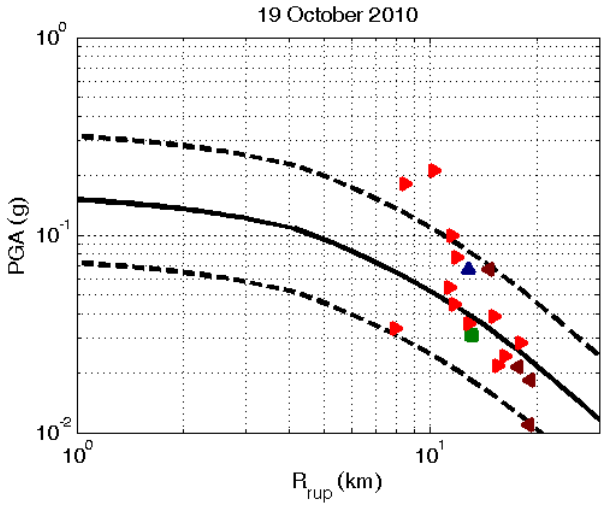

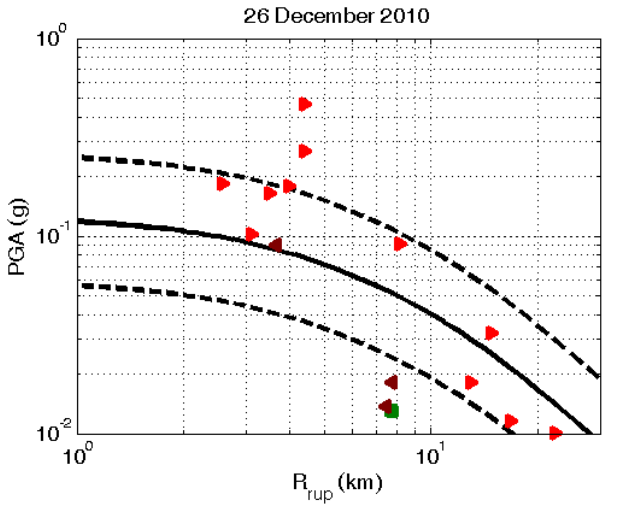

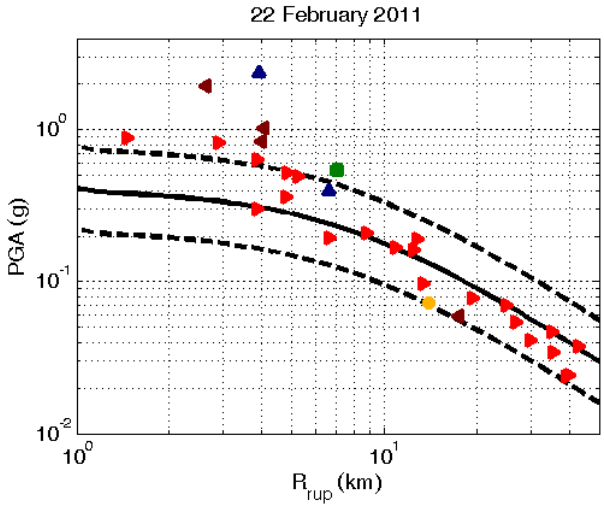

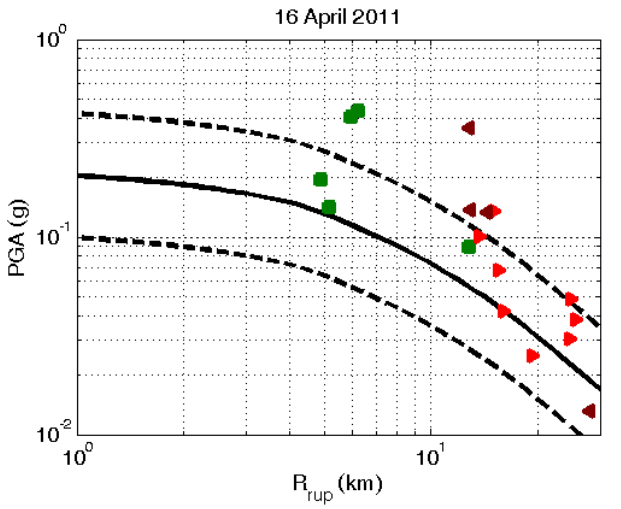

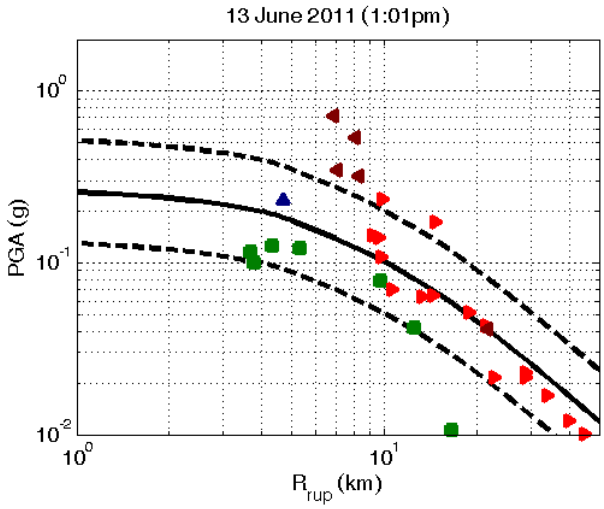

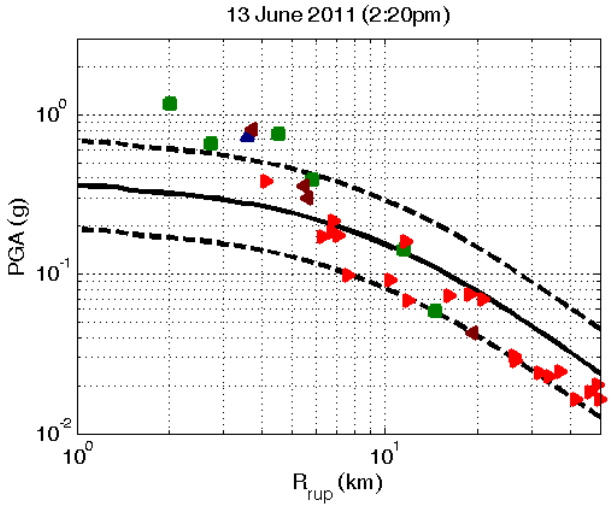
13 June 2011 (2:20pm)
PGA (g)
10^{0}
10^{-1}
10^{-2}
10^{0}
10^{1}
R_{rup} (km)

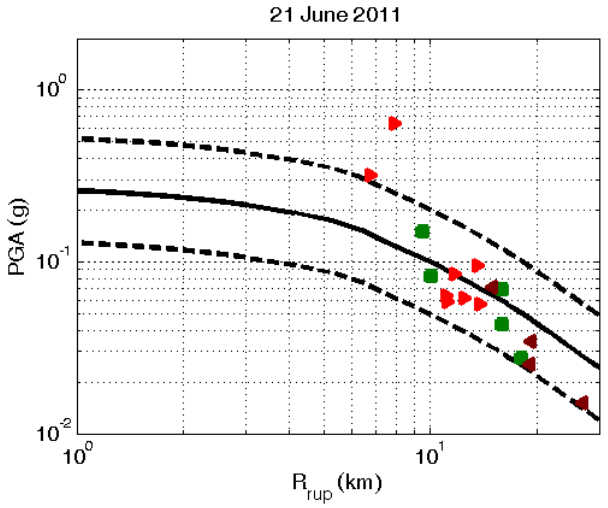
21 June 2011
PGA (g)
10^{0}
10^{-1}
10^{-2}
10^{0}
10^{1}
R_{rup} (km)

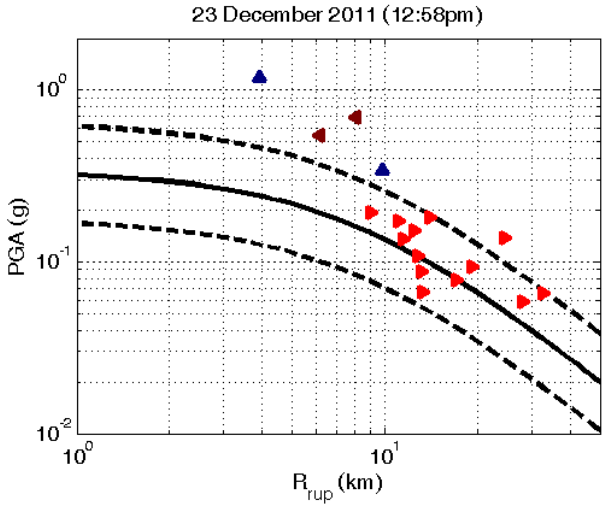
23 December 2011 (12:58pm)
PGA (g)
10^{0}
10^{-1}
10^{-2}
10^{0}
10^{1}
R_{rup} (km)

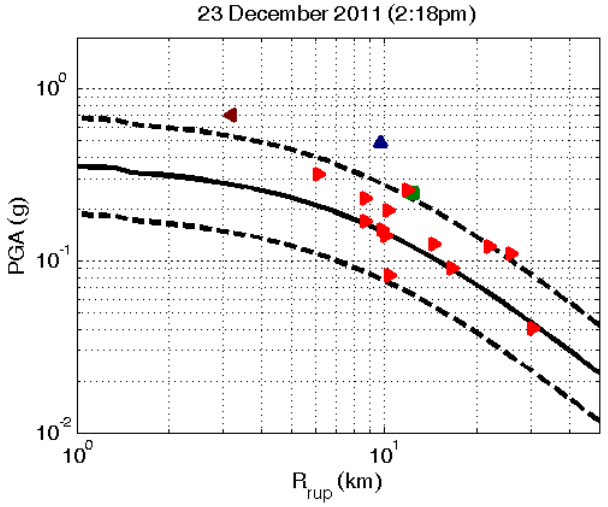
23 December 2011 (2:18pm)
PGA (g)
10^{0}
10^{-1}
10^{-2}
10^{0}
10^{1}
R_{rup} (km)

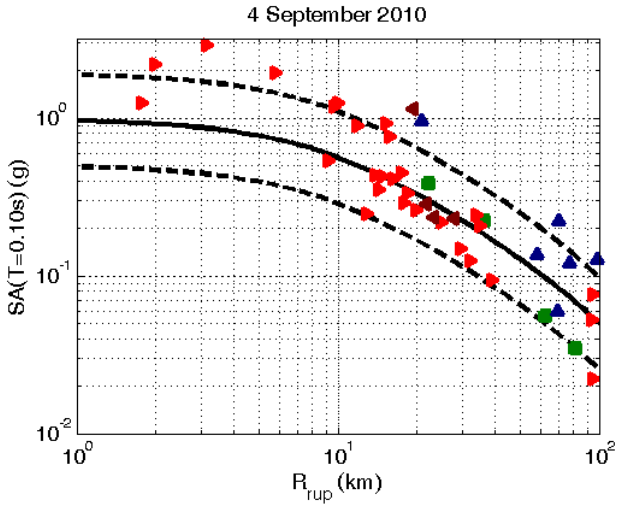
4 September 2010
SA(T=0.10s) (g)
R_rup (km)

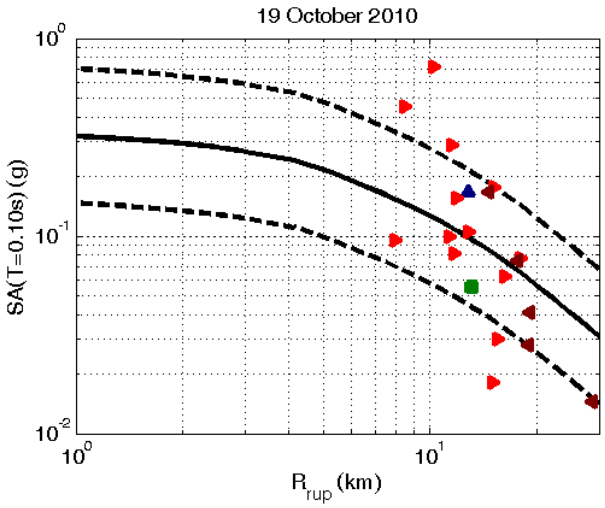
19 October 2010
SA(T=0.10s) (g)
R_rup (km)

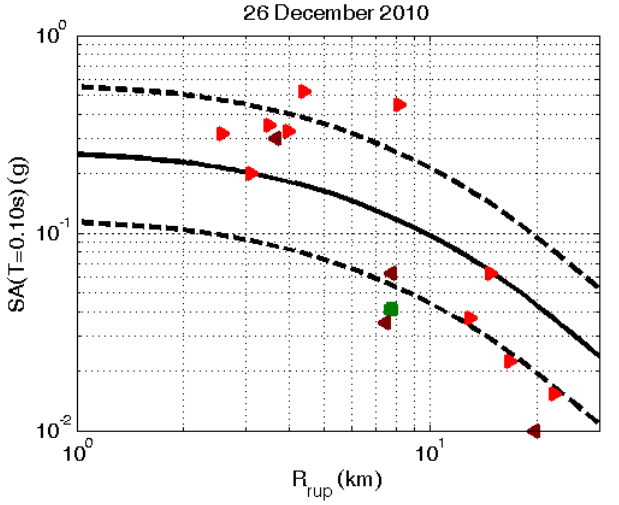
26 December 2010
SA(T=0.10s) (g)
R_rup (km)

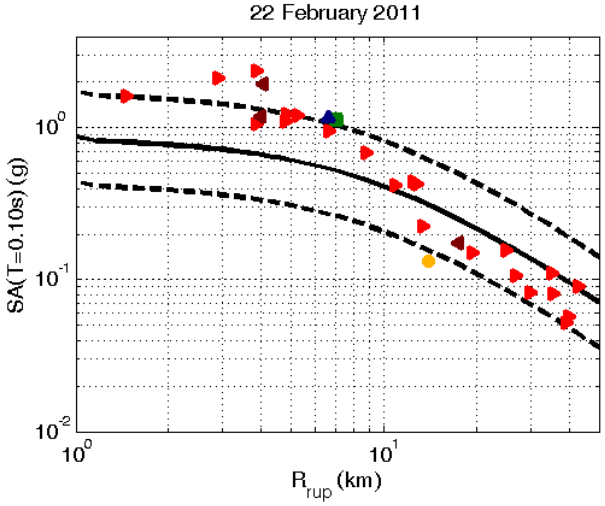
22 February 2011
SA(T=0.10s) (g)
R_rup (km)

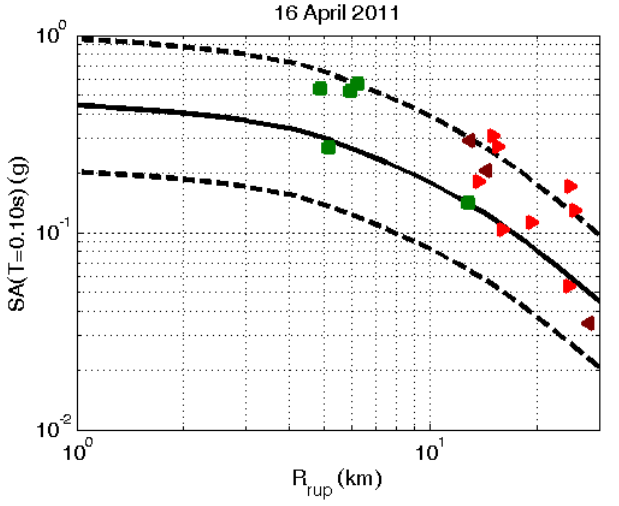
16 April 2011
SA(T=0.10s) (g)
R_rup (km)

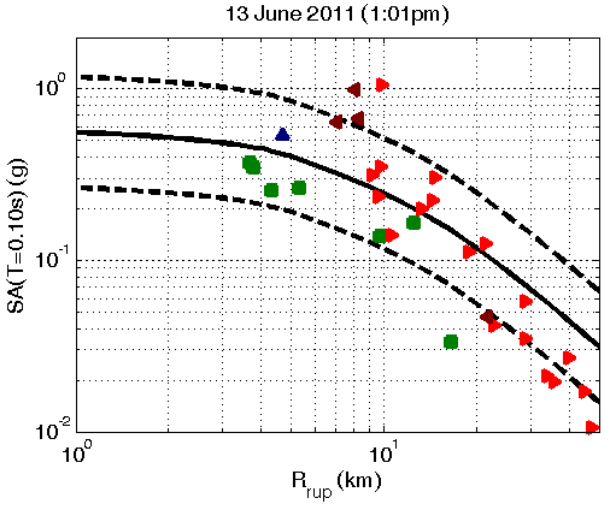
13 June 2011 (1:01pm)
SA(T=0.10s) (g)
R_rup (km)

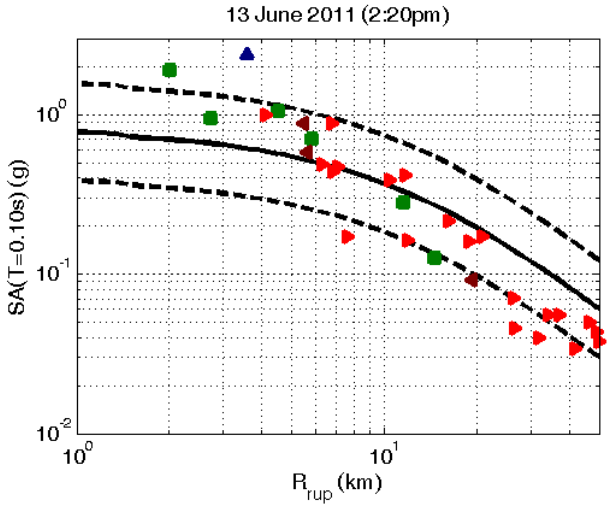
13 June 2011 (2:20pm)
SA(T=0.10s) (g)
10^{0}
10^{-1}
10^{-2}
10^{0}
10^{1}
R_{rup} (km)

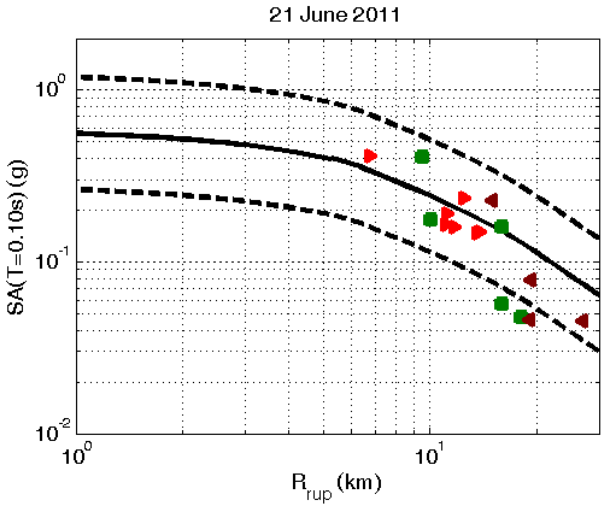
21 June 2011
SA(T=0.10s) (g)
10^{0}
10^{-1}
10^{-2}
10^{0}
10^{1}
R_{rup} (km)

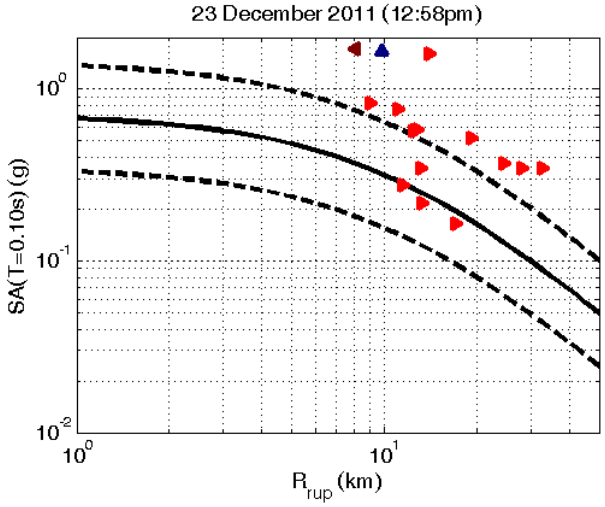
23 December 2011 (12:58pm)
SA(T=0.10s) (g)
10^{0}
10^{-1}
10^{-2}
10^{0}
10^{1}
R_{rup} (km)

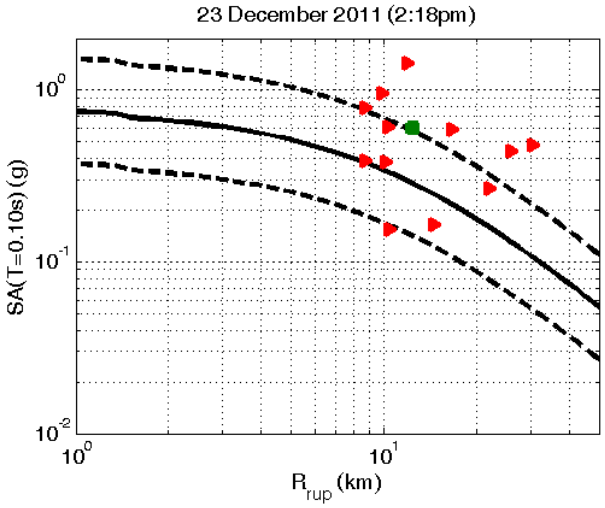
23 December 2011 (2:18pm)
SA(T=0.10s) (g)
10^{0}
10^{-1}
10^{-2}
10^{0}
10^{1}
R_{rup} (km)

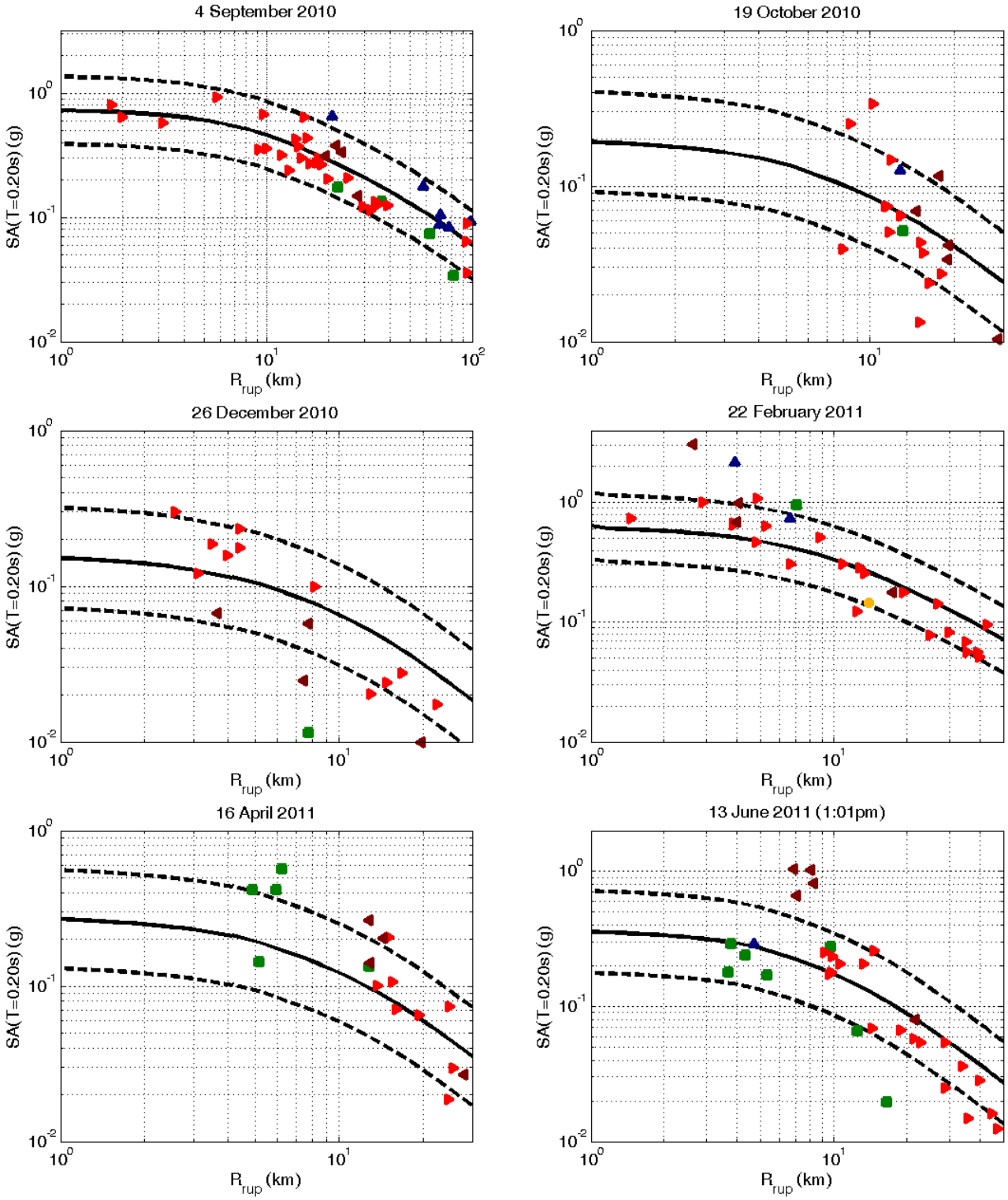
4 September 2010
19 October 2010
26 December 2010
22 February 2011
16 April 2011
13 June 2011 (1:01pm)
SA(T=0.20s) (g)
R_rup (km)

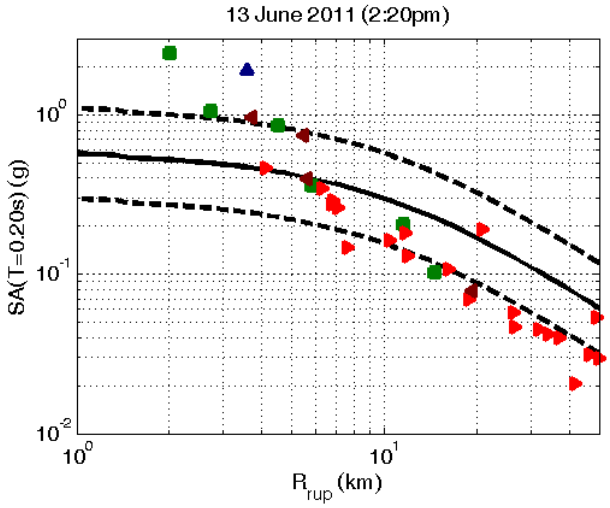
13 June 2011 (2:20pm)
SA(T=0.20s) (g)
10^{0}
10^{-1}
10^{-2}
10^{0}
10^{1}
R_{rup} (km)

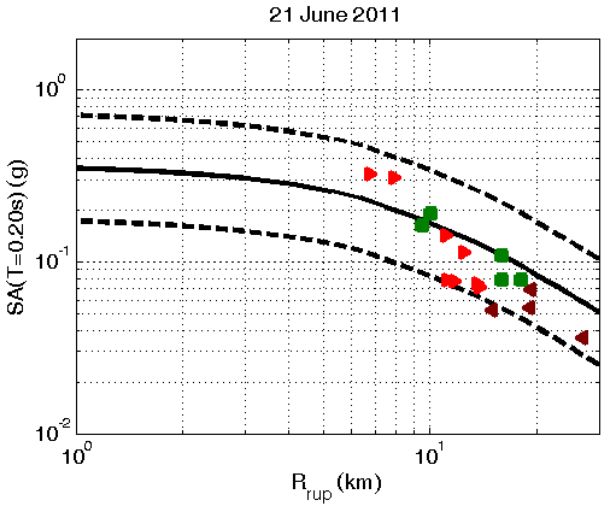
21 June 2011
SA(T=0.20s) (g)
10^{0}
10^{-1}
10^{-2}
10^{0}
10^{1}
R_{rup} (km)

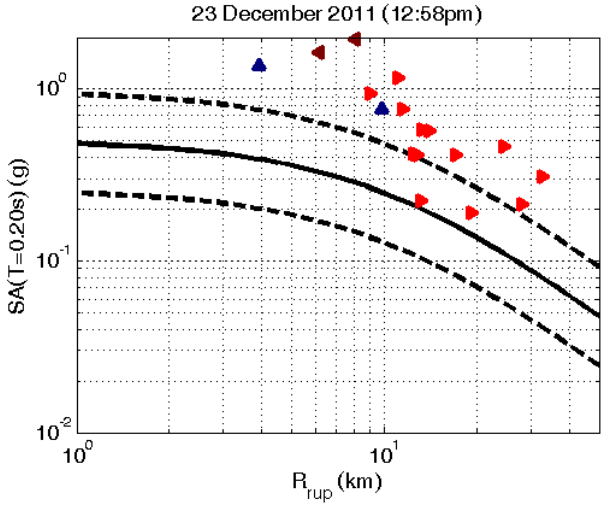
23 December 2011 (12:58pm)
SA(T=0.20s) (g)
10^{0}
10^{-1}
10^{-2}
10^{0}
10^{1}
R_{rup} (km)

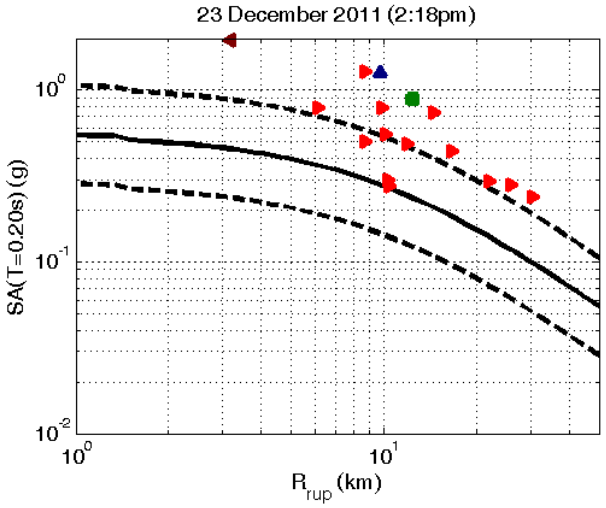
23 December 2011 (2:18pm)
SA(T=0.20s) (g)
10^{0}
10^{-1}
10^{-2}
10^{0}
10^{1}
R_{rup} (km)

Appendix B: Within-Event Residuals for All Stations

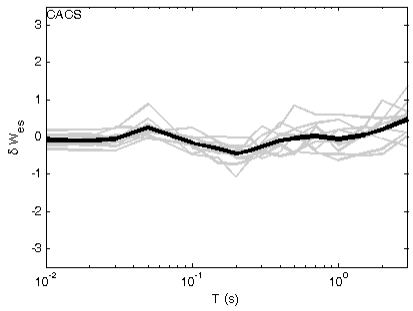

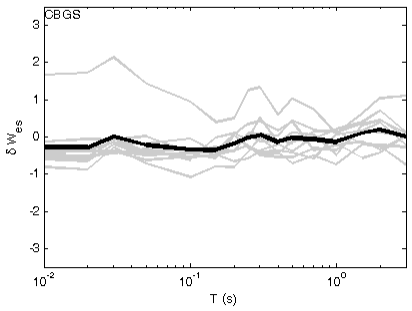

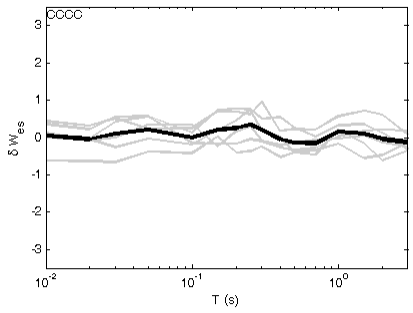

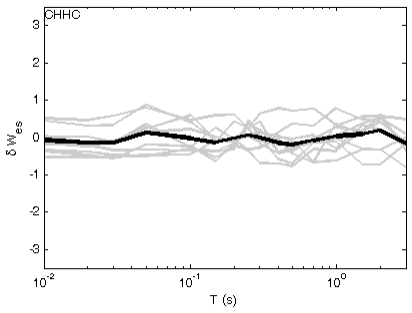

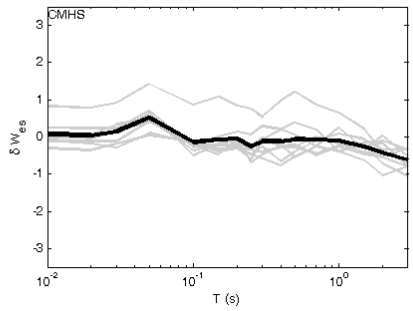

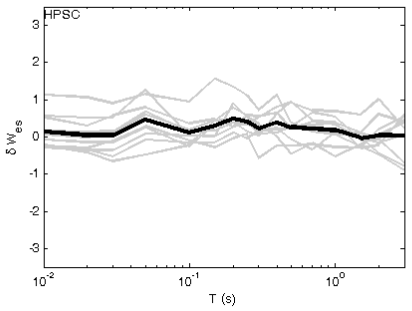

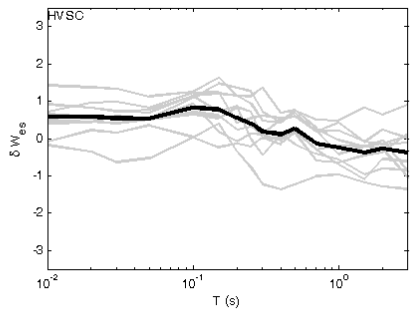

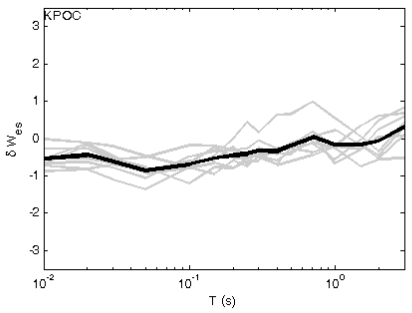

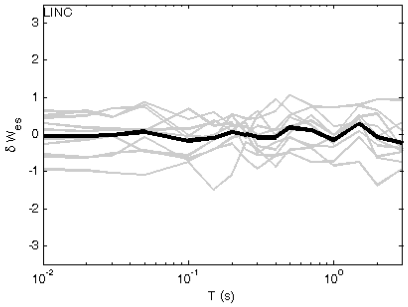
LINC
δ Wes
T (s)

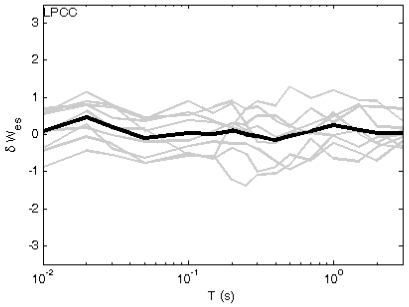
LPCC
δ Wes
T (s)

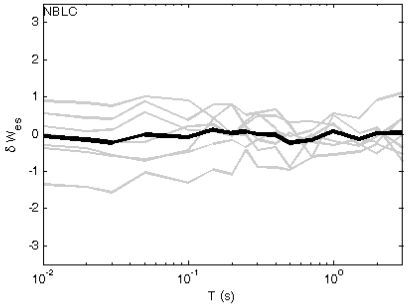
NBLC
δ Wes
T (s)

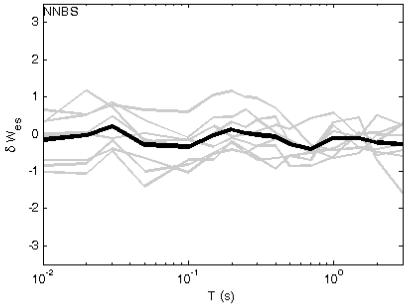
NNBS
δ Wes
T (s)

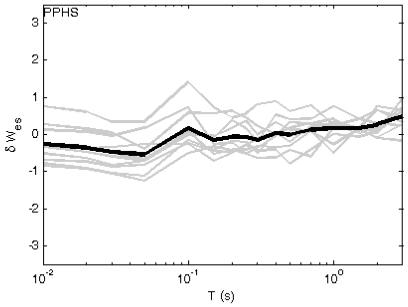
PPHS
δ Wes
T (s)

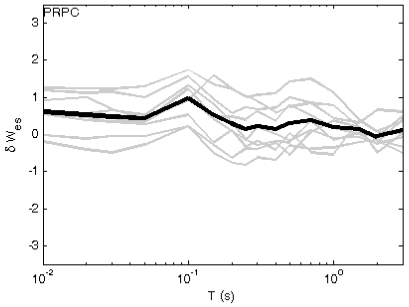
PRPC
δ Wes
T (s)

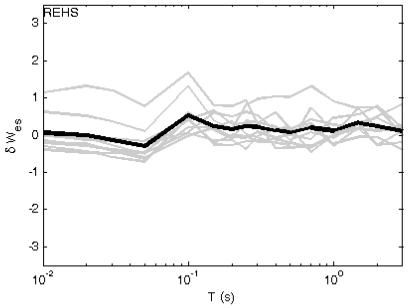
REHS
δ Wes
T (s)

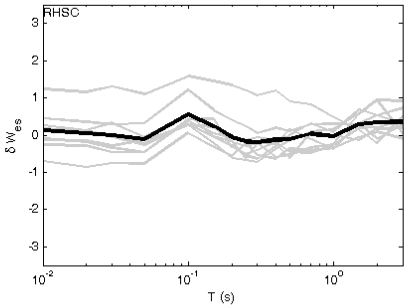
RHSC
δ Wes
T (s)

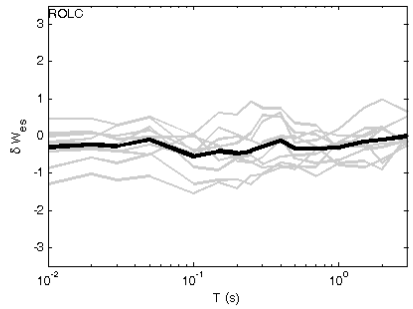
ROLC
δ W_es
T (s)

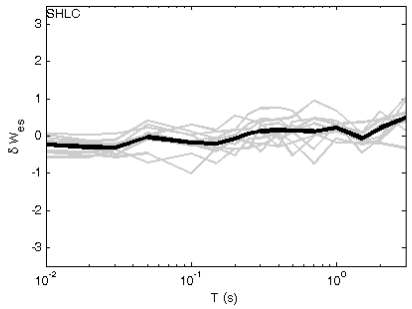
SHLC
δ W_es
T (s)

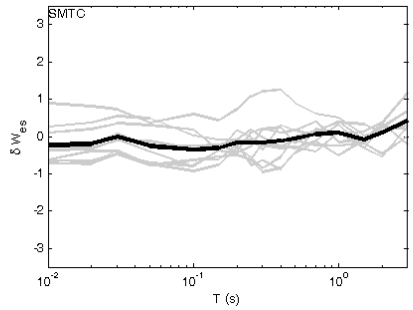
SMTC
δ W_es
T (s)

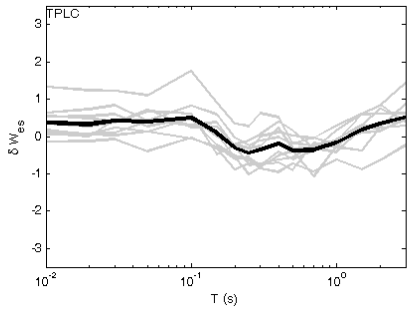
TPLC
δ W_es
T (s)

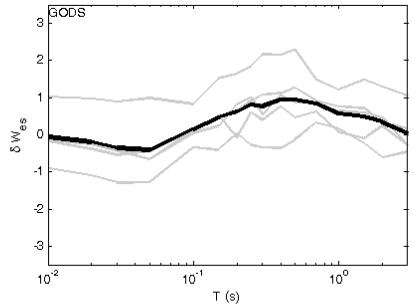
GODS
δ W_es
T (s)

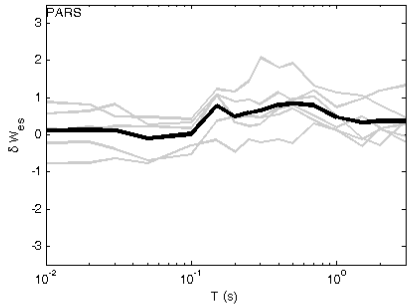
PARS
δ W_es
T (s)

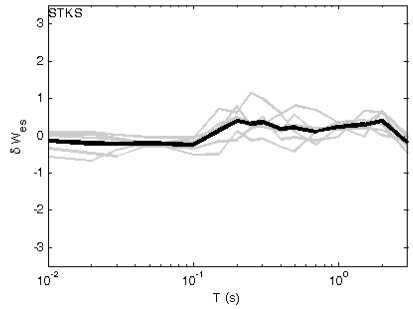
STKS
δ W_es
T (s)

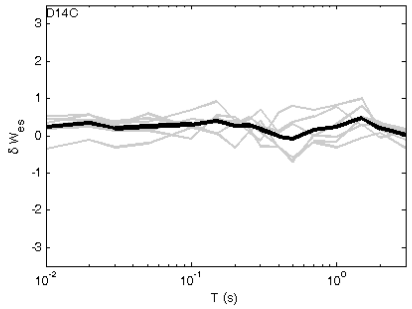
D14C
δ W_es
T (s)

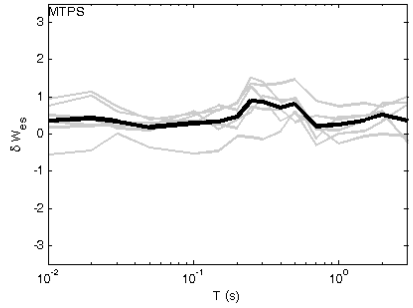
MTPS
δ W_es
T (s)

Appendix C: Within-Event Standard Deviations

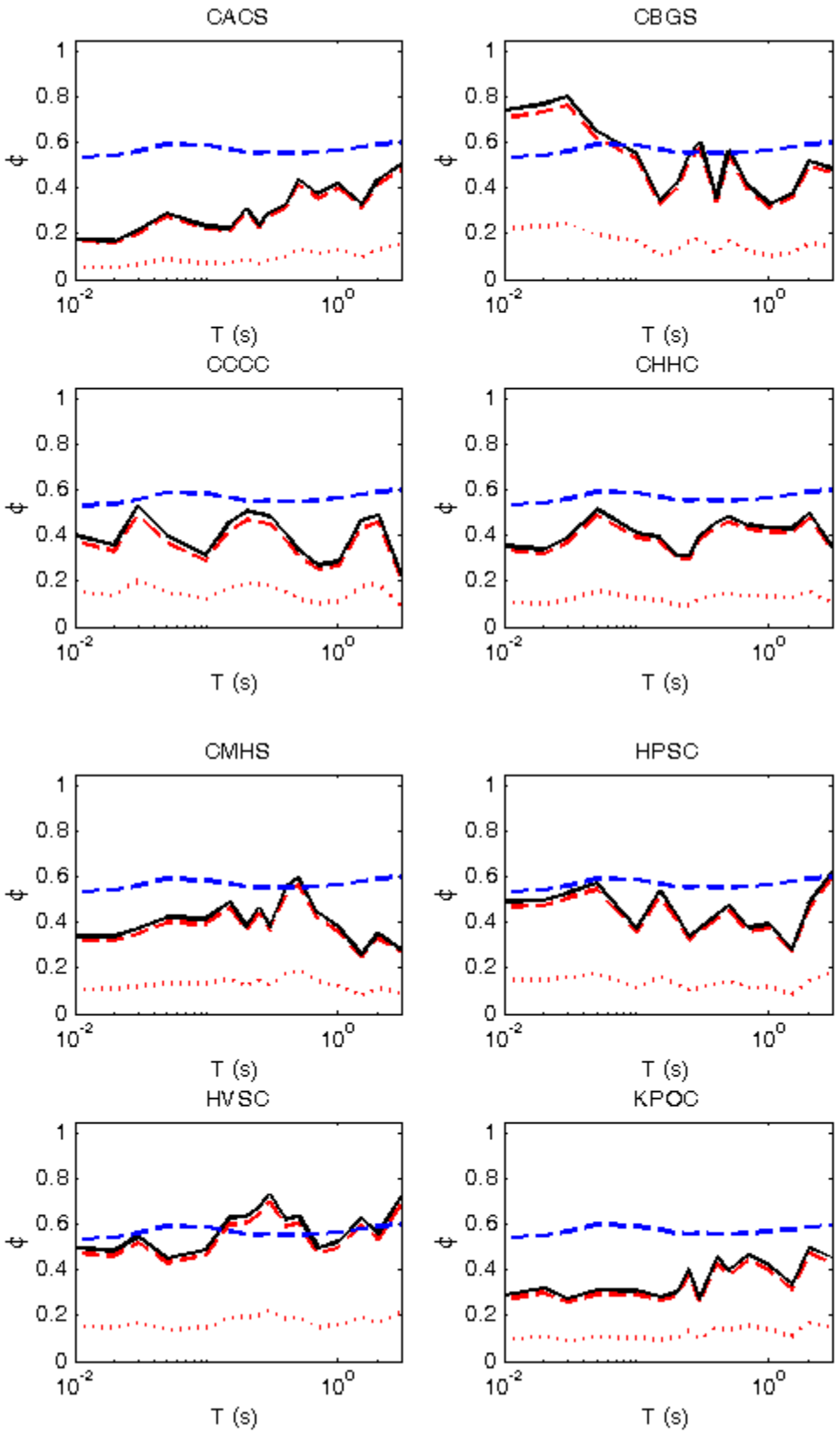

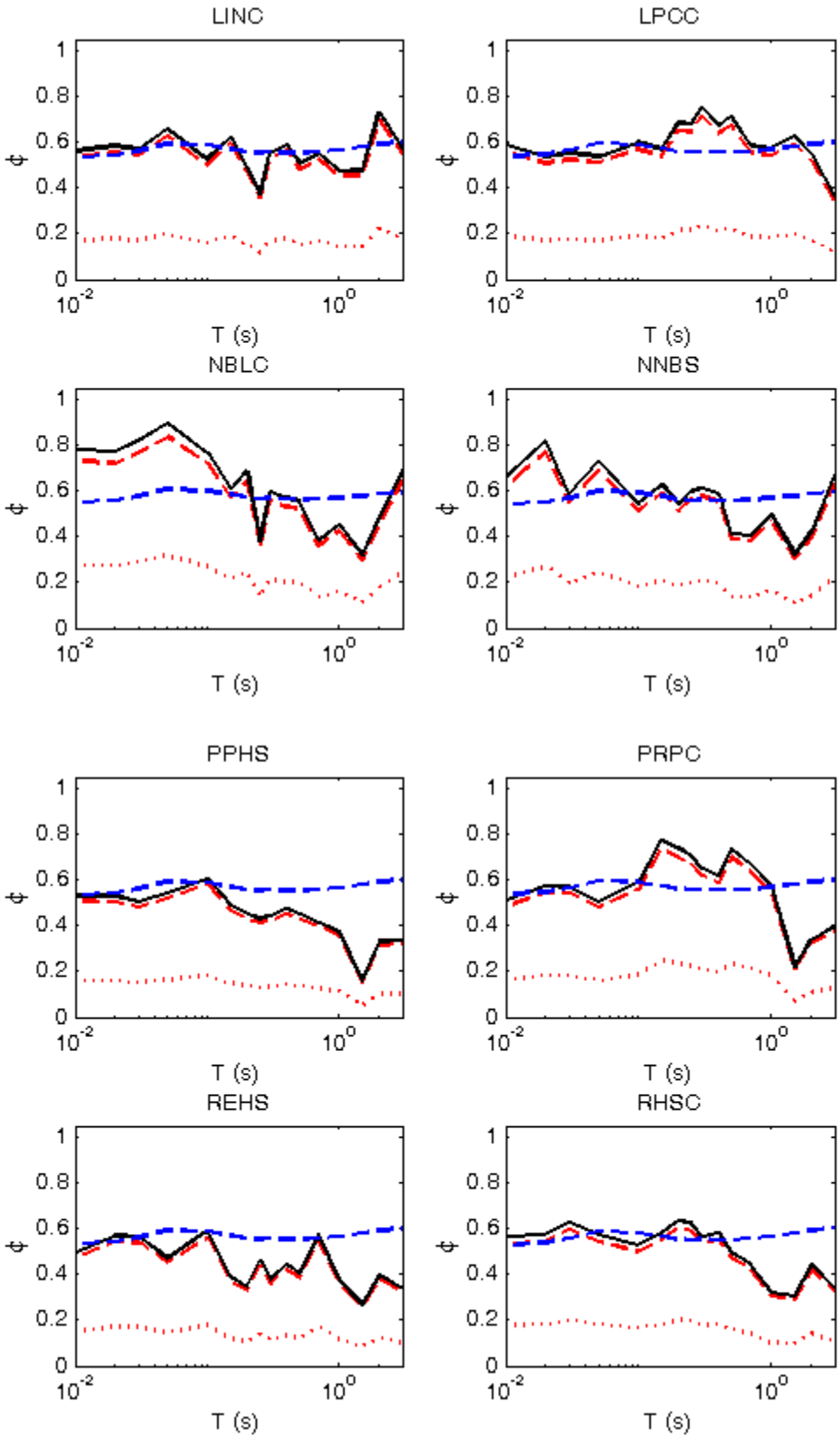
LINC
LPCC
NBLC
NNBS
PPHS
PRPC
REHS
RHSC
ϕ
T (s)
0
0.2
0.4
0.6
0.8
1
10^-2
10^0

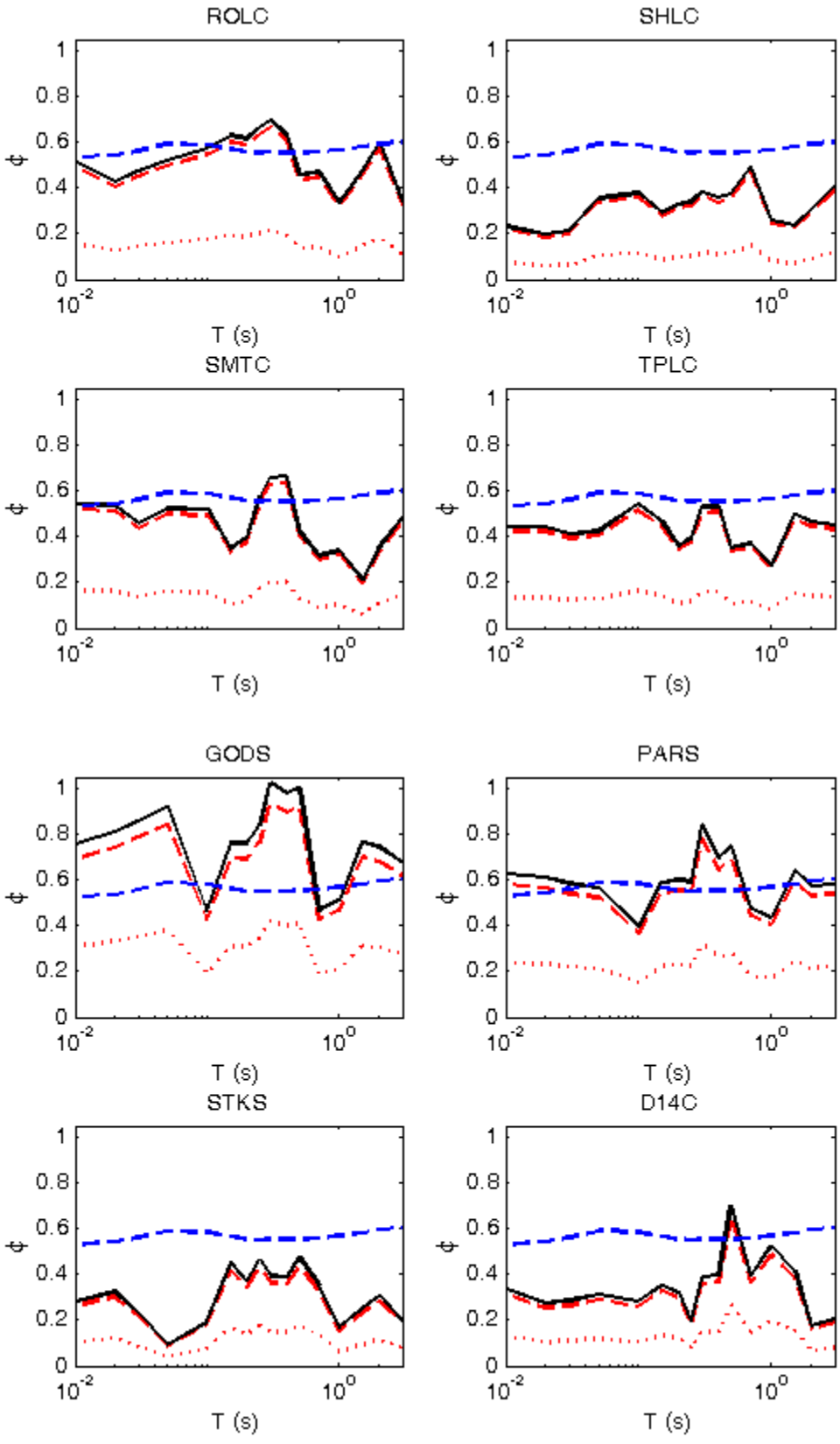
ROLC
SHLC
SMTC
TPLC
GODS
PARS
STKS
D14C
ϕ
T (s)
0
0.2
0.4
0.6
0.8
1
10^-2
10^0

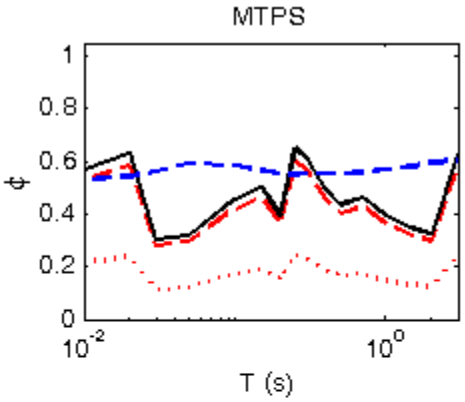
MTPS
1
0.8
0.6
0.4
0.2
0
ϕ
10^-2
10^0
T (s)